Università degli Studi di Perugia

Dipartimento di Fisica e Geologia

Corso di Laurea in Fisica delle Particelle Elementari

Tesi di Laurea Magistrale

Charmed mesons as a probe for Triple Parton Scattering

Supervisors:
Prof. Livio Fanò
Dott.ssa Valentina Mariani

Student:
Maria Elena Ascioti

Academic Year 2021 - 2022

Abstract

The recent observation of three J/ψ production by the Compact Muon Solenoid (CMS) Collaboration raised large interest in Multiple Parton Scattering. While the study of multiple *hard* parton scattering at large x is limited by cross section,extending the investigation to lower mass final states is experimentally challenging because of the huge background expected at LHC. Only recently, for the first time the simultaneous production of three J/ψ mesons have been interpreted as originating from Triple Parton Scattering (TPS) processes, even with a precision on the measured cross section limited by statistics. In this thesis, I investigated a novel mesonic final state which can increase the sensitivity to TPS. On the one hand, the CMS experiment excels in muons reconstruction, J/ψ in their muonic decay can be clearly reconstructed and are then optimal trigger for the process, on the other hand the cross section for an open charm meson is larger than the one for a $c\bar{c}$ state. A final state with two J/ψ and a D^* is expected to provide a more suitable way to directly access TPS production at LHC, with a strong control of experimental systematics. In this work, the J/ψ are reconstructed by their decay into muons pair, meanwhile, the D^* mesons are reconstructed by its most probable decay chain: $D^{*+} \rightarrow D^0\pi^+_{slow} \rightarrow K^-\pi^+\pi^+_{slow}$. After setup the Monte Carlo generation of signal and background samples, a study has been done deeply analyzing event kinematic and topology providing an indication on possible discriminating observables.

Dimidium facti, qui coepit, habet; *sapere aude*, incipe.
Orazio, Epist., I, 2, 40.

Alla mia famiglia, a chi c'è, a chi avrebbe desiderato esserci.

Contents

Chapter 1

Introduction

Multi Parton Interactions (MPI) are studied with an eye to the past and one to the future, aiming a better classification of the processes in hadron interactions and to improve the understanding of the hadron structure. In the overall pictures of MPI studies, this thesis represents a proposal of a novel study for both open charmed mesons and charmed quarkonia as a probe for *Triple Parton Scattering* (TPS).

In November 2021, the Compact Muon Solenoid (CMS) collaboration published the analysis [1] of a final state with a triple J/ψ and only five events that can be interpreted as a production via Triple Parton Scattering (20%), via Double Parton Scattering (74%) and Single Parton Scattering (6%), have been found. To enhance the probability of finding events of interest, a final state with a larger cross section is needed, and since the open charmed mesons have a larger cross section as opposed to the charmed quarkonia, one of the J/ψ has been here replaced with a D^* meson. I have investigated the final state with two J/ψ and a D^* in the CMS experimental framework with the idea, in a future time, of a complete analysis of the Run II and Run III data. The whole point of this thesis is to present at the Monte Carlo level, without any simulation of the detector, the possibility for the Compact Muon Solenoid [2] experiment to study the proposed process This peculiar final state has been chosen because, on the one hand, the CMS experiment excels in muons reconstruction (the J/ψ are principally reconstructed from their decay into muon pairs of opposite signs), on the other hand, the cross section for an open charm meson is larger than the one for a $c\bar{c}$ state. Since, among all the open charm mesons, the CMS experiment can reconstruct with a higher purity the D^* (i.e. a meson which has one c quark and one quark of different flavour) a final state with two J/ψ and a D^* may be more for a direct measurement of TPS. Sample generation is the mandatory first step for an Monte Carlo study: I have used HELAC-Onia [3][4] and PYTHIA [5] to generate samples for TPS events and

DPS + SPS, which is the only inclusive background considered in this study. Both HELAC-Onia and PYTHIA are open-source software that can be employed for the generation of a plethora of physics processes at fundamental level: the joint use of both the programs was necessary, but not sufficient, to produce the complete desired final state. A deep study and insight of the Les Houches Events File format were necessary indeed to reproduce the so-called pocket formula, which is the factorized representation for the cross section of n parton scattering. The pocket formula is the result of the assumption of parton independence and non-correlation that are made to simplify the general cross section, whose calculation will be far away from being trivial. The obtained samples are analysed using, in a first step, the Monte Carlo *truth*, namely knowing the full event history in detail, and in a second one simulating a reconstruction strategy: an esteem of the algorithmic efficiency is finally provided.
The thesis has the following structure: the second and the third chapters describe the Large Hadron Collider and the Compact Muon Solenoid apparatus, respectively. These two chapters aim to illustrate the framework and the context where this analysis is collocated, giving the reader an initial knowledge to understand the larger picture behind this thesis. The fourth chapter describes the theoretical framework of the n parton interactions: starting from the parton distribution functions and moving to the n parton scattering, the reader can finally understand which is the state of the art of the Double and Triple Parton Scattering. Here all the theoretical motivations are provided. The fifth chapter gets to the heart of this thesis: here all the motivations for the choice of the investigated final state are presented. In addition, the whole procedure followed for the sample generation is explained in detail. The next chapter presents and explains the analysis procedure and the results obtained. Finally, in the last chapter, the conclusions and the suggestions for future developments of this study are illustrated.

Chapter 2

The Large Hadron Collider

2.1 Introduction

Located at CERN in Geneva, between Switzerland and France, the Large Hadron Collider (LHC) [6] is the largest and most energetic collider ever built. Its design and realization are the results of the increasing interest and ideas in particle physics in the 1970s. New experimental technologies, nevertheless, had to be developed to achieve the energies needed to demonstrate the existence and the prediction of some theoretical thesis. The LHC project received a boost thanks to the brilliant physics results achieved at the time. Where today is located the LHC, once there was the LEP collider (figure 2.1) which was an electron-positron collider that successfully measured the mass of both the W and Z bosons in 1982 and 1983 [7] [8] [9][10]. Another relevant asset at CERN was the existence of a well-proven chain of injectors (linac, booster, PS and SPS), which, after some modifications, could be used for injecting protons and ions into rings in the LEP tunnel. The feasibility study for a proton-proton collider in the LEP tunnel started at the end of 1982. The project was approved by the CERN Council in December 1994 and, according to plans, the commissioning should have started in 2007.

The main initial steps of the LHC can be summarized in three phases:

- The period from 1982 to 1987 was dedicated to the basic technical choices and the exploration of the parameter space.
- The period from 1987 to 1993/1994 was characterized by magnet models, more intense technical work and final project definition.
- The period from 1994 to 2004 was marked by the final design of all systems, the arrival on site of hundreds of magnets and substantial progress on all other systems [10].

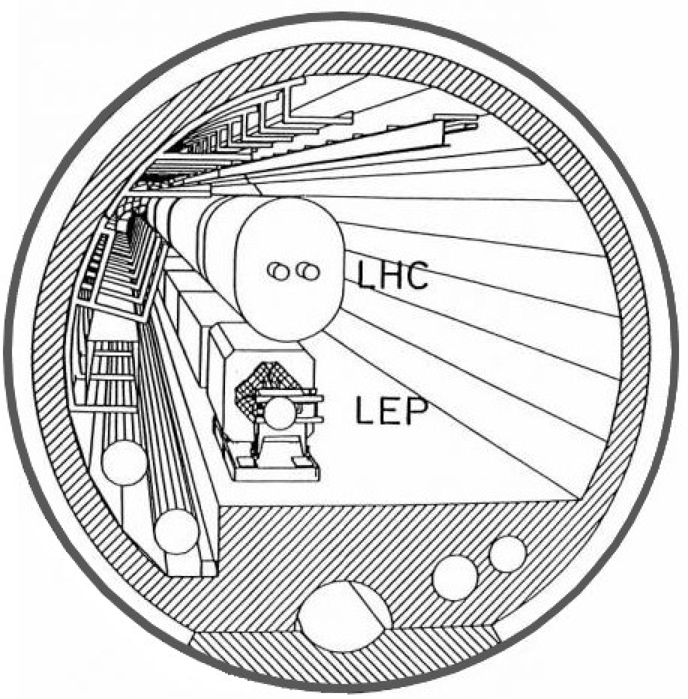

Figure 2.1: First pages of the Proceedings of the LHC workshops held in Lausanne, 1984 [ECFA-CERN 1984], and Aachen, 1990 [Jarlskog and Rein 1990]. Note the early design of the machine layout in the LEP tunnel, with the LHC and the LEP rings together. Coexistence of the two machines was considered up to 1995, when it was dismissed by Chris Llewellyn Smith at the Lepton-Photon Conference in Beijing [11].

Only in June 2008, the LHC was declared operational and no longer a project; later the same year the first attempt to circulate the beam in the LHC took place. Despite the first attempt seeming successful, after only nine days of preliminary beam commissioning, on 19 September 2008, disaster struck: the last octant was being ramped up in preparation for high energy operation when a magnet interconnects failed and the enormous energy stored in the superconducting magnets was released in an uncontrolled way and damaged around 600 m of the LHC installed equipment [12]. The next 14 months were crucial for the machine: all the forces were focused on repairing the damaged sector and on understanding the causes of the accident. After overcoming the difficulties, the LHC finally became operating.

In the following table all the main characteristics of the past and future phases are summarized.

Parameter	Design	Run I	Run II	Run III	HL-LHC
Energy [TeV]	14	7/8	13	13.6	14
Bunch spacing [ns]	25	50	25	25	25
Bunch Intensity [10^{11} ppb]	1.15	1.6	1.2	up to 1.8	2.2
Number of bunches	2800	1400	2500	2800	2800
Emittance [μm]	3.5	2.2	2.2	2.5	2.5
β^*[cm]	55	80	$30 \rightarrow 25$	$30 \rightarrow 25$	down to 15
Crossing angle [μrad]	285	–	$300 \rightarrow 260$	$300 \rightarrow 260$	TBD
Peak Luminosity [10^{34}cm^{-2}s^{-1}]	1.0	0.8	2.0	2.0	5.0
Peak pileup	25	45	60	55	150

Table 2.1: Summary of main accelerator parameters for the LHC, showing the design values, and those used during Run I and Run II, as well as the expected parameters for Run III and the HL-LHC [13].

2.2 The LHC structure

The LHC collider has been installed more than 100 meters below ground in a tunnel of 27.6 km circumference on the Franco-Swiss border near Geneva, Switzerland [14]. The tunnel was initially built for and previously used by the large e^+e^- collider LEP, thus the basic layout of the LHC mirrors that of LEP, with eight long straight sections each approximately 500 metres in length available for experimental insertions or utilities. In figure 2.2 is possible to see that the two high luminosity proton-proton experiments are located at diametrically opposite straight sections, Point 1 (ATLAS [15]) and Point 5 (CMS [16]). Two more experimental insertions are foreseen at Point 2 (ALICE [17], mainly focused on Pb-ions) and Point 8 (LHCb [18], mainly focused on B-physics). These insertions also contain the two injection systems. The beams cross from one ring to another at these four locations [19].

2.2.1 The intial project

Since high energy was required to allow the production of new heavy particles, like the Higgs particle predicted by the Standard Model (SM), breaking the energy and luminosity frontiers was crucial, thus, these are two of the most important design parameter for an accelerator for particle physics. It was also relevant to achieve a high flux of particles resulting in a sufficiently high number of collisions. The collision rate n for a process of cross section σ is the product of the luminosity L

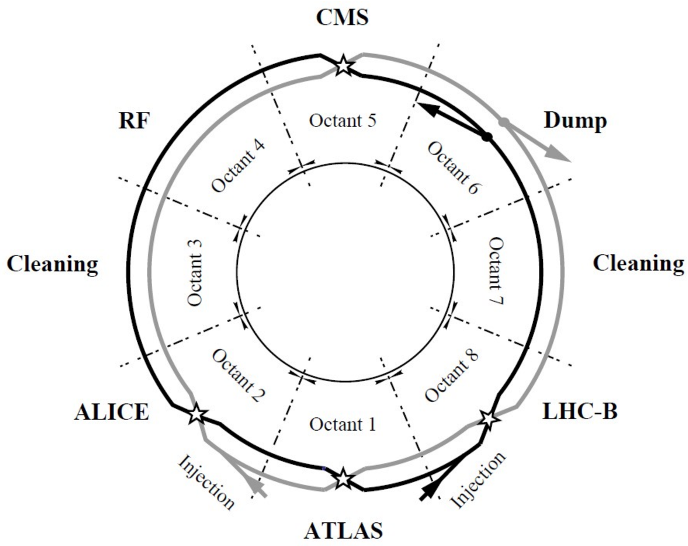

Figure 2.2: Global layout of LHC [19].

and the cross section:

$$n = \sigma \cdot L, \tag{2.1}$$

where cross sections are usually given in units of barn (symbol b) which is defined as $1\text{b} = 10^{-28}\text{m}^2$. The luminosity of a collider is determined by the icoming proton flux and geometry. For head-on collisions, the luminosity is:

$$L = \frac{N_1 N_2 n_b f_{rev}}{A} \tag{2.2}$$

where N_1, N_2 are the number of particles per bunch in beam 1 and 2 respectively, n_b is the number of bunches, f_{rev} the revolution frequency and A is the effective area of beam overlap [14]. The main path to very high luminosities in the LHC is to use many bunches, nearly 3000, and to reduce the transverse beam size at the Interaction Points (IPs) by manipulations of the magnetic focusing system at top energy, the so-called squeezing of the beams before the beams are brought into collisions [14].

Assuming a gaussian beam, the r.m.s. beam size at the position s in the machine is $\sigma(s) = \sqrt{\epsilon\beta(s)}$, where ϵ is an average beam quantity called emittance and beta is a quantity related to the transverse size of the particle beam. The emittance represents the beam size in transverse phase space. For simplicity, the dispersion is neglected since it is usually small in the interaction regions. To focus the beams near the interaction regions, strong quadrupole magnets are implied: the aim is to obtain small values of the β-function at the interaction point (called $\beta*$) resulting in small beam sizes and high luminosity (figure 2.3).

Alongside the quadrupoles, one finds the dipole magnets whose purpose is to orient the beams along the beam pipe. The superconducting $NbTi$ magnets need an operating temperature of 1.9 K: this temperature allows fields up to $B = 8.33$ T and $p = 7$ TeV/c [14].

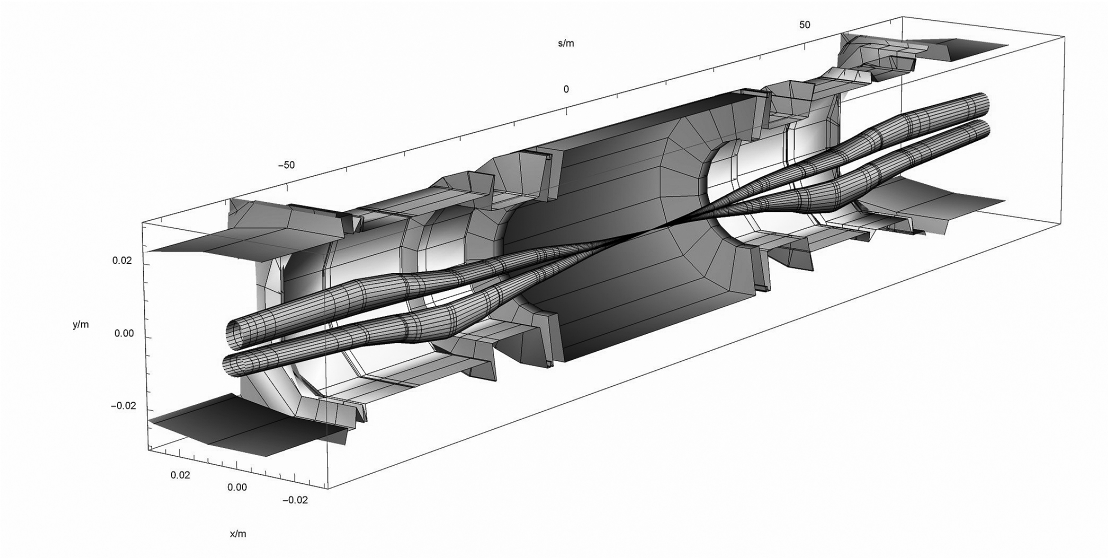

Figure 2.3: Schematic of how the transverse dimensions of the bunches change nearby the collision point.

The protons running in the collider are extracted from hydrogen gas: electrons are torn off through an electric field, meanwhile, the remaining protons can enter the acceleration system. This procedure last until the protons reach the minimum level prescripted. The first accelerator in the chain is Linac 2 which accelerates the protons up to 50 MeV. Then the beam is injected into the Proton Synchrotron Booster (PSB) followed by the Proton Synchrotron (PS), scaling up from 1.4 GeV to 25 GeV. The last step before entering the LHC is the Super Proton Synchrotron (SPS) where the beam is accelerated up to 450 GeV. Finally, after 4 minutes and 20 seconds, each LHC ring is filled: in one ring the proton beam circulates clockwise and anticlockwise in the other one. It takes about 20 minutes for the protons to reach their actual maximum energy of 6.5 TeV, the Run II energy [20]. A schematic of the acceleration complex is shown in figure 2.4.

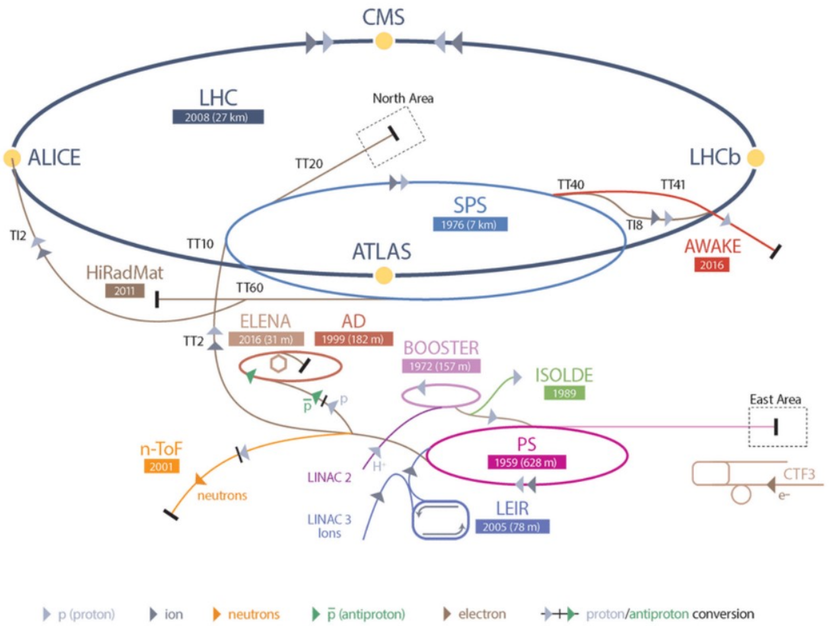

Figure 2.4: Schematic of CERN's LHC starring accelerator complex.

The acceleration of the beams is ensured by the radio frequency cavities (RF) where an electric field is produced, and the electromagnetic waves resonate with the structure and accumulate within it. The energy is thereby passed to the charged particles passing through the cavity. Hence the RF systems provide a longitudinal focus which constraints the particle motion in the longitudinal phase space to a confined region called the RF bucket. The RF frequency of the LHC is 400 MHz which corresponds to 75 cm wavelength or buckets of 2.5 ns length [14] [20].

The focus of the beams is left to a system of dipole and quadrupole magnets. The dipoles curve the beam track along the circumference meanwhile the role of quadrupoles can be compared to one of the lenses in optic: they can focus the beam in one of the transverse coordinates. Thus the first quadrupole squeezes the width of the bunch, meanwhile, the second magnet focuses the beam height. Summing up both the effects the protons result in a *compressed* bunch which allows a greater number of collisions (figure 2.5). The magnet system is thereby crucial to rise the luminosity up to the value goal. There is a total of 858 quadrupoles magnets along the LHC circumference [21].

The basic structure of both dipoles and quadrupoles is the two-in-one design, where the two beam channels are incorporated into a single iron yoke and cryostat, operating in pressurised superfluid helium. Because of the large bursting force of more than 500 tonnes per metre, the coils must be firmly clamped in a rigid

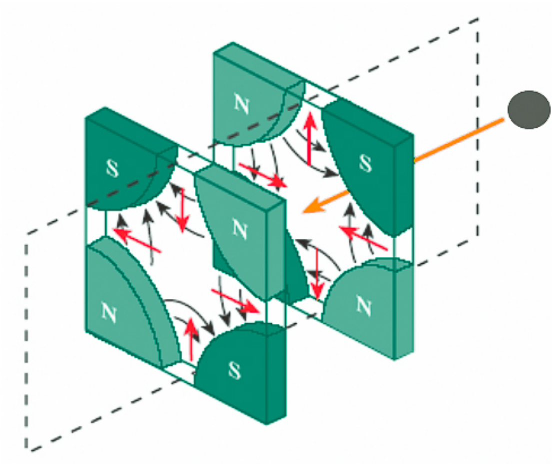

Figure 2.5: LHC quadrupoles focusing system: the positive particles coming from the right are focused in height by the first quadrupole magnet and in width by the second one.

mechanical structure [19].

Although protons have a mass sufficiently large to neglect the energy lost by synchrotron radiation when considering the collision energy, the same radiation must not be neglected when considering the cooling system. Indeed, due to the synchrotron radiation emitted by the protons (almost 4 kW per ring at 7 TeV) and the heating due to the image currents in the wall of the vacuum chamber, the magnet cold bore at 1.9 K must be shielded from the beam, otherwise, the required cryogenic power would become excessive. An inner liner cooled to around 20 K through tubes carrying high-pressure gas has been installed inside the cold bore [19].

Another important parameter that characterized a collider is the pile-up (PU): by definition, the pile-up is the medium value of proton-proton interactions in the same bunch crossing in addition to the one of interest. Such effect gains relevance in high luminosity conditions. The ATLAS and CMS experiments received on average almost 20 collisions during each bunch crossing during Run I. This number increased to over 40 during Run II, with tails beyond 60: that was the consequence of the increased luminosity. Complex analysis techniques are required to mitigate all unwanted effects of the pileup interactions [22].

2.2.2 Further improvements

The years from 2010 to 2013 have seen the first Run of the LHC: in early 2013 beam operation was stopped for a 2-year long shutdown (LS1). The goal for the first shutdown was to complete work on the magnets aiming at reaching the design beam energy. Linked to the PU, one of the principal requests made by the experiments hosted by the LHC was about the bunch spacing claiming a 25 ns interval, as opposed to the 50 ns spacing used in 2011-2012 (see figure 2.6) . On the machine side, this posed additional challenges, thus, given the number of new territories that had to be explored, the following years became dedicated to preparing the machine for full luminosity production in 2016-2018, intending to collect over 100 fb^{-1} until the end of 2018 [23] [24].

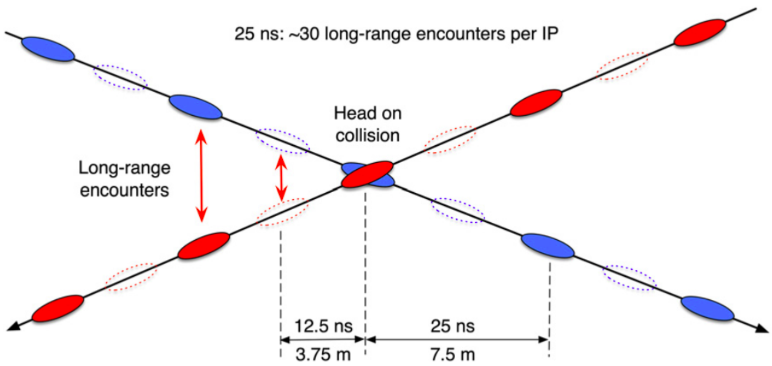

Figure 2.6: The minimum bunch spacing in the LHC is 25 ns (7.5 m) giving a maximum number of bunches of approximately 2800. Each bunch nominally contains approximately 1.20×10^{11} protons [22].

The year 2015 was devoted to establishing operation at 6.5 TeV per beam and with standard 25 ns bunch spacing. The first three months were focused on magnet powering tests and the magnet training campaign to establish a reliable and reproducible magnet performance at magnetic fields equivalent to 6.5 TeV beam energy. After a first period with the bunch spacing left to 50 ns, by mid-July 2017, the operation switched to 25 ns bunch spacing, initially with a reduced number of bunches to limit the total intensity and stored energy. The beam intensity was ramped up until the end of the year by increasing step-wise the number of bunches injected to 2244 bunches per beam [23].

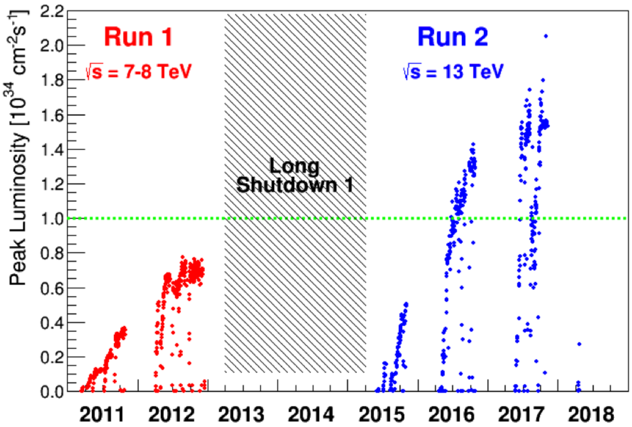

Figure 2.7: The peak luminosity of each fill as a function of the date. A few points have now been plotted for 2018, indicating the first steps of the intensity ramp-up phase. The green line indicates the LHC design luminosity [23].

In 2016, on 26 June the LHC attained its design luminosity of $1 \times 10^{34}\text{cm}^{-2}s^{-1}$. In parallel, the injector chain prepared a high brightness 25 ns beam, based on a Batch Compression Merging and Splitting (BCMS) scheme. The LHC used this beam successfully for production, resulting in a transverse emittance at the start of collisions of only 2 μm. In combination with a reduction of the half crossing angle from 185 μrad to 140 μrad in September led to a further increase of the peak luminosity, as can be observed in figure 2.7, with a record peak luminosity of $1.4 \times 10^{34}\text{cm}^{-2}s^{-1}$. The proton physics run ended on a very positive note with 40 fb^{-1} of integrated luminosity for ATLAS and CMS. The LHC continued running successfully for another 4 weeks with proton-lead collisions [23].

The second of November 2017 marked a new luminosity record of $2.6\times10^{34}\text{cm}^{-2}s^{-1}$. Unfortunately, the number of inelastic collisions per bunch crossing (PU), in the experiments ATLAS and CMS, was beyond acceptable, consequently, the instantaneous luminosity was levelled to $1.5 \times 10^{34}\text{cm}^{-2}s^{-1}$, using levelling by beam separation. 2017 proton physics run ended with a record integrated luminosity of 50 fb^{-1} [23].

The luminosity of 2017 was surpassed the following year. With the highest luminosity score at LHC, the 2018 proton physics run ended on 24 October and accumulated 66 fb^{-1} of integrated luminosity for ATLAS and CMS. The last month were dedicated to a 24-day lead-lead ion run at 6.37 TeV beam energy [22].

By the end of Run II, an integrated luminosity of 190 fb^{-1} had been delivered to both ATLAS and CMS, about 50% more than expected and almost 20 times the combined integrated luminosity delivered by all the world's hadron accelerators prior to the LHC [22].

When the second Run ended, in 2018, the second long shutdown started and it was exploited for major interventions which can be carried on only during multi-year shutdowns. One of these improvements, for instance, was the installation of an upgraded system of collimators, as requested by the LHC Injector Upgrade Project (LIU) parts of the HL-LHC upgrade [22].

2.2.3 Future perspective

The third Run has started in July 2022 and it is planned to last until the end of 2025; in the figure 2.8 the actual long time planner is shown. The principal aim of Run III is to collect a large amount of data at the foreseen centre of mass energy of $\sqrt{s} = 13.6$ TeV. The expected integrated luminosity at the end of Run III is forecasted to be of the order 150 fb^{-1} increasing the probability of observing the rarest physics events [22].

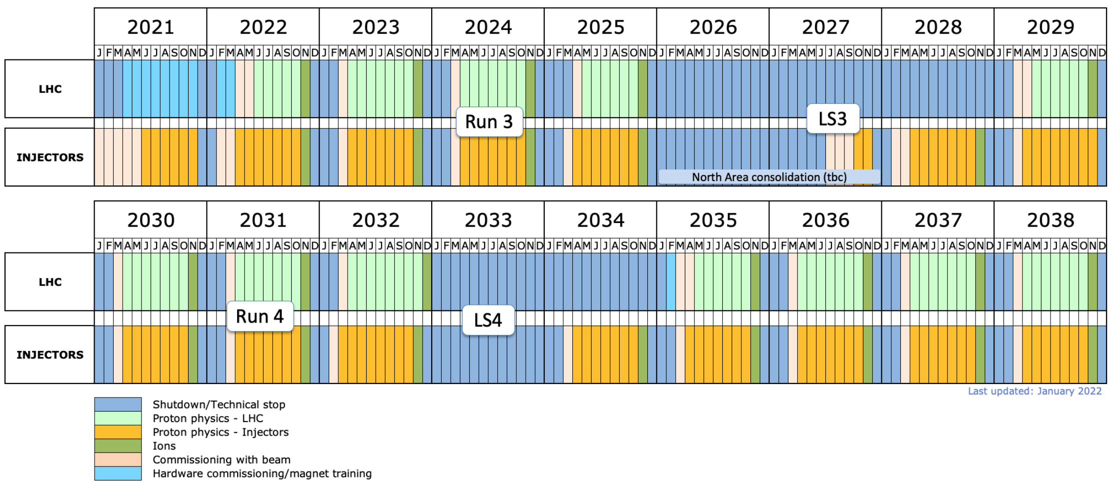

Figure 2.8: Actual schedule of LHC activities.

The first era of the LHC lifetime is expected to end with Run III: at the end of the run, during the third long shut down, all the major upgrades that will allow the beginning of the high luminosity era will take place. The High-Luminosity LHC (HL-LHC) will operate with the goal of increasing the integrated luminosity delivered to the experiments by an order of magnitude. Significant upgrades to the LHC itself and the detectors will be installed. Data taking with the HL-LHC configuration is planned to start in 2029 and continue until about 2040 [22].

The design of the HL-LHC targets the following key points:

- a significant lower β^* at the CMS and ATLAS interaction points: the β^*

is requested to go below 30 cm (the nominal value of the LHC is 55 cm). This implies a new approach for the machine optics and the corrections of chromatic aberration due to the large beta functions;

- a significant upgrade to the injectors to increase the bunch population while maintaining low beam size;
- the high bunch population will require a large crossing angle. This will lead to a loss of luminosity which will be countered by the use of novel crab radio frequency (RF) cavities.
- many measures to deal with the high level of collision debris and high radiation levels are foreseen on either side of the high luminosity experiments [22].

The goal of the HL-LHC upgrade project is to increase the luminosity of the LHC in order to deliver an integrated total luminosity of order 3000 fb^{-1} and allow for the potential accumulation of an integrated luminosity of up to 4000 fb^{-1} when using all engineering margins of the new HL-LHC configuration. The luminosity goals imply an annual integrated luminosity of 250 fb^{-1} [22]. At the same time, the experiments have asked for the number of events per bunch crossing, the event pileup, to be limited to around 140. This event pileup corresponds to a peak luminosity of $5 \times 10^{34}\text{cm}^{-2}s^{-1}$ [22]. Another goal is to extend the LHC machine lifetime by another decade beyond the LHC Run III operation period.

All the upgrades made to the collider machine must be followed by appropriate changes to the experimental setups.

2.3 Physics research at LHC

The LHC has undoubtedly become famous in mass culture thanks to the discovery of the Higgs boson, whose existence has been predicted by the Higgs mechanism almost fifty years before its discovery in 2012. Since its discovery, experiments at the LHC have focused on testing the Higgs boson's couplings to other elementary particles, precision measurements of the Higgs boson's properties and an initial investigation of the Higgs boson's self-interaction and shape of the its potential [25]. The Higgs bosons represented the last missing piece of the Standard Model, although it is firmly believed that the Standard Model is not a destination point: quite the contrary, it is just a starting point. That is the principal reason why the study of the Higgs boson has been the main goal of the experiments working at LHC: the precision tests on the Standard Model particles and their processes are fundamental to understand where the model fails. At the same time, the rarest events or the discovery of new processes may link the Standard Model to a wider theory, which could be able to explain what cannot be explained by the current theory, i.e. the neutrino mass.

2.3.1 Principal achievements

The aforementioned discovery of the Higgs boson has been one of the greatest achievements of the LHC. The CMS and ATLAS collaborations announced the discovery in 2012, exactly 48 years after the formulation of the mechanism that foreseen its existence. In 2013 Peter Higgs, Robert Brout and François Englert, the minds behind the Brout-Englert-Higgs mechanism, won the Nobel prize for their brilliant intuition. The Higgs boson is a fundamental scalar boson, as opposed to all other vector bosons transmitting interactions, photons, gluons, and $W^{\pm}$ and Z^0 bosons, with a mass of $m = 125.10 \pm 0.14$ GeV/c^2 [25]. At the LHC energies, the Higgs boson is mostly produced by gluon-gluon fusion; its reconstruction, because of experimental limits, has initially been performed in two different golden channels: $H \to \gamma\gamma$ and $H \to ZZ \to 4l$ [25] [26] although they are not the most probable final states. An example of the reconstructed signal in the two different channels obtained by the CMS Collaboration is shown in figure 2.9 [27]. The announcement from ATLAS and CMS was based on the data collected in Run I, which was sufficient for both experimental collaborations to claim independently the observation of a new particle. The observation was made with a significance of the result of more than five standard deviations, 5σ, away from a background-only result, meaning that the chance of this result being due to a fluctuation of the background is less than 1 in 3'500'000 [25].

With its higher statistic, Run II has been exploited by the CMS and ATLAS Collaborations to deeply study the Higgs boson proprieties and coupling constants with the help of new processes that were not accessible during the first Run. For instance, the decay of the Higgs boson into charged fermions was a key physics target for the LHC Run II since it is a direct test of the SM [20]. Decays to all fermions are kinematically allowed except for the decay into a top plus anti-top quark pair. An important check is the quantitative comparison of the coupling strengths to the different fermions, which for the quantum particle associated with the Englert-Brout-Higgs field in the SM are expected to be proportional to the masses of the respective fermions. No particularly evidence of disagreement with the Standard Model predictions can be appreciated so far in the Higgs sector [25] [26].

Both Run I and Run II data were used to stress the Standard Model predictions in many different channels, i.e. the processes involving the top quark. The top

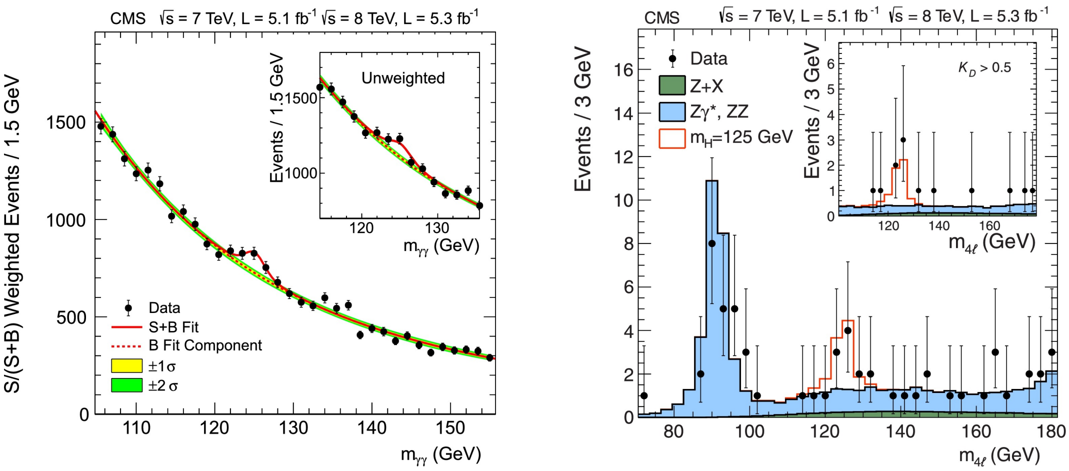

Figure 2.9: (Left) The diphoton invariant mass distribution with each event weighted by the S/(S + B) value of its category. The lines represent the fitted background and signal, and the coloured bands represent the ±1 and ±2 standard deviation uncertainties in the background estimate. (Right) Distribution of the four-lepton invariant mass for the $ZZ \to 4l$ analysis. The points represent the data, the filled histograms represent the background, and the open histogram shows the signal expectation for a Higgs boson of mass, added to the background expectation. [27]

quark with its mass of almost 173 GeV$/c^2$ is the heaviest particle among the quarks, thereby it can play a key role in the electroweak symmetry breaking, being a good probe for the searching for new physics. At the same time, in the flavour physics sector, several measurements have been carried out confirming the prediction about the flavour mixing, CP violation and rare decays [20] [26]. In fact, another huge sector of research for the LHC experiments is represented by flavour physics: understanding the structure and the origin of flavour phenomena in the quark sector is one of the big open challenges of particle physics. The search for new sources of CP violation, beyond those present in the CKM mixing matrix, underlies the efforts to explain the baryon asymmetry of the universe. The rare $B_s \to \mu\mu$ decay, with a rate of approximately 3×10^{-9}, has been discovered by the LHCb, CMS and ATLAS experiments [28]. The rarer $B_d \to \mu\mu$ decay is still unobserved, but its expected almost 10^{-10} rate is within reach. These two results alone had a big impact on constraining the parameter space of several beyond Standard Model (BSM) theories, notably supersymmetry, and their precision and BSM sensitivity will continue improving. Another important achievement is the discovery of the DD mixing by the LHCb collaboration and the long-elusive CP violation in D-meson decays. Although, the large hadronic non-perturbative uncertainties make the interpretation of these results particularly challenging, leaving under debate whether the measured properties are consistent with the SM, or signal new physics. But the experimental findings are a textbook milestone in the worldwide flavour physics programme [29].

2.3.2 Future goals

In May 2022 Run III has finally begun: it is expected to collect a high amount of data which will be helpful, thanks to a higher statistic, to improve the final states already investigated and for the search of never observed events.

Nevertheless, the step change for the LHC is expected to be the High Luminosity era. Indeed, along with improving the precision of Higgs sector measurements, the substantial luminosity of HL-LHC will make it possible to probe fundamental rare processes involving the Higgs boson. Some examples involving rare decays might be $H \to Z\gamma$, or those involving second-generation fermion couplings, which can open a novel window on the problem of flavour. Finally, the HL-LHC may have the potential to study di-Higgs production. A study of the Higgs boson self-coupling provides a test on the association between the actual vacuum and the Higgs potential, because the self-coupling is related to the third derivative of the Higgs potential at its minimum, uniquely predicted in the Standard Model [30]. One main avenue for studying self-coupling is through di-Higgs production, which is sensitive to the (off-shell) $H^* \to HH$ process. It should be noted, however, that this interferes with other mechanisms for the production of two Higgs bosons, which complicates the determination of the self-coupling. Furthermore, new physics can modify the relation between the Higgs potential and di-Higgs production; for example, di-Higgs production can be greatly enhanced in cases where the Higgs is composite rather than elementary. The compositeness of the Higgs boson is one of the key predictions of the Composite Higgs Model [20]. The importance of the study of the Higgs sector derives from one particular important shortcoming of the SM given the recent discovery of a relatively low mass Higgs boson is that the mass of a scalar particle such as the Higgs receives large radiative corrections, on the order of Planck mass [30].

The SM does not provide answers to several of the fundamental questions in particle physics including the nature of the dark mass or why matter and antimatter differ. Also can not unify all the forces and explain how QCD behaves under extreme conditions. In addition, one of the most pressing questions in particle physics is, therefore, whether or not there exist new particles around the TeV scale which stabilise the Higgs mass and cancel the quadratic divergences in the Higgs sector [30]. One of the favoured models beyond the SM is Supersymmetry (SUSY). SUSY is a hypothetical new symmetry of nature that relates fermions and bosons and suggests partner particles, called sparticles. The cross sections for strongly produced sparticles are relatively large, cross sections for electroweak particles like neutralinos and charginos are several orders of magnitude smaller and thereby benefit significantly from the large integrated luminosity provided by the HL-LHC. Finally, the study of the Higgs boson properties offers compelling perspectives for testing the effects of SUSY. This is particularly the case in the context of supersymmetric theories and its minimal version, the Minimal Supersymmetric Standard Model (MSSM). The Higgs couplings to SM particles, both at tree level and through loops, are sensitive to new physics effects and can be used to discriminate the MSSM h from the SM H [31].

To date, there is no evidence for the existence of the supersymmetric partners, but thanks to the higher luminosity of the HI-LHC might be possible to observe new processes that can guide us in the formulation, or the validation or not of theories beyond the SM.

Chapter 3

The CMS experiment

The prime motivation of the LHC was to elucidate the nature of electroweak symmetry breaking for which the Higgs mechanism was presumed to be responsible. As largely explained in the previous chapter, the experimental study of the Higgs mechanism can also shed light on the consistency of the Standard Model. Also, various alternatives to the Standard Model invoke new symmetries, new forces or constituents not discovered yet. Furthermore, all the experiments have been projected and realized to meet the goals of the LHC.

One of the experiments operating at the LHC is the Compact Muon Solenoid (CMS) detector which is a multi-purpose apparatus. The CMS detector is installed about 100 metres underground close to the French village of Cessy, between Lake Geneva and the Jura mountains [32].

The main measurement goals that drove the CMS design can be summarised as follows:

- good muon identification and momentum resolution over a wide range of momenta and angles, good dimuon mass resolution ($\approx 1\%$ at 100 GeV), and the ability to determine unambiguously the charge of muons with $p < 1$ TeV;
- good charged-particle momentum resolution and reconstruction efficiency in the inner tracker. Efficient triggering and offline tagging of τ's and b-jets, requiring pixel detectors close to the interaction region. Good primary vertex reconstruction;
- good electromagnetic energy resolution, good diphoton and dielectron mass resolution ($\approx 1\%$ at 100 GeV), wide geometric coverage, π_0 rejection, and efficient photon and lepton isolation at high luminosities;
- good missing-transverse-energy and dijet-mass resolution, requiring hadron calorimeters with a large hermetic geometric coverage and with fine lateral

segmentation [32].

The detector gets its name thanks to its ability to detect *muons* very accurately in a small volume thanks to the presence of the most powerful *solenoid* magnet ever made. In addition, with a height of 15 meters and a length of 21 meters, in opposition to its weight of 14'000 t, it gains the epithet of *compact*.

3.1 Overview of the experiment

In this paragraph an overview of the CMS experiment is presented: each component will be deepened in the following sub-paragraphs.

Before going into details, it is important to keep in mind the coordinate system adopted by the CMS experiment:

- the origin is centred at the nominal collision point inside the experiment;
- the y-axis pointing vertically upward;
- the x-axis pointing radially inward toward the centre of the LHC;
- the azimuthal angle ϕ is measured from the x-axis in the x-y plane;
- the radial coordinate in the x-y plane is denoted by r;
- the polar angle θ is measured from the z-axis.

Consequently, the momentum and energy transverse to the beam direction, denoted by p_T and E_T, respectively, are computed from the x and y components; the imbalance of energy measured in the transverse plane is denoted by E_T^{miss}. Another important parameter is the pseudorapidity which is defined as $\eta = -ln(tan(\theta/2))$ [32]. A schematic of the coordinate system is shown in figure 3.1.

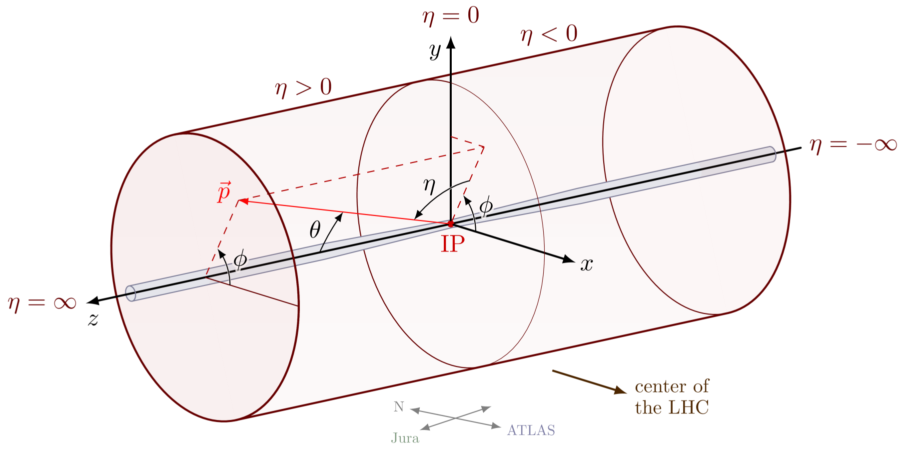

Figure 3.1: Schematic of the coordinate system for the CMS experiment.

The core of the CMS experiment is the tracking system: the tracking volume is a cylinder of 5.8 m length and 2.6 m diameter. A sketch of the CMS tracker is shown in figure 3.3.To deal with the high track multiplicities, CMS employs 10 layers of silicon microstrip detectors, which provide the required granularity and precision. Meanwhile, to improve the measurement of the impact parameter of charged-particle tracks, as well as the position of secondary vertices, there are also 4 layers of silicon pixel detectors, which are placed close to the interaction region [32]. Externally to the tracking system, there are the electromagnetic calorimeter and the hadronic calorimeter. The electromagnetic calorimeter (ECAL) uses lead tungstate (PbWO4) crystals with coverage in pseudorapidity up to $|\eta| < 3.0$. The scintillation light is detected by silicon avalanche photodiodes (APDs) in the barrel region and vacuum phototriodes (VPTs) in the endcap region. A preshower system is installed in front of the endcap ECAL for π_0 rejection. The ECAL is surrounded by a brass/scintillator sampling hadron calorimeter (HCAL) with coverage up to $|\eta| < 3.0$. This central calorimetry is complemented by a tail-catcher in the barrel region (HO) ensuring that hadronic showers are sampled with nearly 11 hadronic interaction lengths. Coverage up to a pseudorapidity of 5.0 is provided by an iron/quartz-fibre calorimeter [32].

A crucial aspect driving a detector of this type is the design and layout of the magnetic field configuration. The magnetic field configuration is relevant for measuring the momentum of charged particles. In fact, a large bending power is needed to measure precisely the momentum of high-energy charged particles. At the heart of CMS sits a 13 m long, 6 m inner-diameter, 4-T superconducting solenoid providing a large bending power (12 Tm) before the muon bending angle is measured by the muon system. The return field is large enough to saturate

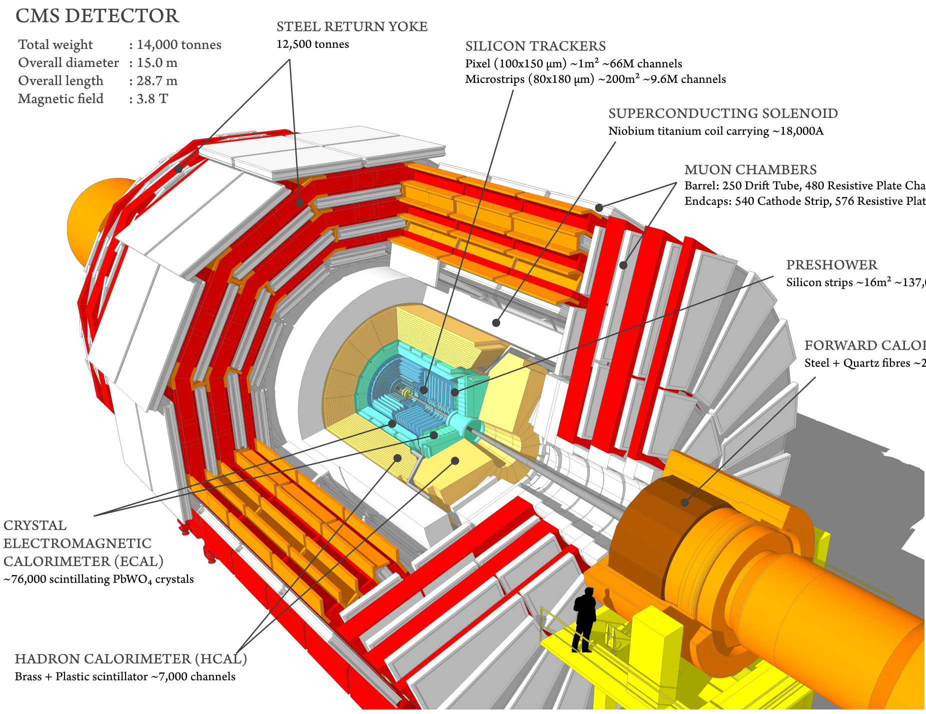

Figure 3.2: A perspective view of the CMS detector.

1.5 m of iron, allowing 4 muon stations to be integrated to ensure robustness and full geometric coverage. Each muon station consists of several layers of aluminium drift tubes (DT) in the barrel region and cathode strip chambers (CSC) in the endcap region, complemented by resistive plate chambers (RPC). The bore of the magnet coil is large enough to accommodate the inner tracker and the calorimetry inside [32]. The overall layout of CMS is shown in figure 3.2.

3.1.1 Tracker

As the name suggests, the tracker system is the part of the experiment dedicated to the reconstruction of the track of the charged particles. Thanks to their charge, the trajectory of charged particles can be blended under magnetic force. In its classical formulation, the Lorentz's force reads:

$$\vec{F}_L = m\frac{d^2\vec{x}}{dt^2} = q \cdot (\vec{v} \times \vec{B}), \tag{3.1}$$

at the same time, the particles are also subject to the centrifuge force that is:

$$\vec{F}_c = \frac{mv^2}{r}\hat{r}. \tag{3.2}$$

The two forces are in equilibrium, thus the radius can be obtained as:

$$\vec{r} = \frac{m \cdot v}{q \cdot B}\hat{r}. \tag{3.3}$$

It is now clear how information on the charge and the momentum can be deducted by the track measurement and, thereby, to have a high precision measurements of the trajectory means to have a high resolution on the momentum reconstruction. Another crucial point for the tracker is the large amount of signal per bunch crossing which means that a detector technology featuring high granularity and fast response is required, such that the trajectories can be identified reliably and attributed to the correct bunch crossing. At the same time, these features imply a high power density of the on-detector electronics which in turn requires efficient cooling; that is in direct conflict with the aim of keeping to the minimum the amount of material to limit multiple scattering, Bremsstrahlung, photon conversion and nuclear interactions. A compromise to fulfil all the requirements on granularity, speed and radiation hardness led to a tracker design entirely based on silicon detector technology. The CMS tracker was initially composed of a pixel detector with three barrel layers at radii between 4.4 cm and 10.2 cm and a silicon strip tracker with 10 barrel detection layers extending outwards to a radius of 1.1m. Each system was completed by endcaps which consisted of 2 disks in the pixel detector and 3 plus 9 disks in the strip tracker on each side of the barrel, extending the acceptance of the tracker up to a pseudorapidity of $|\eta| < 2.5$ [32].

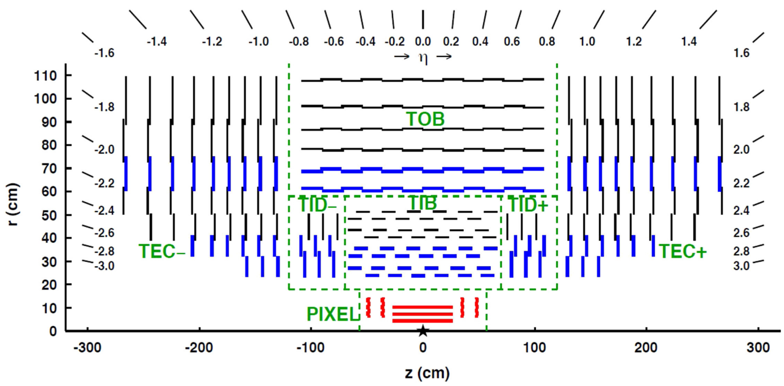

Figure 3.3: Sketch of the CMS tracker detector. Pixel modules are shown in red, single-sided strip modules are depicted as black thin lines and strip stereo modules are shown in blue thick lines.

To fulfil the reconstruction demands, the inner tracker surrounds the interaction point and had a length of 5.8 m and a diameter of 2.5 m for a total of 1440 pixel and 15148 strip detector modules. The high number of particles per bunch crossing led to a hit rate density of 1 MHz/mm^2 at a radius of 4 cm, falling to 60 kHz/mm^2 at a radius of 22 cm and 3 kHz/mm^2 at a radius of 115 cm. To keep the occupancy, namely the number of particles traversing a detector cell per event, at or below 1%, pixelated detectors had to be used at radii below 10 cm. For a pixel size of 100×150 μm^2 in r-ϕ and z, respectively, the occupancy was of the order 10^{-4} per pixel and LHC bunch crossing. At intermediate radii (20 cm $<$ r $<$ 55 cm) the reduced particle flux allowed the use of silicon micro-strip detectors with a typical cell size of 10 cm×80μm, leading to an occupancy of up to 2-3% per strip and LHC bunch crossing. In the outer region (55 cm $<$ r $<$ 110 cm) the strip pitch could be further increased [32]. It was designed for a maximum instantaneous luminosity of $1 \times 10^{34} cm^{-2} s^{-1}$ and a maximum average pileup (number of inelastic interactions per bunch crossing) of 25 in LHC operation with 25 ns bunch spacing. With the upgrade of the accelerators during the first long shutdown (LS1, 2013–2014), these parameters have been exceeded and the luminosity and pileup have more than doubled compared to the design values. In order to maintain efficient and robust tracking at CMS under these conditions, the original pixel detector has been replaced by a new system, referred to as the CMS Phase-1 pixel detector.The layout of the CMS Phase-1 pixel detector is optimized to have four-hit coverage over the pseudorapidity range $\eta < 2.5$, improved pattern recognition and track reconstruction, and added redundancy to cope with hit losses. During LS1, a new beam pipe with a smaller radius of 23 mm, compared to a radius of 30 mm of the original beam pipe, was installed in CMS. This allowed for placement of the innermost layer of the CMS Phase-1 pixel detector closer to the interaction point compared to the original pixel detector. The CMS Phase-1 pixel detector consists of four concentric barrel layers (L1-L4) at radii of 29, 68, 109, and 160 mm, and three disks (D1-D3) on each end at distances of 291, 396, and 516 mm from the center of the detector. The layout of the CMS Phase-1 pixel detector is compared to the one of the original pixel detector in figure 3.1.12. The total silicon area of the CMS Phase-1 pixel detector is 1.9 m^2 , while the total silicon area of the original pixel detector was 1.1 m^2. The CMS Phase-1 pixel detector is built from 1856 segmented silicon sensor modules, where 1184 modules are used in the barrel pixel detector (BPIX) and 672 modules are used for the forward disks (FPIX). Each module consists of a sensor with 160×416 pixels connected to 16 readout chips (ROCs). In total there are 124 million readout channels [33].

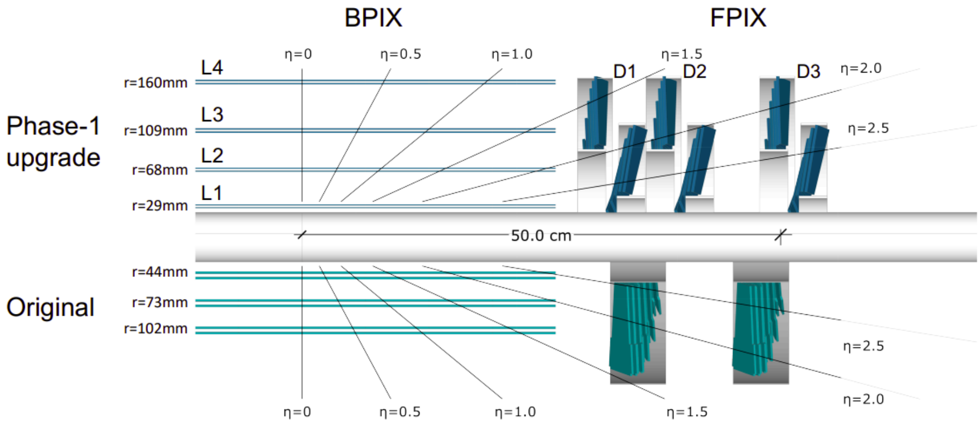

Figure 3.4: Layout of the CMS Phase-1 pixel detector compared to the original detector layout, in longitudinal view.

Outside the pixel detector, where the flux of particle is less intense, the tracker is completely composed of silicon strips [34]. Ten layers in the barrel region and twelve disks in the endcap are made of strips with a thickness of 300 μm in the inner part and 500 μm in the outer, for a total of 200 m^2 of active area with 15148 modules. The strip detector is based on single-sided and double-sided microstrip detectors with AC-coupled p-type strips in an n-type bulk. The strip detector geometrical structure is divided into four regions. The Tracker Inner Barrel (TIB) and Disk (TID) cover a region limited in $r < 55$ cm and $|z| < 118$ cm and are made of four longitudinal layers and three transverse disks. They guarantee a resolution in $r\phi$ between 13-38 μm [35]. In the outer region there is the Tracker Outer Barrel (TOB) that covers the region $r > 55$ cm and $|z| < 118$ cm, consisting of six layers and providing a $r\phi$ resolution between 18-47 μm. Finally in the endcap region the Tracker EndCaps (TEC) covers the range $124 < |z| < 282$ cm and is made of nine disks in each side. Each disk contains seven rings of strips and has the same resolution of TOB. In the barrel region the single strips are arranged parallel to the beam direction with a distance between each other varying from 80 μm innermost to 183 μm outermost. In the endcap region the sensors have a step from 81 μm at small radius to 205 μm for larger radii. Each substructure has been designed for the specific position occupied within the detector. The strip detector is read-out by a 250 nm CMOS Readout Chip, called APV. Each APV handles 128 strip channels with a read-out rate of 100 kHz [36].

3.1.2 Electromagnetic calorimeter - ECAL

Calorimeters are classified into two classes: homogeneous and inhomogeneous. The main difference between them is the sampling fluctuations, larger in the latter case, which can critically affect the energy resolution.

The CMS electromagnetic calorimeter (ECAL) is a hermetic, homogeneous, fine-grained lead tungstate (PbWO4) crystal calorimeter [37]. The choice fell on a homogeneous medium to obtain a better energy resolution: high-density crystals offer the potential to achieve the required performance and compactness and allow the calorimeter to be fast, have a fine granularity and be radiation resistant. In addition, the CMS design enabled the electromagnetic calorimeter to fit within the volume of the CMS superconducting solenoid magnet. All the features just mentioned are crucial in the LHC environment. Finally, another of the driving criteria in the design was the capability to detect the decay into two photons of the postulated Higgs boson [37] [32].

The 75 848 crystals are arranged in a central barrel section (EB), with pseudo-rapidity coverage up to $|\eta| = 1.48$, closed by two endcaps (EE), extending coverage up to $|\eta| = 3.0$. A preshower detector is placed in front of the endcap crystals. Avalanche photodiodes (APDs) are used as photodetectors in the barrel and vacuum phototriodes (VPTs) in the endcaps [37]. The spatial arrangement is shown in the figure 3.5.

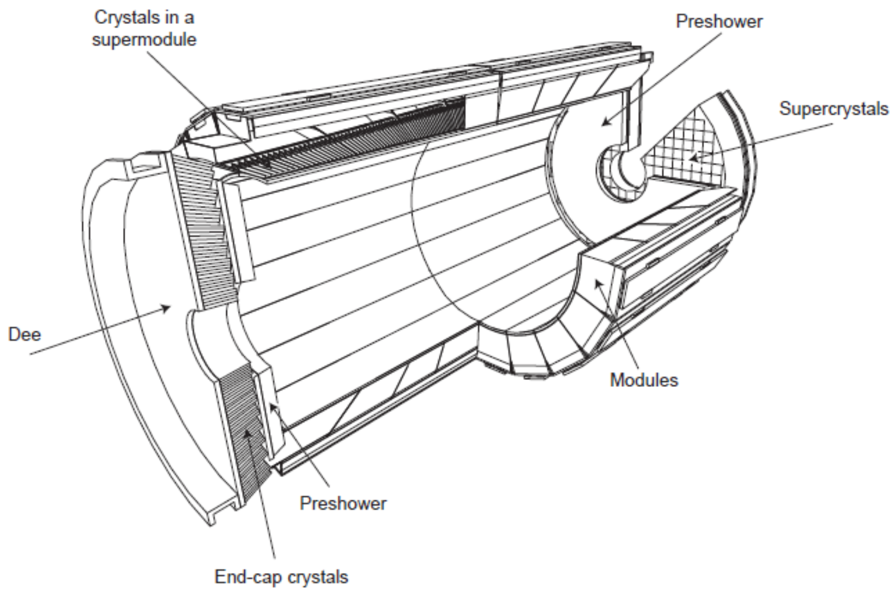

Figure 3.5: Spatial arrangement of the electromagnetic calorimeter parts.

The calorimeter has no longitudinal segmentation, thus the measurement of the photon angle relies on the primary vertex reconstruction from the silicon tracker. The crystal length in EB is 230 mm (220 mm in EE) corresponding to 26 (25) radiation lengths, meanwhile, the transverse size of the crystals at the front face is 2.2×2.2 cm^2 in EB (2.86×2.86 cm^2 in EE). The total crystal volume is 11 m^3 and the weight is 92 t. Each of the 36 supermodules in the barrel contain 1,700 crystals, while the endcaps consist of two dees, with 3,662 crystals each. The pre-shower detector (ES), based on lead absorber and silicon strips sensors (4,288 sensors, 137,216 strips, 1.90×61 mm^2 with x-y view), placed in front of the endcaps at $1.65 < |\eta| < 2.6$, improves the photon-π_0 separations. The total thickness of the ES is 3 radiation lengths [37]. The obtained energy resolution, for the central impact of electrons on a 3 × 3 crystal array, has a stochastic, noise and a constant term: $\sigma_E/E = 2.8\%/\sqrt{E} \oplus 0.128\ GeV/\sqrt{E} \oplus 0.3\%$ where E is measured in GeV. The constant term is dominated by the longitudinal non-uniformity of light collection. The energy resolution can also be affected by the photon conversion and electron Bremsstrahlung. The time resolution is also excellent (<100 ps for E>20 GeV); it has been measured at beam tests using the time difference between adjacent crystals belonging to the same electromagnetic shower. The ECAL time information can be exploited as an alternative method to determine the position of the primary vertex, namely the reconstructed location of an individual particle collision, in events with low track multiplicity [37].

3.1.3 Hadronic calorimeter - HCAL

The CMS detector is designed to study a wide range of high-energy processes involving diverse signatures of final states, in particular, the hadron calorimeters are relevant for the measurement of hadron jets and neutrinos or exotic particles resulting in apparent missing transverse energy. More specifically, the hadronic calorimeter (HCAL) is used to measure the timing and energy of hadronic showers, as well as their angle and position, needed for the generation of level-1 trigger primitives, the high-level trigger, and offline reconstruction of jets and missing transverse energy [32]. The hadron calorimeter barrel and endcaps usually sit behind the tracker and the electromagnetic calorimeter as seen from the interaction point: that is because the hadrons are less likely to interact with the previous inner detectors, contrariwise to lighter particles, such as electrons or positrons. The HCAL barrel of CMS is radially restricted between the outer extent of the electromagnetic calorimeter (r = 1.77 m) and the inner extent of the magnet coil (r = 2.95 m). The main consequence is the constraint on the total amount of material that can be implied to absorb the hadronic shower, limiting the probability of interaction. Hence, to complement the barrel calorimeter an outer hadron calorimeter or tail catcher has been placed outside the solenoid. Beyond $|\eta| = 3$, the forward hadron calorimeters placed at 11.2 m from the interaction point extend the pseudorapidity coverage down to $|\eta| = 5.2$ using a Cherenkov-based, radiation-hard technology [32]. A schematic view of the placement and structure of the HCAL is shown in figure 3.6.

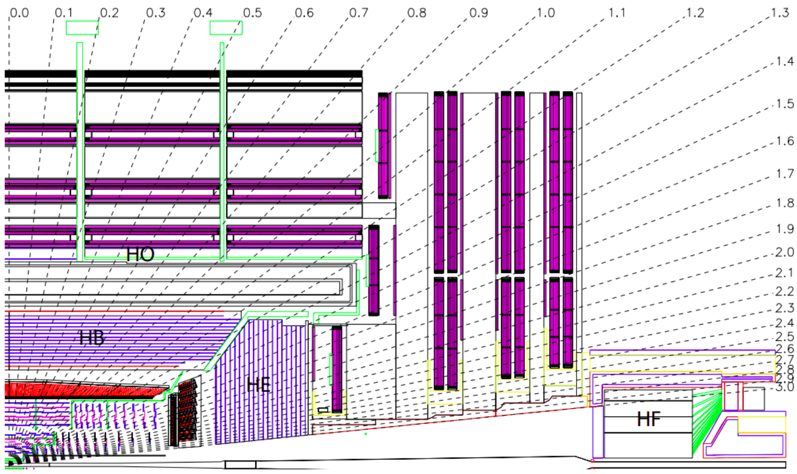

Figure 3.6: Longitudinal view of the CMS detector where the constituents of the hadronic calorimeter are indicated.

The hadronic calorimeter has been designed to reach an energy resolution of $100\%/\sqrt{E} \oplus 5\%$ where E is in GeV.

3.1.4 Solenoid

As already explained in the subparagraph 3.1.1, the magnetic field gives the particle trajectories in the tracking detector a curvature, which depends on the magnetic flux density B. A higher magnetic flux density provides a larger curvature and, as a result, a more accurate measurement of the momentum of a charged particle [38].

The CMS Detector uses a magnetic field provided by a wide-aperture superconducting thin solenoid with a diameter of 6 m and a length of 12.5 m, where a central magnetic flux density $|B_0|$ of 3.8 T is generated by an operational direct current of 18.164 kA. The superconducting solenoid is made of NbTi, meanwhile, the magnetic flux return yoke is made of construction steel containing up to 0.17% carbon and up to 1.22% manganese, as well as small amounts of silicon, chromium, and copper. The solenoid is installed in a vacuum cryostat in the central four-layer barrel wheel of the magnet yoke and creates a magnetic flux of 130 Wb. In the magnet yoke, are also included two three-layer barrel wheels around the solenoid cryostat on each side of the central barrel wheel, two nose disks inside each end of the solenoid cryostat, and four endcap disks on each side of the cryostat [38]. A schematic of both the longitudinal and transverse sections is shown in figure 3.7.

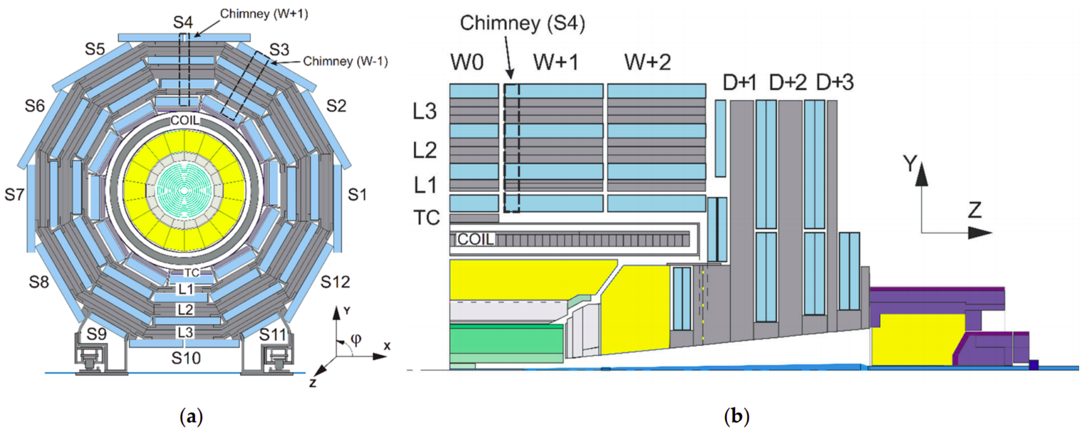

Figure 3.7: A schematic view of the CMS detector in transverse (a) and longitudinal (b) sections, where: S1-S12 are the detector azimuthal sectors, TC and L1-L3 are the layers of the yoke barrel wheels (W) and D is the yoke endcap disks.

Only two-thirds of the solenoid magnetic flux passes through the cross sections of the magnet yoke. The remaining third of the magnetic flux creates a stray magnetic field around the magnet yoke: the intensity decreases with a radius around the solenoid axis and with a distance along the axis. Hence, while at a radius of 50 m from the coil axis in the central plane of the detector, the value of the magnetic flux density is 2.1 mT, at a distance of 50 m from the centre of the solenoid along its axis, the value of the magnetic flux density becomes 0.6 mT [38].

3.1.5 Muons chambers

Muon detection is a powerful tool for recognizing signatures of interesting processes over the very high background rate expected at the LHC with full luminosity. Therefore, as is implied by the experiment's middle name, the detection of muons is of central importance to CMS: precise and robust muon measurement was a central theme from its earliest design stages [32].

In the CMS experiment, muons are reconstructed thanks to the information collected by both the tracking system and the dedicated muons chambers. The muons chambers, as can be easily guessed, owe their name to the ability to detect

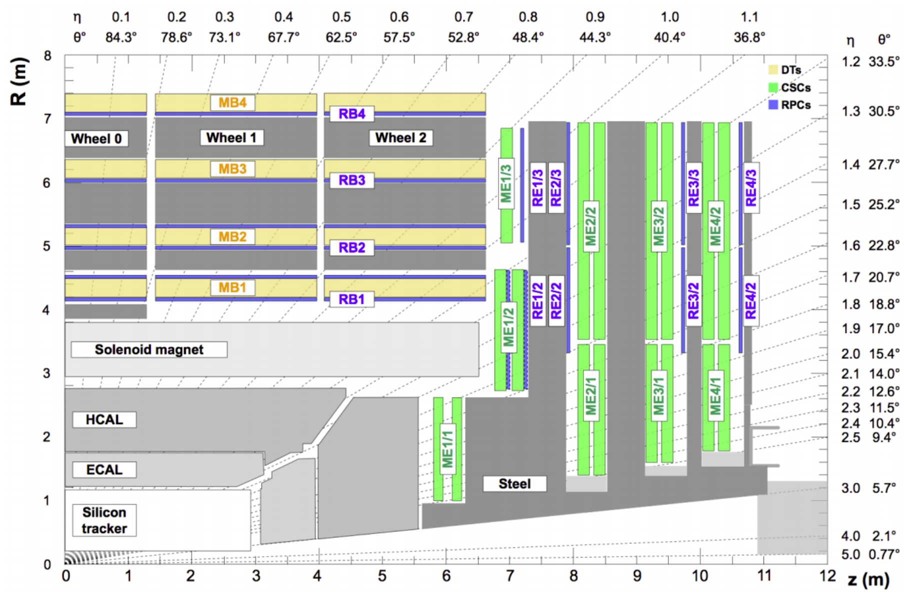

Figure 3.8: In figure is shown a schematic of the muon system, here the drift tube stations (DTs) are labeled MB ("Muon Barrel") and the cathode strip chambers (CSCs) are labeled ME ("Muon Endcap"). Resistive plate chambers (RPCs) are mounted in both the barrel and endcaps of CMS, where they are labeled RB and RE, respectively.

the passage of muons and, in order to have high efficiency in the muon detection, three types of gas ionization chambers have been chosen: drift tube chambers (DTs), cathode strip chambers (CSCs), and resistive plate chambers (RPCs). The chambers are independently-operating units and to match the cylindrical geometry of the solenoid, the barrel region is instrumented with drift tube chambers and the two endcap regions with cathode strip chambers, meanwhile the resistive plate chambers are interspersed in both the barrel and endcap regions, forming a redundant trigger system (see figure 3.8).

The DTs are segmented into drift cells; the position of the muon is determined by measuring the drift time to an anode wire of a cell with a shaped electric field. The DTs are organized into 12 ϕ-segments per wheel forming 4 stations and each station consists of 8 layers of tubes measuring the position in the bending plane and 4 layers in the longitudinal plane. The basic element of the DT system is the drift cell: it has a transverse size of 42×13 mm^2 with a 50 μm -diameter gold-plated stainless-steel anode wire at the centre. The wire operates at a voltage of +3600 V. The gas mixture (85%/15% of Ar/CO2) provides good quenching properties and a saturated drift velocity of about 55 $\mu m/ns$ [39] [40].

The CSCs operate as standard multi-wire proportional counters but add a finely segmented cathode strip readout, which yields an accurate measurement of the position of the bending plane (R-ϕ) coordinate at which the muon crosses the gas volume. The CSCs have been chosen thanks to their fast response time (resulting from a short drift path), in addition, they can be finely segmented and also can tolerate the non-uniformity of the magnetic field. Each endcap has 4 stations of chambers mounted on the faces of the endcap steel disks perpendicular to the beam. A CSC consists of 6 layers, each of which measures the muon position in 2 coordinates: the cathode strips provide a precision measurement in the r-ϕ bending plane, meanwhile, the wires provide a coarse measurement in the radial direction [39] [40].

The RPCs are double-gap chambers operated in avalanche mode and are primarily designed to provide timing information for the muon trigger. Each gap consists of two 2-mm-thick resistive bakelite plates separated by a 2-mm-thick gas gap. The outer surface of the bakelite plates is coated with a thin conductive graphite layer, and a voltage of about 9.6 kV is applied. The RPCs are operated with a 3-component, non-flammable gas mixture that consists of 95.2% Freon (C2H2F4, known as R134a), 4.5% isobutane (i-C4H10), and 0.3% sulphur hexafluoride (SF6). Readout strips are aligned in η in between the 2 gas gaps [39] [40].

The DT and CSC chambers are located in the regions $|\eta| < 1.2$ and $0.9 < |\eta| < 2.4$, respectively, and are complemented by RPCs in the range $|\eta| < 1.9$. The chambers are arranged to maximize the coverage and to provide some overlap where possible [39].

3.1.6 Trigger and DAQ system

Any experiment that collects a large amount of data needs a trigger system to discriminate events of physics interest from the background ones before the acquisition and analysis. In each bunch crossing, a plethora of interactions take place, thereby billion of signals should be detected, saved and analyzed in principle, but using a trigger system a first selection is possible. In the case under exam, the trigger system consists of two levels designed to select events of potential physics interest from a GHz (MHz) interaction rate of proton-proton (heavy ion) collisions [41].

The first level (L1) of the trigger is implemented in hardware and selects events containing detector signals consistent with an electron, photon, muon, τ lepton, jet, or missing transverse energy. A programmable menu of up to 128 object-based algorithms is used to select events for subsequent processing. One of the important characteristics a good trigger should have, besides the robustness, is adaptability: the trigger thresholds can be adjusted to the LHC instantaneous luminosity during data taking. This feature allows restricting the output rate to 100 kHz, the upper limit imposed by the CMS readout electronics. The L1 trigger goal is to decide if an event should be tentatively accepted or rejected using information from the calorimeter and muon detectors with a fixed latency: the time is fixed to $4\mu s$. The trigger primitives (TP) from ECAL and HCAL and the muon chambers are processed in several steps before the combined event information is evaluated in the global trigger (GT) and a decision is made whether to accept the event or not [41]. A schematic of the logic system can be appreciated in figure 3.9. The L1 calorimeter trigger comprises two stages: a regional calorimeter trigger

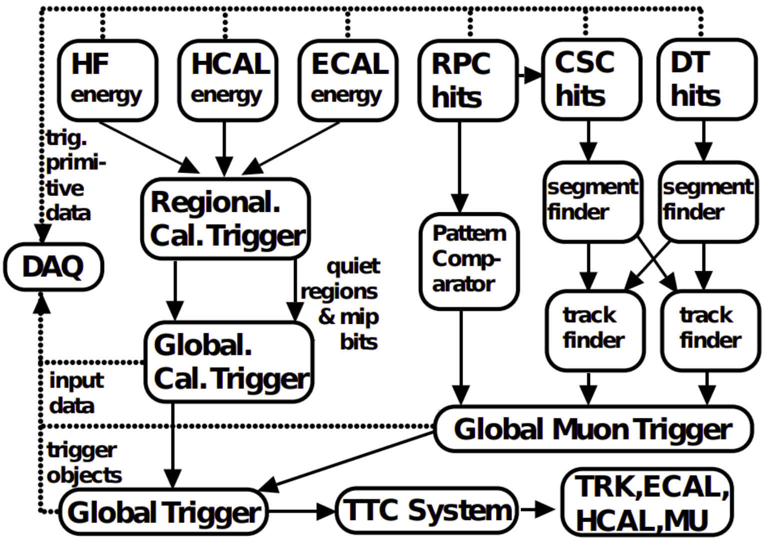

Figure 3.9: Schematic of the trigger logic.

(RCT) and a global calorimeter trigger (GCT). The RCT receives the transverse energies and quality flags from over 8000 ECAL and HCAL towers, giving trigger coverage over $|\eta| < 5$. In parallel, the RCT processes this information and sends as output e/γ candidates and regional E_T sums based on 4×4 towers. The GCT sorts the candidates who passed the first selection further, finds jets (classified as central, forward, and tau) using the E_T sums, and calculates global quantities such as E_T^{miss}. It sends as output four e/γ candidates each of two types, isolated and nonisolated, four each of central, tau, and forward jets, and several global quantities. Finally, each of the three muon detector systems in CMS participates in the L1 muon trigger to ensure good coverage and redundancy. The GT is the final step of the CMS L1 trigger system and implements a menu of triggers, a set of selection requirements applied to the final list of objects required by the algorithms of the HLT algorithms to meet the physics data-taking objectives [41].

The second level, implemented in software, further refines the purity of the output stream, selecting an average rate of 400 Hz for offline event storage. This second selection is performed by the High-Level Trigger (HLT). The event selection at the HLT is performed in a similar way to that used in offline processing, thus for each event, objects such as electrons, muons, and jets are reconstructed and identification criteria are applied. The HLT hardware consists of a single processor farm composed of commodity computers, the event filter farm (EVF), which runs Scientific Linux. The event filter farm consists of filter builder units. In the builder units, individual event fragments from the detector are assembled to form complete events. The events are then reconstructed and a trigger filter is applied. Associated builder and filter units are located in a single multi-core machine and communicate via shared memory. In total, the EVF executed on approximately 13,000 CPU cores at the end of 2012 [41].

The task to convert from analogic to digital and transport information is entrusted to the Data Acquisition System (DAQ). Each detector sub-systems use different custom hardware to read out their detectors after an L1 accept. A common sender mezzanine board plugged onto the front-end driver (FED) board, is used to interface the sub-system readout with the DAQ and trigger. The number of FEDs per sub-system varies between 1 and 438 meanwhile the fragment sizes depend on the instantaneous luminosity (occupancy) and on the level of zero suppression. The system is designed for an average event size of 1 MB. The central DAQ runs online software on about 3000 PC used for buffering and data processing [42].

A general scheme of the CMS DAQ system is shown in 3.10.

3.2 Upgrades

As largely explained in the previous chapter, the long shutdowns are an opportunity to improve the accelerating machine; however changes to the detector systems must follow the LHC upgrades. An increased luminosity, i.e., means a larger number of events and an increased pile up and as a consequence, better performance is required of the subdetectors to maintain the desired accuracy in the reconstruction. During LS1 the CMS strip detector has been upgraded to operate at lower temperatures: a lower cooling plant set point aims to reduce those radiation damage induced effects that have a temperature dependence, such as the increase of the leakage current and the long-term increase of the depletion voltage (also called reverse annealing). To prevent humidity formation inside the detector, the tracker volume has been fully sealed and a new dry gas plant has been installed to provide

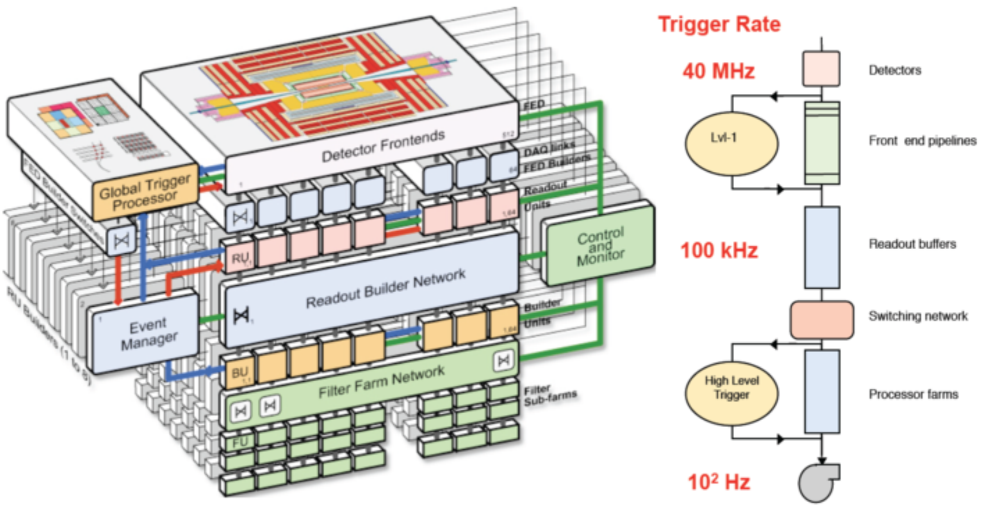

Figure 3.10: CMS DAQ system.

the tracker with the needed amount of dry gas. During LS1 the pixel detector has been extracted to repair damaged channels [43]. A new detector, the pixel luminosity telescope consisting of 8 telescopes, equipped with silicon pixel sensors, on both ends of the interactions point, was also installed. The Fast Beam Conditions Monitoring system, using diamond sensors, was upgraded to 24 sensors, 12 on each end of the IP. In addition, dedicated fast ASICs produced in 130 nm commercial CMOS technology and dead-time free backend electronics using FPGAs for fast signal processing have been developed and built. Also, the part of the forward HCAL used for the luminosity measurement was instrumented with new readout electronics [44]. Significant upgrades have been carried out also on the muon detectors and on the L1 muon trigger. In parallel, the algorithms for muon reconstruction and identification have been improved for both the High-Level Trigger and the offline reconstruction [45].

Further improvements have been made during the second LS looking forward to Run III and in preparation for the successive phase. In the following lines, some of the more major changes to the CMS detector are listed.

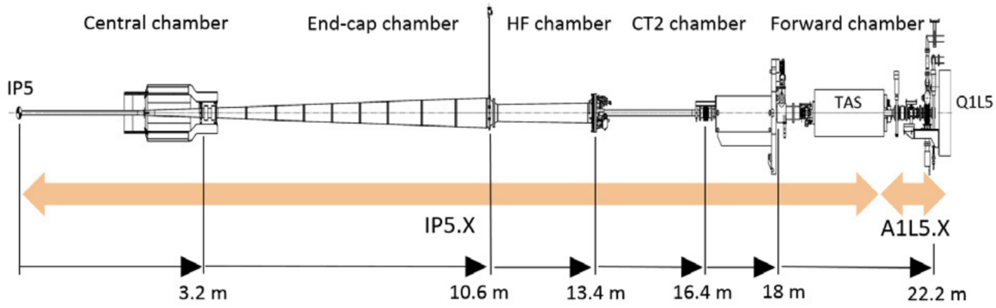

Figure 3.11: Initial CMS experimental vacuum layout.

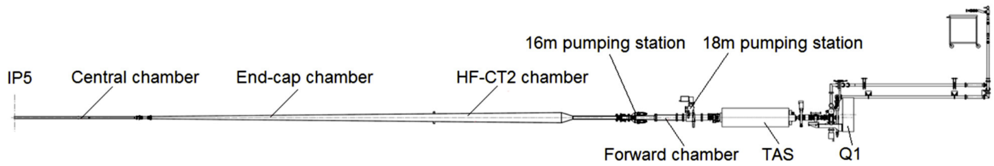

Figure 3.12: CMS experimental vacuum layout after the LS2 [46].

The front-end electronics of the CSC muon chambers in the end-cap regions have been changed to sustain HL-LHC trigger rates. This major LS2 work was completed in 2020, with a delay of a few months due to the COVID-19 pandemic. A new layer of high-granularity muon chambers based on Gas Electron Multipliers (GEM) has been installed, complementing the first station of muon chambers in the end-cap regions and aiming to cover the pseudo-rapidity range from 1.6 to 2.1 [47]. Together with another layer, to be integrated during LS3 to complement the second station, the GEM muon chambers will allow a reduction of the L1 trigger rate on muons in the forward regions by a factor of at least 10, as well as an improved trigger efficiency on forwarding displaced muons. Also, the Phase-1 upgrades of the hadronic calorimeter (HCAL) have been completed: these consisted of the replacement of the previous readout based on hybrid photo-diodes by a more efficient readout based on silicon photomultipliers, with a much improved longitudinal segmentation both in the barrel and end-cap regions [47]. A much lighter beam pipe has been installed, completely redesigned for the high luminosity phase of the LHC, this operation has been the biggest upgrade of the experiment's vacuum system since 2008 [46] [47]. The figures 3.11 and 3.12 show respectively the layout before and after the upgrade. Also, the pixel detector has been improved, including a new barrel layer closer to the interaction point, with more radiation tolerant electronics. Finally, a heterogeneous computing architecture in the High-Level Trigger (HLT) has been implemented, with a mixture of GPUs and CPUs, already yielding significant speed improvement [47]. Other significant changes are planned for the LS3, which temporally follows the third Run and precedes the HL-LHC era.

3.3 Physics research at CMS

To date, more than one thousand papers based on collision data had been published (or submitted) by CMS and some of them are a milestone for particle physics such as the article announcing world-famous discovery of the Higgs boson.

CMS tried to answer fundamental questions on the Standard Model, i.e the top quark mass which is a crucial parameter in several normalization schemes. To characterize the top quark, for instance, many alternative methods have been developed: an example is a measurement of the experiment top-quark mass in single-top events, which is quite precise in itself (0.77 GeV in total uncertainty) and in addition, allows separate measurements for the quark and antiquark mass [47]. Searches for the production of new heavy particles promptly decaying to pairs of leptons or vector bosons with the full Run II data set have been performed. In the latter case, one of the bosons is a W decaying leptonically, while the other one (W, Z or H) is boosted and detected as a merged jet with substructures. Many other searches are exploiting the novel boosted boson or top-quark detection techniques. CMS has also developed a systematic search for deviations from the Standard Model predictions in several hundred final states and kinematic distributions, in events containing at least one lepton. The B-physics also represents a huge sector of research for CMS, indeed the bottomonia allowed the study perturbation and lattice calculations of non-relativistic potentials, for instance, an analysis of 13-TeV data using 80 fb^{-1} of luminosity led to the first observation of the resolved $\chi_{b1}(3P)$ and $\chi_{b2}(3P)$ resonances [48]. Also the decays to $(Y(3S) \rightarrow \mu\mu)(\gamma \rightarrow ee)$ were considered; the separation was achieved after a photon-energy scale calibration that utilizes $\chi_b(nP)$ decays to $Y(nS)\gamma$ leading to a measured $Y(3S)\gamma$ invariant mass resolution of 2.2 MeV. To CMS goes also the merit to have observed for the first time the rare decay $Z \rightarrow J/\psi{+}l^+l^-$; such observation was performed with 35.9 fb^{-1} of 13 TeV data. Both direct production of J/ψ and through $\psi(2S) \rightarrow J/\psi + X$ were considered. The signal is extracted from an unbinned log-likelihood fit, resulting to 13±3.9(stat) $\mu^+\mu^-\mu^+\mu^-$ events and 11.2±3.4(stat) $e^+e^-\mu^+\mu^-$ events leading to the measured ratio of branching fractions $B(Z \rightarrow J/\psi + l^+l^-)/B(Z \rightarrow \mu^+\mu^-\mu^+\mu^-) = 0.67 \pm 0.18(\text{stat}) \pm 0.05(\text{syst})$ [49]. In addition, CMS runs a variegate program of analyses dedicated to direct discovery of New Physics, either model-independent or described by existing supersymmetric (SUSY) or exotic models.

Among other physics goals for Run III, there is an improved precision on Higgs coupling measurements, observation of the $H \to \mu^+\mu^-$ and $H \to Z\gamma$ ultra-rare decays, and progress towards the observation of double-Higgs production [47] that can give us important clues on the Higgs sector.

Chapter 4

Multi Parton Interaction with focus on Triple Parton Scattering

4.1 Parton distribution functions

The first evidence of proton inner structure dates back to the 1960s. Despite the absence of experimental evidence, the idea of more elementary components of the matter had already been discussed by theorists. A few years later surprising results from a series of deep inelastic scattering (DIS) experiments, performed from 1967 through 1973 by a collaboration of scientists from the Massachusetts Institute of Technology (MIT) and the Stanford Linear accelerator Center (SLAC), began to give direct evidence for the existence of quarks as real, physical entities [50].

In DIS it is common to use the word scattering to refer to leptons deflection and the measurement of the deflection angle gives information about the nature of the process. On the other hand, the term inelastic means that the target can partially absorb the kinetic energy of the probe.

Within DIS processes one can determine the scattering cross section for a specific target, which structure can be expressed in terms of two structure functions $W_1(Q^2, \nu)$ and $W_2(Q^2, \nu)$. The former describes the interaction between the electron and the nucleon magnetic moments, the latter describes the interaction between the charges and is sensitive to the charge distribution. Both depend on Q^2 which is the four-momentum transfer, meanwhile the variable ν is defined as the energy transferred to the target in the laboratory frame. In the kinematic conditions of the experiments that one shall refer to, W_1 is negligible, thereby the cross section can be expressed in the form:

$$\frac{d\sigma}{d\Omega dE'} = \left(\frac{d\sigma}{d\Omega}\right)_{\text{point}} W_2(Q^2, \nu).$$

The aim of these experiments is to determine the function $W_2(Q^2, \nu)$, which experimentally translates in the measurement of the deep inelastic differential cross section at several values of Q^2 and ν [51].

The main results of the measurements made at SLAC showed a surprising behaviour of $W_2(Q^2, \nu)$ as a function of Q^2. It seemed that, in the deep inelastic region, the function W_2 slightly varies with Q^2 and is independent of the hadronic mass W. It follows that the nucleon contains point-like objects, to which R. Feynman [52] referred as *partons*, later identified as *quarks*. In the model proposed by Feynman, scaling arose naturally because high-energy electrons rebounded elastically from charged, pointlike partons; he recognized that the universal function $F_2(x, Q^2) = \nu W_2(Q^2, \nu)$ was the momentum distribution of the partons, weighted by the squares of their charges, when plotted versus a variable $x = Q^2/2M\nu$, where M is the mass of the proton. Note that x is actually the inverse of Bjorken's variable; it represents the fraction of the proton momentum carried by the struck parton when viewed in what Feynman called the *infinite momentum frame*, essentially the frame in which the electron is at rest and the proton is speeding toward it [50].

The possibility to explore higher energy regions lead to the observation that the valence quarks were not the only constituents of nucleons. Indeed, high-resolution probes, principally electron and neutrino beams, have shown that nucleons contain the following components:

- the three quarks called *valence quarks*, which suggest the nature of the observed hadron;
- the gluons which are the quanta of the colour field;
- the quark and the antiquark of the *sea*.

In the intense colour field, several processes take place continually: gluons materialize in pairs of quarks and antiquarks which soon annihilate, two gluons fuse into one and so on. As one can imagine, the probability of finding a specific quark rather than another depends on the mass. Thus the probability of finding a quark-antiquark pair of a certain flavour decreases for increasing masses.

It is common to define $f(x)$ as the distribution of the momentum fraction for a quark of a flavour *f*, consequently $f(x)dx$ assumes the meaning of the probability that a quark carries a momentum fraction between x and $x + dx$. Analogously $\bar{f}$ is used for the antiquark and g for the gluons. These functions play a key role in the theory and are called *parton distribution functions (PDF)*.

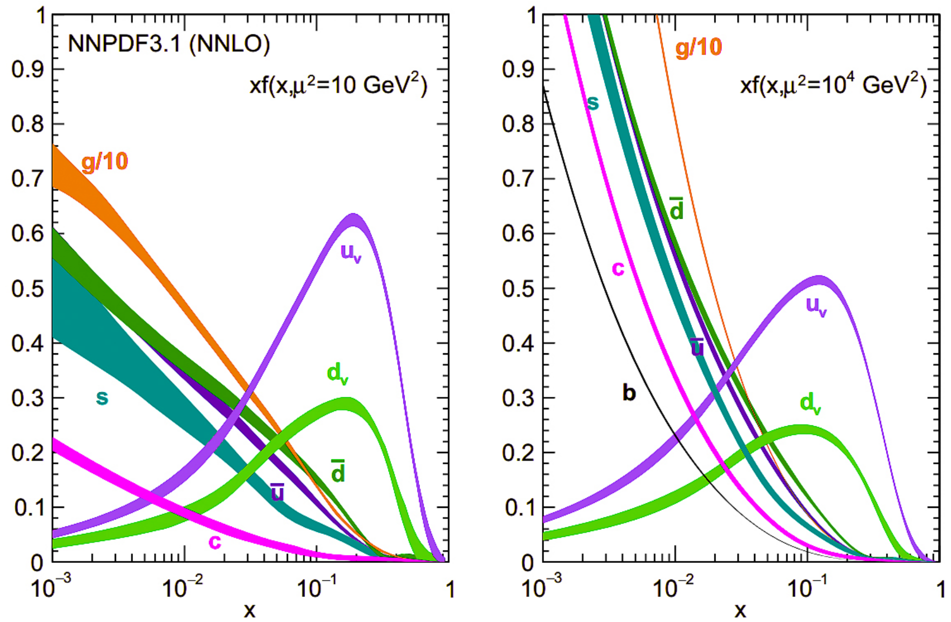

Figure 4.1: In figure it is shown an example of parton distribution function that is the NNPDF3.1 NNLO PDFs, evaluated at $\mu^2 = 10$ GeV^2 (left) and $\mu^2 = 104$ GeV^2 (right) [53].

An example of PDFs can be seen in figure 4.1: it is crucial to observe how the slope of the distributions changes at different energies, especially for the quark sea and the gluons. The distribution functions are obtained experimentally from the measurement of the differential cross section of electrons, neutrinos and antineutrinos scatterings. Using electroweak probes is although not sufficient. For instance, neglecting the contribution of the charm quarks and taking into account all the dependencies between the PDF of the nucleons quarks, only five distributions remain to study.

Integrating over the measured distribution functions one obtains:

$$\int_0^1 x[u(x) + d(x) + \bar{u}(x) + \bar{d}(x) + s(x) + \bar{s}(x)]dx \approx 0.50$$

All the quarks and antiquarks do not carry all the momentum of the nucleon [51]. This suggests that half of the momentum is carried by particles that cannot interact weakly or electromagnetically: these are the gluons.

Another hint of the distribution of partons inside the nucleons comes from the violation of Bjorken's scaling law. It was believed, and in a first moment also verified from different experiments, such as ZEUS [54] and H1 [55] carried out at the electron-proton collider HERA [56], that the structure function F_2 was independent of Q^2 [51]. As matter of fact, the data appeared to *scale*: they fell along a single curve $F_2 = \nu W_2$ that is a function of only the ratio ν/Q^2, and not ν and Q^2 independently, even though the cross sections had been measured at several different energies. Nevertheless, for small x values the scaling law is falsified: by increasing the resolution power it is possible to observe how F_2 is no longer independent of Q^2 (figure 4.2). This may imply the model used might be excessively naive.

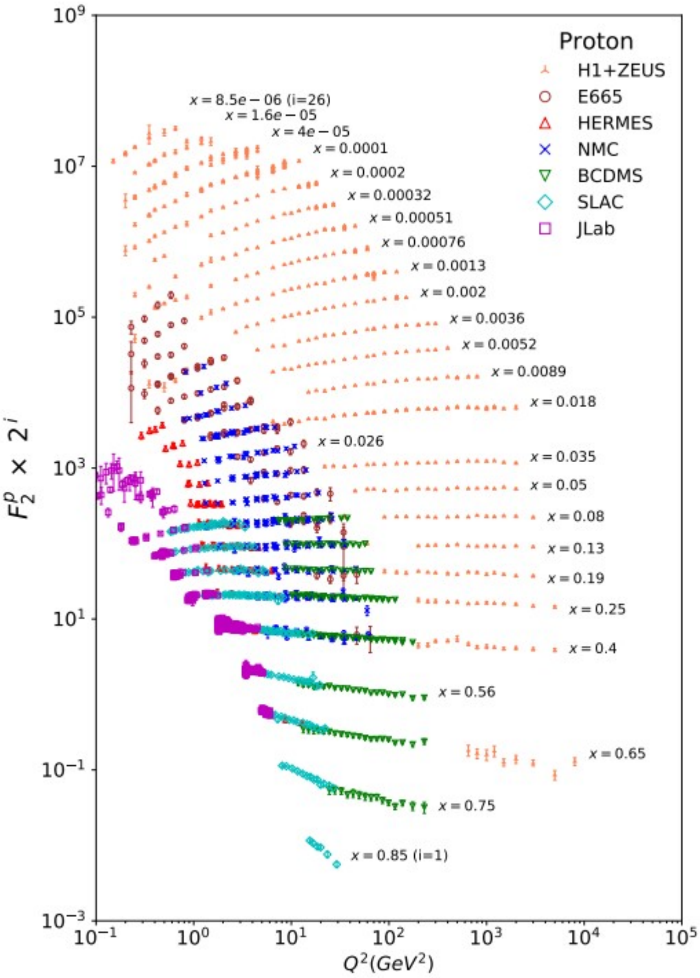

Figure 4.2: Bjorken Scaling: independence of structure functions vs Q^2 in proton (PDG,2019).

Where the naive parton model fails the Dokshitzer-Gribov-Lipatov-Altarelli-Parisi or DGLAP equations seems to be in perfect agreement with the data, finally explaining the phenomenon of the scaling violation of the proton structure function F_2 [51]. They are differential equations that describe to leading-logarithmic accuracy the change in the parton distribution functions when changing Q_2. DGLAP equations are an important example of evolution equations in quantum field theory. If one increases Q^2, enhancing the resolving power, indeed from Heisenberg's uncertainty relation, it is clear that $r_\perp^2 \approx 1/Q^2$ in the transverse plane, hence Q^2 can be understood as the resolution with which the constituents of nucleons are probed. The quarks emit and absorb gluons at lower x; if the initial quark has a momentum x, emitting a gluon of $x - x'$ momentum, its final momentum becomes x'. If the resolving power is not sufficient it is not possible to resolve the quark and the emitted gluon as two separated entities, contrariwise, if Q^2 is large enough, one resolves the two objects and measure the fraction to be x' (figure 4.3).

Figure 4.3: Partons with smaller and larger resolving power.

The interest in studying parton distribution functions and their energy evolution is high: for instance, α_s can be determined from the evolution of the form function as a function of Q^2. Moreover, improving our knowledge on how the momentum is distributed among the partons is crucial in the determination of cross section. Increasing the power of prediction of the cross section can be useful to forecast the number of expected events of a certain type, which leads to improved knowledge of the background events. The ability to discriminate background events from the ones of physics interest is essential in the search for New Physics (NP) or where the processes under investigation are extremely rare.

4.2 Multi parton interaction

A direct consequence of the hadron composite nature is that in a generic hadron-hadron collision is inevitable that multi parton interactions may occur (figure 4.4). In literature, these events are called MPI for short.

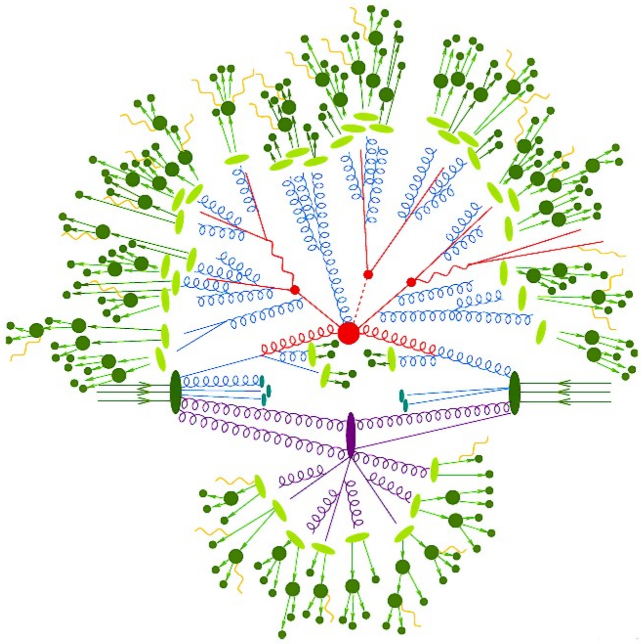

Figure 4.4: Graphic illustration of multi parton interaction in a proton-proton collision.

While in an electron-positron collision the initial state is well defined due to the elementary nature of the colliding particles, this does not happen in a hadronic collider. That is because it is not possible to forecast, in principle, how many and which parton-parton interactions will simultaneously take place in a hadronic process. Multi parton interactions stand out for the energy involved in hard and soft processes: it is rare to have two or more separate hard processes. However, they are gaining relevance due to their higher probability to occur, since in time the energy involved in colliders has been increased.

The hard nature of the scattering ensures that this process is much more approachable from a theoretical front, with the potential to develop and prove factorization formulae that have already extensively been used for single parton scattering interaction. In the modelling of the soft theory of MPI, the knowledge acquired in the hard sector can be spent, indeed, and soft models can be seen as an extension of the ones used for harder processes [57].

4.2.1 Double parton scattering

DPS is the most trivial extension to multi parton interaction and by definition, it occurs if in the same proton-proton collision two partons in each proton initiate two separate hard scattering processes [57]. More than thirty years ago, the AFS and the UA2 collaborations observed double parton scattering (DPS) processes for the first time. After these pioneering works, a series of measurements was performed at the Tevatron collider and the LHC [58] [59].

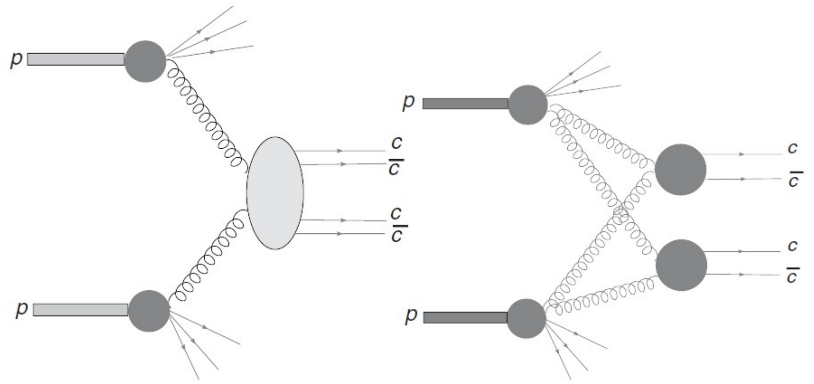

Figure 4.5: Example of a SPS process (left) and a DPS processes (right).

At LHC energy, the quark-antiquark annihilations play a marginal role. Consequently, all the efforts can focus on gluon-gluon interactions. Limiting the possible initial processes is, obviously, a simplification, although, all the possible correlations between partons due to, e.g., QCD or spin interaction, drastically complicate the theory behind the processes. In order to simplify the theory and obtain a model that can be used to compare predictions to data, one can rely on the so-called *factorized ansatz*. The generic DPS cross section reads:

$$\begin{aligned} \sigma^{DPS}_{pp\longrightarrow q\bar{q}q\bar{q}} = \frac{m}{2!} \int & \Gamma^{gg}_{p}(x_1, x_2; \vec{b_1}, \vec{b_2}; \mu_1^2, \mu_2^2) \\ & \times \hat{\sigma}^{gg}_{q\bar{q}}(x_1, x_1', \mu_1^2) \hat{\sigma}^{gg}_{q\bar{q}}(x_2, x_2', \mu_2^2) \\ & \times \Gamma^{gg}_{p}(x_1', x_2'; \vec{b_1} - \vec{b}, \vec{b_2} - \vec{b}; \mu_1^2, \mu_2^2) \\ & \times dx_1 dx_2 dx_1' dx_2' d^2b_1 d^2b_2 d^2b, \end{aligned} \tag{4.1}$$

where $\hat{\sigma}^{gg}_{q\bar{q}}(x_i, x_i', \mu_i^2)$ are the partonic cross sections for $gg \to q\bar{q}$ mechanism, x_i, x_i' are the longitudinal momentum fractions, μ_i are the renormalization/factorization scales and $m/2!$ is the combinatorial factor. The above DPS hadronic cross section is expressed in terms of the so-called double-gluon distribution functions $\Gamma^{gg}_{p}(x_1', x_2'; \vec{b_1}, \vec{b_2}; \mu_1^2, \mu_2^2)$.

Multi-PDFs should depend on all the possible correlations between partons, such as colour and flavour interactions as well as spatial and kinetical correlations. Although MPIs are under intense study, there is not a well defined theoretical model capable of describing the phenomenology. It is therefore suggested to use a simplified model, thus in practice, one uses the *factorized ansatz*. In this optic, the double gluon distribution is simplified: longitudinal and transverse degrees of freedom can be regarded as independent and other correlations between partons can be neglected; thus one can assume:

$$\begin{aligned}\Gamma_p^{gg}(x_1, x_2; \vec{b_1}, \vec{b_2}; \mu_1^2, \mu_2^2,) =& D_p^{gg}(x_1, x_2, \mu_1^2, \mu_2^2) \\ & \times F(\vec{b}_1) F(\vec{b}_2),\end{aligned} \tag{4.2}$$

where $D_p^{gg}(x_1, x_2 \mu_1^2, \mu_2^2)$, which is the double PDF in the transverse plane, can be further simplified in:

$$D_p^{gg}(x_1, x_2, \mu_1^2, \mu_2^2) = g(x_1; \mu_1^2) g(x_2; \mu_2^2)). \tag{4.3}$$

After the simplifications, all the possible interactions are neglected, therefore a DPS process can be seen as two simultaneous SPS (see figure 4.5); in view of this, one can write the so-called *pocket formula* [60]:

$$\sigma_{DPS}^{pp \to \psi_1 \psi_2} = \left(\frac{m}{2!} \right) \frac{\sigma_{SPS}^{pp \to \psi_1} \cdot \sigma_{SPS}^{pp \to \psi_2}}{\sigma_{\text{eff},DPS}}, \tag{4.4}$$

where m is a combinatorial factor that can assume value 1 or 2 depending on the multiplicity of the final state, $\sigma_{SPS}^{pp \to X}$ is the cross section for a specific final state and the σ_{eff}'s role is to summarize all the unknown effects. The $\sigma_{\text{eff},DPS}$ is an effective cross section that, in a purely geometric approach, can be determined from the p-p transverse overlap. Initially it was assumed that its value could have been constant at different energies of center of mass and independent form the specific process taken into account, but now, in light of some recent observations it seems that there might be some correlations between the σ_{eff} value and the energy and/or the process studied. This will be discussed in more detail in the next paragraph.

A smaller value of $\sigma_{\text{eff},DPS}$, which is proportional to the average (squared) transverse separation of the partons participating in the two hard scatterings, implies larger DPS yields [61]. The previous formula (4.4) assumes that the two sub-processes are not correlated and do not interfere: to date there are not enough precision studies able to confirm or reject such approximation.

The effective cross section can be expressed as:

$$\sigma_{\text{eff}} = \left[\int d^2b \; (T(\vec{b}))^2 \right]^{-1}, \tag{4.5}$$

where $T(\vec{b})$ is the overlap function and it is defined as follows:

$$T(\vec{b}) = \int f(\vec{b_1}) f(\vec{b_1} - \vec{b}) d^2 b_1, \tag{4.6}$$

where $\vec{b}$ is the impact parameter.

To solve the pocket formula, calculation of the SPS cross section is needed: a common approach is based on the k_T-*factorization*. The framework of the k_T-*factorization* approach is often used with success in describing inclusive spectra of D or B mesons as well as for theoretical predictions for so-called nonphotonic leptons, products of semileptonic decays of charm and bottom mesons [62]. In this optic the SPS cross section reads:

$$\begin{aligned} \frac{d\sigma^{SPS}_{pp\to q\bar{q}}}{dy_1 dy_2 d^2p_{1,t} d^2p_{2,t}} =& \frac{1}{16\pi^2 (x_1 x_2 S)^2} \int \frac{d^2 k_{1t}}{\pi} \frac{d^2 k_{2t}}{\pi} \overline{|\mathcal{M}_{g^* g^* \to q\bar{q}}|^2} \\ & \times \delta^2(\vec{k_{1t}} + \vec{k_{2t}} - \vec{p_{1t}} - \vec{p_{2t}}) \mathcal{F}_g(x_1, k_{1t}^2, \mu^2) \mathcal{F}_g(x_2, k_{2t}^2, \mu^2), \end{aligned} \tag{4.7}$$

where $\mathcal{M}_{g^* g^* \to q\bar{q}}$ is the matrix element for the off-shell production of a pair of quark-antiquark from g-g interaction; it must be calculated including the transverse momenta of the initial gluons. $\mathcal{F}_g(x_i, k_{it}^2, \mu^2)$ are the unintegrated gluons PDF, notable is their dependence from k_T. At this point, it is essential to clarify that multi parton interactions can take place in a generic hadronic collision and not just only in a proton-proton one. In order to enhance the possibility to observe DPS events, one should find out which are the golden channels for the aim of their research. In 2014 A. van Hameren and R. Maciuła [63] suggested charmed mesons, both hidden or opened, to be one of the best final states for DPS investigation in the small-x region. As a preliminary result, it is shown how the $q\bar{q} \to c\bar{c}\, c\bar{c}$ contribution in rapidity and transverse momentum is negligible with respect to $gg \to c\bar{c}\, c\bar{c}$ at $\sqrt{s} = 7$ TeV.

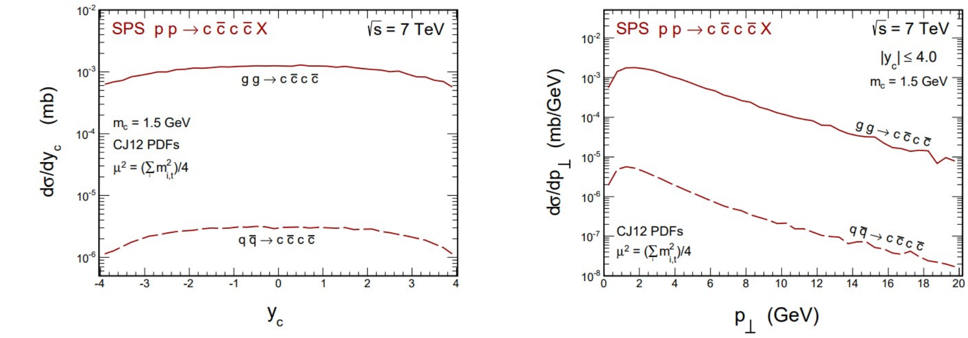

Figure 4.6: Comparison of gluon fusion and quarl-antiquark annihilation distribution with respect to rapidity (left panel) and transverse momentum (right panel) for $c\bar{c}$ $c\bar{c}$ production (van Hameren et Maciuła, 2014).

Likewise for single $c\bar{c}$ production, as it is shown in figure 4.6, the gluon-gluon fusion gives the contributions of almost two-orders of magnitude larger than the quark-antiquark (antiquark-quark) annihilation. The correct prediction of the charmed meson as one of the golden final states for the study of DPS is another remarkable result.

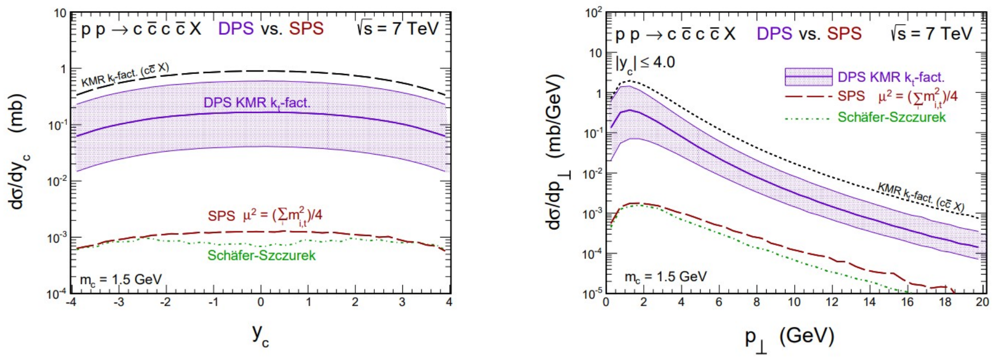

Figure 4.7: Rapidity (left panel) and transverse momentum (right panel) distributions of charm quarks for $c\bar{c}$ $c\bar{c}$ production (van Hameren et Maciuła, 2014).

A first hint of the relevance of DPS processes in the charmed mesons' final states was already present in a 2012 paper by M. Łuszczak, R. Macuiła and A. Szczurek[62]. In figure 4.7 is possible to see how the DPS yields is predicted to overtake the SPS ones.

Thereafter, in 2014 the predictions were compared to data [64].

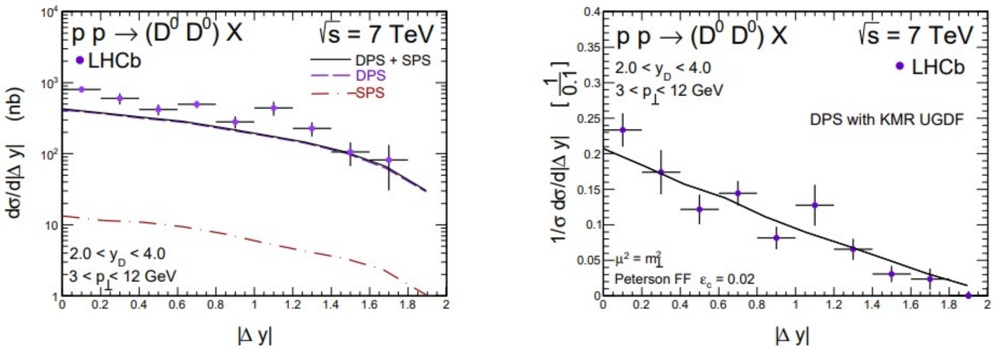

Figure 4.8: Distribution in rapidity difference between two D^0 mesons (left panel). The SPS contribution (dash-dotted line) is compared to the DPS contribution (dashed line). The right panel shows distribution normalized to the total cross section (van Hameren et Maciuła, 2014).

Figure 4.8 represents the comparison between data and theoretical predictions: the shape of the distribution is well reproduced.

4.2.2 State of art for double parton scattering

As just discussed, charmed particles are a valid final state to study DPS. However, since charmed mesons are very soft objects when compared to the energy scale of the LHC, they are an efficient probe only for the small-x region. Nevertheless, to draw a more comprehensive picture of MPIs, it is mandatory to consider different topologies. Harder objects, e.g. same-sign W bosons pairs (ssWW), can offer complementary information on DPS, providing an opportunity to explore higher x-values. The ATLAS, ALICE, CMS, and LHCb Collaborations have reported measurements of DPS in various topologies, such as the aforementioned ssWW, J/ψ production or double charm production. Also, events with W+jets, 4 jets and more recently a Z boson plus a di-jet have been studied [65]. In the following lines same examples of DPS studies are reported.

Double ssWW: the same-sign WW production is considered a golden channel for the DPS study at large x since the two W bosons are produced independently of each other and without any associated jet (with respect to the topology of the SPS production), furthermore leptonic decay is reconstructed in order to ensure a clear identification of the final state. The measured cross section for production of same sign W bosons decaying leptonically is $80.7 \pm 11.2(\text{stat})^{+9.5}_{-8.6}$ (syst) ± 12.1 (model) fb, whereas the measured fiducial cross section is 6.28 $\pm$ 0.81 (stat) $\pm$ 0.69 (syst) $\pm$ 0.37 (model) fb. The observed significance of the signal is 6.2 standard deviations above the background-only hypothesis [66] [67].

4-jets: in recent times a study of the inclusive production of four-jet events at low transverse momentum has been presented based on data from proton-proton collisions collected with the CMS detector at a centre-of-mass energy of 13 TeV. Differential cross sections are measured as functions of the jet transverse momentum, jet pseudorapidity, and several other observables that describe the angular correlations between the jets. Since the interplay between angular correlations caused by parton shower and double-parton scattering contributions is shown to be important, this topology might be a good probe for DPSs. The effective double-parton scattering cross section has been calculated and discussed given previous measurements and of its dependence on the models used to describe the single-parton scattering background [1]. Other important observations on kinetical variables and useful cuts suggested for the final state with a 4-jets topology can be found in [58].

W boson plus a J/ψ: recently ATLAS data have been re-analysed in a new light: it has been deepened the associated production of a prompt $J//\psi$ and a W boson in p-p collisions. Performing next-to-leading (NLO) calculation of the SPS cross section in the Colour-Evaporation Model (CEM) it has been possible to claim a 3σ deviation between SPS theory and ATLAS data, which has been interpreted as a strong indication for DPSs. The extracted σ_{eff} is $\sigma_{\text{eff}} = (6.1^{+3.3}_{-1.9}{}_{\text{exp}}{}^{+0.1}_{-0.3}{}_{\text{theo}})$ mb which is consistent with the previous prediction always made by the ATLAS Collaboration [68].

Z boson plus a di-jet: double parton scattering is investigated using events with a Z boson and jets, where the Z boson is reconstructed using only the dimuon channel. The measurements are performed with proton-proton collision data recorded by the CMS experiment at the LHC at $\sqrt{s} = 13$ TeV, corresponding to an integrated luminosity of 35.9 fb^{-1} collected in the year 2016. This is the first measurement performed to explore observables sensitive to the presence of multi-parton interaction (MPI) using the Z+jets process at 13 TeV. Within the fiducial region, the production cross sections of Z+$\geq$ 1 jet and Z+ $\geq$ 2 jet events are measured to be $158.5 \pm 0.3(\text{stat}) \pm 7.0(\text{syst}) \pm 1.2(\text{theo}) \pm 4.0(\text{lumi})$ pb and $44.8 \pm 0.4(\text{stat}) \pm 3.7(\text{syst}) \pm 0.5(\text{theo}) \pm 1.1(\text{lumi})$ pb, respectively [65].

The ones detailed above were just a few examples of DPS studies and their most recent achievements. At the time we are far from having a sufficient experimental sensitivity and a complete theoretical overview for MPIs: the former limits the capability to esteem the strength of the initial assumptions, and the latter limits the prediction and description power of the observations.

Another limiting aspect inherited by the theory is the impossibility to determine *a priori* the σ_{eff}. Current methods used for σ_{eff} extraction rely on fits to DPS-sensitive observables performed with two different templates, one for the background contribution and one for the signal. This method is the so-called *Template method*. The principal difficulty of this procedure is to define an appropriate background template consistently with different Monte Carlo event generators. This feature consequently brings larger uncertainties due to model dependence and some ambiguity in the σ_{eff} extraction.

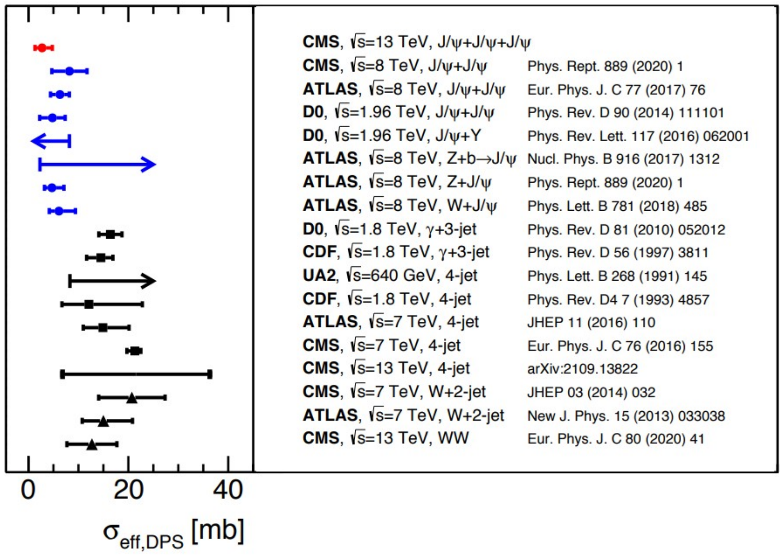

Figure 4.9: Comparison of the σ_{eff} parameter extracted here (upper red circle) to those derived in midrapidity measurements of double-quarkonium and EW boson plus quarkonium production (blue circles), as well as in final states with jets, $\gamma+$ jets, W+jets, and same-sign W bosons (black squares and triangles). The arrows indicate lower limits at 95 confidence level [61].

One of the most severe issue concerning the σ_{eff} in the DPS case is its value: the effective cross sections obtained from quarkonium measurements give a value of $\sigma_{\text{eff},DPS} \approx 3-10$ mb compared to the $\sigma_{\text{eff},DPS} \approx 10-20$ mb derived from harder or heavier final states [61]. The dependence of the $\sigma_{\text{eff},DPS}$ from the process might be linked to different parton transverse profiles and/or correlations present [61]. At midrapidity, ($|\eta| < 2.5$), quarkonia are produced mostly in gluon-gluon scatterings carrying a fraction $x \approx 5 \times 10^{-4}$ of the proton momentum, whereas mostly quarks around $x \approx 1 \times 10^{-2}$ intervene in the production of electroweak (EW) bosons. The

LHCb measurements of double-quarkonia and quarkonia-plus charm at forwarding rapidities ($\eta \approx 2-4.5$), processes originate in parton scatterings with asymmetric fractional momenta $x_1 \approx 10^{-4}$ and $x_2 \approx 10^{-2}$, leading to values of $\sigma_{\text{eff},DPS} \approx 15$ mb. Such value is larger than those measured at midrapidity for similar final states, which suggests the dependence of the effective DPS cross section on the relevant parton species and x fractions probed [61]. What has just been said can be appreciated in fig 4.9 that reports the σ_{eff} measured by different analysis and experiments so far.

4.3 Triple parton scattering

Triple parton scattering can be regarded as a further step from DPS. As before mentioned, as the energy of the colliding protons increases, the collisions probe shorter and shorter distances within the proton, and the density of gluons and sea quarks grows rapidly. Thus, at higher energies, more simultaneous parton interactions are expected. This is the reason why exploring always higher energy frontiers is essential to study *n-parton interactions*.

TPS formalism [69] is the same of the DPS one. The generic cross section reads:

$$\begin{aligned}\sigma^{TPS}_{pp\longrightarrow q\bar{q}q\bar{q}q\bar{q}} = \frac{m}{3!}\int & \Gamma^{ggg}_p(x_1,x_2,x_3;\vec{b_1},\vec{b_2},\vec{b_3};\mu_1^2,\mu_2^2,\mu_3^2) \\ & \times\hat{\sigma}^{gg}_{q\bar{q}}(x_1,x_1',\mu_1^2)\hat{\sigma}^{gg}_{q\bar{q}}(x_2,x_2',\mu_2^2)\hat{\sigma}^{gg}_{q\bar{q}}(x_3,x_3',\mu_3^2) \\ & \times\Gamma^{ggg}_p(x_1',x_2',x_3';\vec{b_1}-\vec{b},\vec{b_2}-\vec{b},\vec{b_3}-\vec{b};\mu_1^2,\mu_2^2,\mu_3^2) \\ & \times dx_1dx_2dx_3dx_1'dx_2'dx_3'd^2b_1d^2b_2d^2b_3d^2b,\end{aligned} \tag{4.8}$$

where $\hat{\sigma}^{gg}_{q\bar{q}}(x_i,x_i',\mu_i^2)$ are the partonic cross sections for $gg \rightarrow q\bar{q}$ mechanism, x_i, x_i' are the longitudinal momentum fractions, μ_i are the renormalization/factorization scales and $m/3!$ is the combinatorial factor. The above TPS hadronic cross section is expressed in terms of the so-called triple-gluon distribution functions $\Gamma^{ggg}_p(x_1',x_2',x_3';\vec{b_1},\vec{b_2},\vec{b_3};\mu_1^2,\mu_2^2,\mu_3^2)$.

Triple parton distribution, triple PDFs, should depend on all the possible correlations between partons, however, likely to the DPS case, it is suggested to use a simplified model, thus in practice, one uses the *factorized ansatz*. In this optic, the triple gluon distribution is simplified: longitudinal and transverse degrees of freedom can be regarded as independent and other correlations between partons can be neglected; thus one can assume:

$$\Gamma_p^{ggg}(x_1, x_2, x_3; \vec{b_1}, \vec{b_2}, \vec{b_3}; \mu_1^2, \mu_2^2, \mu_3^2) = D_p^{ggg}(x_1, x_2, x_3, \mu_1^2, \mu_2^2, \mu_3^2) \times F(\vec{b}_1)F(\vec{b}_2)F(\vec{b}_3), \tag{4.9}$$

where $D_p^{ggg}(x_1, x_2, x_3\mu_1^2, \mu_2^2, \mu_3^2)$, which is the triple PDF in the transverse plane, can be further simplified in:

$$D_p^{ggg}(x_1, x_2, x_3, \mu_1^2, \mu_2^2, \mu_3^2) = g(x_1; \mu_1^2)g(x_2; \mu_2^2)g(x_3; \mu_3^2). \tag{4.10}$$

According to these approximations the formula for inclusive TPS cross section, similarly to the DPS case (4.4), can be simplified to the pocket form:

$$\sigma_{TPS}^{pp\to\psi_1\psi_2\psi_3} = \left(\frac{m}{3!}\right)\frac{\sigma_{SPS}^{pp\to\psi_1} \cdot \sigma_{SPS}^{pp\to\psi_2} \cdot \sigma_{SPS}^{pp\to\psi_3}}{\sigma_{\text{eff},TPS}^2}. \tag{4.11}$$

where $m = 1, 3$ or 6, depending on whether all three, two or none of the ψ_i states are identical [61] [70].

As mentioned, σ_{eff} in the DPS case is obtained from experiments; this strategy, because of the absence of experimental data, cannot be applicated to the TPS case yet. From simple geometric considerations, $\sigma_{\text{eff},TPS}$ is closely connected to the effective cross section $\sigma_{\text{eff},DPS}$ already measured in DPS. From the existing measurements of $\sigma_{\text{eff},DPS}$ and realistic proton profiles, it is possible to derive the numerical value of $\sigma_{\text{eff},TPS}$ which proves very robust whichever is the choice of the underlying transverse parton density [71].

In an article published in 2016 by D. d'Enterria and A. M. Snigirev [71] different ways were proposed to numerically esteem $\sigma_{\text{eff},TPS}$. Similarly to $\sigma_{\text{eff},DPS}$ (4.5), $\sigma_{\text{eff},TPS}$ is defined:

$$\sigma_{\text{eff},TPS} = \left[\int d^2b \; (T(\vec{b}))^3\right]^{-1}. \tag{4.12}$$

To estimate the value of $\sigma_{\text{eff},TPS}$ one can first consider a simplistic class of analytical models for the overlap function of a given hadronic AA collision:

$$T_{AA}(\vec{b}) = \begin{cases} \frac{A^2(n+1)}{4\pi R_A^2}[1 - (b/2R_A)^2]^n & b < 2R_A \\ 0 & b > 2R_A \end{cases} \tag{4.13}$$

normalized to $T = \int d^2b \; T_{AA}(\vec{b}) = A^2$, where exponents n = 0,1...∞ give respectively a flat, hard-sphere-like, and Gaussian-like distribution in the interval $[0, 2R_A]$; R_A is the radius.

Using (4.13) in (4.12) one gets:

$$\sigma^2_{\text{eff},TPS} = \left[\int d^2b \; (T(\vec{b}))^3 \right]^{-1} = \frac{(4\pi R_A^2)^2(3n+1)}{A^6(n+1)^3}. \tag{4.14}$$

Once this formula is specified to the proton case, thus $A = 1$ and $R = r_p$, where r_p is its characteristic transverse "radius", it reads:

$$\sigma^2_{\text{eff},TPS} = \frac{(4\pi r_p^2)^2(3n+1)}{(n+1)^3}. \tag{4.15}$$

For the DPS case, using (4.13), one gets:

$$\sigma^2_{\text{eff},DPS} = \left[\int d^2b \; (T(\vec{b}))^2 \right]^{-1} = \frac{4\pi R_A^2(2n+1)}{A^4(n+1)^2} \tag{4.16}$$

It is advantageous to express (4.14) in terms of (4.16) since $\sigma_{\text{eff},DPS}$ can be experimentally determined; the equation (4.15) now reads:

$$\sigma^2_{\text{eff},TPS} = \frac{(3n+1)(n+1)}{(2n+1)^2}\sigma^2_{\text{eff},DPS}. \tag{4.17}$$

The exponent n varies from 0 to ∞, thus the factor $k = \frac{(3n+1)(n+1)}{(2n+1)^2}$ in (4.17) varies from 1 to 0.87, i.e. the effective TPS cross section is waited to be similar to the DPS one.

Another approach suggested in the same paper is based on the current Monte Carlo (MC) techniques used to simulate σ effective: in the PYTHIA genrator [5], the p-p overlap function is parametrized with:

$$T(\vec{b}) = \frac{m}{2\pi r_p^2 \Gamma(2/m)} \exp[-(b/r_p)^m] \tag{4.18}$$

normalized to one, where $\Gamma(2/m)$ is the gamma function. The exponent m depends on the MC *tune* obtained from fits to the measured p-p *underlying events* and various DPS cross sections. Analogously to the previous case one can use (4.18) to calculate (4.5) and (4.12), then using (4.5) in (4.12) one gets:

$$\sigma_{\text{eff},TPS} = (3/4)^{1/m}\sigma_{\text{eff},DPS}. \tag{4.19}$$

The latest proposal is based on phenomenological observations: the description of the proton profile is given by the dipole fit of the two gluon form factor in the momentum representation

$$F_{2g}(q) = 1/(q^2/m_g^2 + 1)^2 \tag{4.20}$$

where the gluon mass m_g parameter characterizes its transverse momentum q distribution, and the transverse density is obtained from its Fourier-transform:

$$f(b) = \int e^{-ib\cdot q} F_{2g}(q) \frac{d^2 q}{(2\pi)^2} \tag{4.21}$$

Numerically integrating the latter and combining it with (4.20), one obtain $\sigma_{\text{eff},TPS} = 0.83 \times \sigma_{\text{eff},TPS}$ which is quite close to the value obtained for the Gaussian p-p overlap function. Finally, the authors agree that the effective TPS cross section should remain similar to the DPS one, whichever is the path taken.

Indeed, the average and standard deviation of all typical parton transverse profiles considered here, yields $\sigma_{\text{eff},TPS} = k \times \sigma_{\text{eff},DPS}$, with $k = 0.82 \pm 0.11$, i.e., for the typical $\sigma_{\text{eff},TPS} = 15 \pm 5$ mb values extracted from a wide range of DPS measurements at Tevatron and LHC, one finally obtain $\sigma_{\text{eff},TPS} = 12.5 \pm 4.5$ mb.

There are not any other proposals for the effective TPS cross section in the literature yet.

4.3.1 State of art for triple parton scattering

Various final states have been studied to understand if the TPS cross section is relevant to the energy achieved nowadays.

To answer this question, R. Maciuła and A. Szczurek, in a paper published in 2017 [69], suggested the LHCb collaboration to measure the final states for three D^0 mesons or three $\bar{D}^0$ antimesons. Using the factorized ansatz and the k_T-*factorization* quite large cross sections, of the order of millibarns, for the triple parton scattering mechanism are foreseen. It seems clear how TPS cross section increases for increasing energies, indeed, by comparing the number of predicted events linked to triple parton scattering at $\sqrt{s} = 7$ TeV and $\sqrt{s} = 13$ TeV goes from a hundred of events to a few thousand.

$\sqrt{s}$	Integrated Luminosity	DPS(D^0D^0)	TPS($D^0D^0D^0$)
7 TeV	355 pb^{-1}	0.43×10^6	51
	1106 pb^{-1}	2.34×10^6	159
13 TeV	1665 pb^{-1}	7.70×10^6	1789
	5000 pb^{-1}	23.11×10^6	5374

Table 4.1: Number of predicted events for different values of the feasible integrated luminosity in the LHCb experiment for the central predictions of cross sections. The branching fractions for $D^0 \rightarrow K^-\pi^+$ ($\bar{D}^0 \rightarrow K^+\pi^-$) are included here [69].

D. d'Enterria and A. M. Snigirev have forcasted, as well, the positive trend for TPS cross sections. In the already mentioned 2016 paper, they released a prediction of the triple cross sections for final states with charm quarks or bottom quarks.

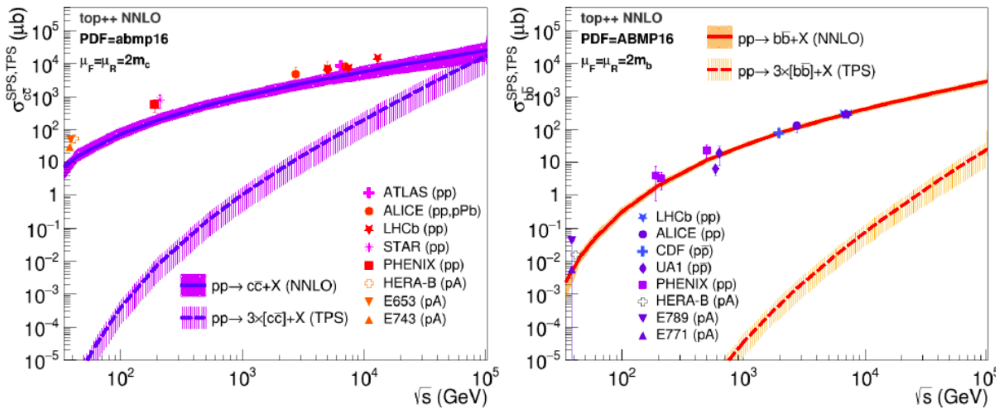

Figure 4.10: Total charm (left) and bottom (right) cross sections in pp collisions as a function of c.m. energy, in single-parton (solidline) and triple-parton (dashed line) parton scatterings. Bands around curves indicate scale, PDF (and $\sigma_{\text{eff},TPS}$, in the case of σ_{TPS}) uncertainties added in quadrature (D'enterria and Snigirev 2016).

The results show how bringing the energy up to $\sqrt{s} = 100$ TeV the charmed channel should be prefered to the bottom one, since, in the former case, the TPS cross section grows more rapidly (figure 4.10). Indeed, meanwhile, at $\sqrt{s} = 100$ TeV, the TPS cross section with bottom quarks remains of two orders smaller of the SPS cross section, for the charmed final states both SPS and TPS cross sections are of the order of mb [71].

Final state	$\sqrt{s} = 14TeV$	$\sqrt{s} = 100TeV$
$\sigma(c\bar{c} + X)$	$7.1 \pm 3.5_{sc} \pm 0.3_{pdf}$	$25.0 \pm 16.0_{sc} \pm 1.3_{pdf}$
$\sigma(c\bar{c}c\bar{c}c\bar{c} + X)$	$0.39 \pm 0.28_{tot}$	$16.7 \pm 11.8_{tot}$
$\sigma(b\bar{b} + X)$	$0.56 \pm 0.09_{sc} \pm 0.01_{pdf}$	$2.8 \pm 0.6_{sc} \pm 0.1_{pdf}$
$\sigma(b\bar{b}b\bar{b}b\bar{b} + X)$	$(0.19 \pm 0.12_{tot})^{-3}$	$(24 \pm 17_{tot})10^{-3}$

Table 4.2: Total charm and bottom SPS (NNLO) and predicted TPS cross sections (in mb) in p-p at LHC and FCC with scales, PDF, and total (quadratic, including $\sigma_{\text{eff},TPS}$) uncertainties.

The TPS studies mentioned above are still waiting to be experimentally proved, since up to date there are no direct measurement for the TPS yields. To this day, indeed, the only experimental research of triple parton scattering in a p-p collision has been conducted by the CMS collaboration at LHC.

In November 2021, the CMS collaboration published experimental results for TPS processes in p-p collisions for the first time ever [61]. The final states explored contain three J/ψ; both prompt and non-prompt productions are taken into account. In the former case the J/ψ are directly produced by the interaction between partons, meanwhile in the latter case they are produced in B mesons decays. The theoretical study is based on the nonrelativistic quantum chromodynamics (NRQCD) approach at leading-order (LO). Since here SPS contributions are negligible, it is believed that the final state with tree J/ψ is one of the gold channels for the study of TPS also because the three J/ψ are reconstructed in their $\mu^+\mu^-$ final state and, as already mentioned, muon reconstruction is one of the best feature of the CMS detector. In addition, $pp \to J/\psi J/\psi J/\psi + X$ processes can also be used to improve our knowledge on $\sigma_{\text{eff},DPS}$, thereby shedding new light on the underlying dynamics of hard NPS.

They observed a $pp \to J/\psi J/\psi J/\psi + X$ with a significance above five standard deviations in final states with three opposite charge $\mu\mu$ pairs. The measured inclusive fiducial cross section $\sigma(pp \to J/\psi J/\psi J/\psi + X) = 272^{+141}_{-104}(\text{stat}) \pm 17(\text{syst})$ fb is compared to theoretical expectations for the production of three J/ψ mesons in single- (SPS), double- (DPS), and triple- (TPS) parton scatterings. While the cross sections for three prompt J/ψ production are: $\sigma_{\text{SPS}} < 0.005$ fb, $\sigma_{\text{DPS}} = 8.4$ fb and $\sigma_{\text{TPS}} = 6.1$ fb. The few numbers of events, only six, justify the large uncertain on the measurement. All the final states have been implemented in the HELAC-Onia code [3] [4] and it has been demonstrated that the pure SPS contributions are negligible compared to those from DPS and TPS. The HELAC-Onia code, due to its central role in this thesis, will be largely discussed in the next chapter.

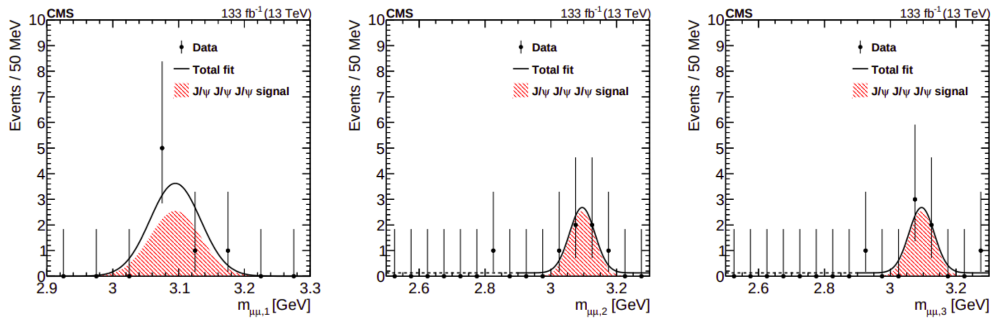

Figure 4.11: Invariant mass distributions for the three $\mu^+\mu^-$ pairs, ordered (left to right) by decreasing pair p_T, in the selected events. The data are represented by the points with the vertical bars showing the (Poisson) statistical uncertainties. The solid (dotted) curve shows the overall fit to the data (in the extended mass range), and the red shaded area the fitted signal yield [61].

The cross section for the inclusive production of three J/ψ is measured via $\sigma(pp \to J/\psi J/\psi J/\psi X) = N^{3J/\psi}_{\text{sign}}/(\epsilon \mathcal{L}_{\text{int}} B^3_{J/\psi\to\mu^+\mu^-})$, where $N^{3J/\psi}_{\text{sign}}$ is the number of signal events, $\mathcal{L}_{\text{int}}$ the total integrated luminosity, $B_{J/\psi\to\mu^+\mu^-}$ the dimuon branching fraction, and $\epsilon = \epsilon_{\text{trig}}\epsilon_{\text{id}}\epsilon_{\text{reco}}$ the total efficiency composed of trigger, identification, and reconstruction components. Finally, the result is compared to the theoretical expectations and under the assumption of factorization for the triple parton scattering cross section. The measured triple J/ψ cross section is consistent with the production via DPS($\approx$ 74%), TPS($\approx$ 20%) and SPS ($\approx$ 6%) processes.

Although the number of events compatible with TPS is limited, the novel approach to study multiple hard-scatterings in p-p collisions, exploited by CMS, lays the foundation for the study of TPS.

Chapter 5

Charmed mesons production as a probe for TPS

In all its fields, naturalness is a central problem of Science: a theory should give a reasonable description and prevision of physical phenomena but should also deal with the problem of fine-tuning. The fine-tune problem concerns all the theories formulated ad hoc to resolve a specific issue, i.e. the SUSY theory and the problem of the normalization of the Higgs boson mass and the hierarchy problem. Some models might seem too artificial to have a true physics valence, however, sometimes, the right intuition can lead to predicting the unpredictable: that was the case of the charm quark. The Glasgow-Illinopulus-Maiani (GIM) mechanism [72] was proposed in 1970 to explain the suppression of the vector-axial neutral current: the innovation of the GIM mechanism was the postulation of the existence of a fourth quark. Four years later, on 11th November, two research groups at the Stanford Linear Accelerator Center (SLAC), led by Richter, and the Brookhaven National Laboratory, led by Ting, announced independently a discovery of a new heavy particle labelled, respectively, ψ [73] and J [74], which finally remained as the J/ψ meson. Both discoveries pointed towards a consistent mass of $m_{J/\psi} \approx 3.1\ GeV$ [75]. The first excited state came only ten days later but it took two more years of research and speculations for the community to agree that the newly observed particle, along with the excited states later appeared, were precisely charm-anticharm bound states ($c\bar{c}$), coined as charmonium, confirming the speculation linked to the GIM mechanism. This discovery was not important just because it confirmed a fourth quark but the quark's physical realm, along with a big push towards the acceptance of the EW and QCD theories [75].

5.1 Study motivations

To date, both open and hidden charmed mesons are central in many studies such as, as largely explained in the previous chapter, the study of DPS and, more recently, TPS processes.

The novel TPS research in a final state with three J/ψ in CMS showed how rare this type of event is: only six events compatible with the triple J/ψ production, via SPS, DPS and/or TPS have been found [61]. The rarety of this peculiar final state might be imputable to the small cross section for the production of charmed quarkonia.

In this thesis, I investigate a novel final state which can work as a probe for TPS: two J/ψ plus a D^* meson. On the one hand, the CMS experiment excels in muons reconstruction, and bear in mind that the J/ψ are principally reconstructed from their decay into muon pairs, on the other hand, the cross section for an open charm meson is larger than the one for a $c\bar{c}$ meson. The idea is then to replace one of the three hidden charm mesons with an open charm one. Unfortunately, the CMS experiment, while excelling at J/ψ reconstruction, does not have the same performance when it comes to the reconstruction of D mesons. This is why, in opposition to the LHCb experiment [18], that has been projected *ad hoc* to study the B flavour physics, CMS, that focus its search program at high energy regime, lacks a particle ID detector and specific triggers to distinguish kaons and pions in the small p_T region, namely the most populated region by these objects. In addition, at small p_T, the higher number of PU tracks makes reconstructing these final states quite challenging.

Although the cross section for a D^0 is larger than the one for the D^*, the D^* meson was preferred over the D^0 because its reconstruction in the CMS framework, thanks to the additional π_{slow} in the decay chain, presents an higher purity. The D^* meson is indeed reconstructed in its most probable decay $D^* \to D^0\pi_{\text{slow}}$. The D^0 meson has a probability to decay hadronically in $D^0 \to K^-\pi^+$ of $(3.88\pm0.05)\%$ and $D^0 \to K^+\pi^-$ of $(1.380 \pm 0.028) \times 10^{-4}\%$; the latter mode is Cabibbo suppressed. Thus the complete chain $D^* \to D^0\pi^+_{\text{slow}} \to K^-\pi^+\pi^+_{\text{slow}}$ is considered here. The reconstruction of charged particles in CMS is limited by the acceptance of the tracker ($|\eta| < 2.4$) and by the decreasing tracking efficiency at low momentum caused by multiple scattering and energy loss. The identification of particle species using specific ionization is restricted to $p < 1.20$ GeV/c for pions and $p < 1.05$ GeV/c for kaons. Pions are measured up to a higher momentum than kaons because of their larger relative abundance. In general low-momentum particles can be identified unambiguously and can therefore be counted; conversely, at high momenta (above about 0.5 GeV/c for pions and kaons and above 1.2 GeV/c for protons) pions and kaons cannot be unambiguously distinguished, thus pion and kaon yields could not be determined for p $>$ 1.20 GeV/c [76]. Indeed, as shown in figure 5.1, over this threshold the energy per unit length deposit ϵ due to kaons and pions overlaps. Also, because of the intrinsic limits of the detector in reconstructing tracks at p_T smaller than 0.5 GeV, the kinematic region where the dE/dx is useful to perform an efficient particle ID is not accessible. In the interval between p_T =0.5-0.9 GeV the detector performances still make unusable the dE/dx information to perform particle ID.

There are all the reasons why a D^* reconstruction, with the association of a charge particle to the D^0 meson, is preferred to the only D^0 identification. Indeed, among all the open charm mesons, the CMS experiment can reconstruct the D^* with higher purity; the price to pay is to have a smaller efficiency.

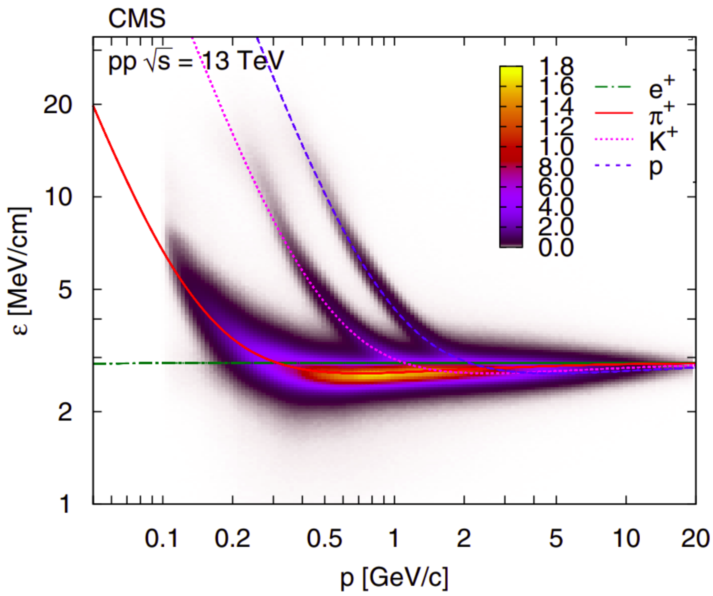

Figure 5.1: Distribution of ϵ as a function of total momentum p, for positively charged reconstructed particles (ϵ is the most probable energy loss rate at a reference path length $l_0 = 450\ \mu m$). The color scale is shown in arbitrary units and is linear. The curves show the expected ϵ for electrons, pions, kaons, and protons.

For all the reasons listed above, a final state with two J/ψ and a D^* may be more promising. My study is focused on the following process:

$$pp \rightarrow J/\psi + J/\psi + D^{*+}, \tag{5.1}$$

where the J/ψ are reconstructed by their decay into muons pairs, while the

D^* mesons are reconstructed by the following decay chain: $D^{*+} \rightarrow D^0\pi^+_{slow} \rightarrow K^-\pi^+\pi^+_{slow}$.

5.2 Sample production

To produce the desired final state, the choice of the software fell on HELAC-Onia [3] [4]. HELAC-Onia is an open-source software that has already been used to produce samples for several Monte Carlo studies: such as the three J/ψ samples used for the analysis [61] already presented in the previous chapter. Since HELAC-Onia has been developed with the aim to exceed PYTHIA [5] performance in quarkonia production, the choice felt natural. The HELAC-Onia software is based on Fortan99 and, to be more user friendly, the latest released versions can be run via Python commands. HELAC-Onia allows the production of both open and hidden charm and beauty mesons in different Fock states, which are the quantum state of a particle in the Fock space. HELAC-Onia can produce single quarks but cannot perform the hadronization, consequently HELAC-Onia by itself was not sufficient to provide for all the necessary samples and the use of PYTHIA was also needed. Following the theory formalism already treated in the previous chapter, the processes that contribute to the total cross section of the double J/ψ plus a D^* production can be summarized as follows:

- **SPS**: $\sigma_{SPS} = \sigma_{SPS}^{(J/\psi+J/\psi+c\bar{c})}$
- **DPS**: $\sigma_{DPS} = \frac{\sigma_{SPS}^{(J/\psi+J/\psi+X)} \cdot \sigma_{SPS}^{(c\bar{c}+X)}}{\sigma_{\text{eff},DPS}} + \frac{1}{2}\frac{\sigma_{SPS}^{(J/\psi+c\bar{c}+X)} \cdot \sigma_{SPS}^{(J/\psi+X)}}{\sigma_{\text{eff},DPS}}$
- **TPS**: $\sigma_{TPS} = \frac{3}{3!}\frac{\sigma_{SPS}^{(J/\psi+X)} \cdot \sigma_{SPS}^{(J/\psi+X)} \cdot \sigma_{SPS}^{(c\bar{c}+X)}}{\sigma^2_{\text{eff},TPS}}$

We will refer to the first DPS contribute as DPS1 and to the second as DPS2 . The first step of the generation is based on HELAC-Onia. HELAC-Onia, if properly set, can give the result following the standard of the Les Houches Event (LHE) Files [77], which allows the user to directly interface the results with PYTHIA. Before starting the production with HELAC-Onia, the user needs to properly set the *user.inp* file where several variables are listed (the nature of the beams, the energy of the beams, the PDFs and so on): those can be changed according to the requests. Once the main variables are set, the user can also decide the *seed* of the production and, using a dedicated input file, force a particle to follow particular decay chains. To be more specific one can force one or all the particle produced to decay in one or more decay chains: in our case the J/Ψ have been forced to decay into muon pairs. In the case under exam, to have a reasonable statistic to work with, more samples of the same process were needed, each of which has been generated from a different seed, to avoid repetition. The different LHE files were then properly merged to get the final sample, large enough to analyse the kinematic of the process.

HELAC-Onia also provides the so-called *add-on codes*: the add-on codes permit the user to reproduce different processes via dedicated codes already implemented. For instance, they allow the user to produce events with a single particle in the final state using a data-driven method or produce directly events from DPS processes, by simply modifying the dedicated files. Let's take into account the add-on code number 1: by calling this command a routine in the HELAC-Onia code is evoked and the output will be a computation of the DPS cross section and the several output files formats for the event selected [3] [4].

To reproduce all the contributions listed before a few passages in the generation of the sample were needed. For the sake of clarity, the command lines used to produce the initial Les Houches files are here reported [78]:

```
SPS:  HO> generate g g > cc~(3s11) cc~(3s11) c c~

DPS:  HO> generate g g > cc~(3s11) cc~(3s11)
      HO> generate g g > cc~(3s11) c c~
      HO> generate g g > c c~
      HO> generate addon 2
      + python script to reproduce the pocket formula

TPS:  HO> generate addon 2 x 2 times
      HO> generate g g > c c~
      + python script to reproduce the pocket formula
```

Let's examine, for instance, the SPS command line: it is clear that the aim of this command is to produce two J/ψ, a quark c and an anti-quark $\bar{c}$. The symbol g represents the initial gluon, the J/ψ are identified by script `cc~(3S11)` where the tilde plays the role of the bar, meanwhile, the variables between the brackets

suggest the Fock state of the quarkonia. Hence the quarkonia here produced is in $^3S_1^{[1]}$ configuration: the [1] indicates that the quarkonium is in the colour singlet. This process involves more than 2000 Feynman diagrams and it is an example of a $2 \to 4$ process with at least two quarkonia to be calculated: this process demonstrates the robustness of HELAC-Onia to perform perturbative of more than one quarkonium production process. Here only the interaction between gluons in the initial states is considered because the luminosity of the quark-antiquark initial state is usually smaller than the gluon-gluon cross section at high-luminosity colliders such as the LHC.
In both the DPS and TPS command lines, it has been used an addon code: to generate a process via add-on code the keyword *addon* should be specified after *generate* and the number indicates the add-on code evoked by the program. In this case, the add-on code used is the second one which is dedicated to the single-quarkonium hard production. The description of the quarkonium-production mechanism is still a challenge for theorists, especially since the current state-of-art computation in NRQCD cannot describe the single quarkonium hard production data in the whole kinematical region. Hence, a data-driven way provides an economy way to generate events for a single quarkonium hard production. The initial averaged square amplitude for single- quarkonium $\mathcal{Q}$ hard production with the assumption of the dominance of the gluon-gluon channel can be expressed in a crystal ball function:

$$\overline{|\mathcal{A}_{gg\to\mathcal{Q}+X}|^2} = \begin{cases} K \exp\Big(-\kappa\frac{P_T^2}{M_\mathcal{Q}^2}\Big) & \text{when } P_T \leq \langle P_T\rangle \\ \\ K \exp\Big(-\kappa\frac{\langle P_T\rangle^2}{M_\mathcal{Q}^2}\Big)\Big(1+\frac{\kappa}{n}\frac{P_T^2-\langle P_T\rangle^2}{M_\mathcal{Q}^2}\Big) & \text{when } P_T \leq \langle P_T\rangle \end{cases} \tag{5.2}$$

where $K = \lambda^2\kappa\hat{s}/M_\mathcal{Q}^2$ and $\hat{s}$ is the partonic center-of-mass energy. Then the cross section of single quarkonium $\mathcal{Q}$ production in proton-proton collisions is:

$$\sigma_{pp\to\mathcal{Q}+X} = \int dx_1 dx_2 f_g(x_1) f_g(x_2)\frac{1}{2\hat{s}}\overline{|\mathcal{A}_{gg\to\mathcal{Q}+X}|^2}\text{dLIPS} \tag{5.3}$$

where f_g is the gluon pdf and dLIPS is the Lorentz-invariant phase space measure for $pp \to \mathcal{Q} + X$. The coefficients λ, κ, n and $\langle P_T\rangle$ can be determined by fitting it to the experimental data [3] [4].

As parton distribution function for the generation we used the CTEQ6L1 set [79] and the factorization scale is $\mu_f = \sqrt{m_i^2 + p_t^2}$ where i is the quarkonium or the quark according to the case.

The Les Houches files produced via HELAC-Onia have afterward passed to PYTHIA which firstly hadronize the c quark and force D^* meson to decay in the chosen decay channel. The fragmentation fraction for the $D*$ is $FF_{D^*} = 0.243$ [80].

5.3 The Les Houches Events File structure and merging

The Les Houches Events File (LHEF) is a standard format, XML-like, born in the wake of the Les Houches Accords [81], which are agreements between particle physicists to standardize the interface between the matrix element calculations and Monte Carlo events generators.

An example of an LHEF is shown in figure 5.3. The first block of the LHE file is the init block enclosed between the string `<init>`, which indicates where the block starts, and the `</init>`, which indicates where the block ends. The init block is where the major information about the event generation are summarized: in the first line the first two integers identify the nature of the beams, followed by their energy (3rd and 4th integers); the following four numbers identify the PDFs, meanwhile, the last two numbers represent the weighting strategy and the number of processes. In the second line, the process info are listed: the cross section and its error, the unit weight and the ID code for the process.

Following the init block there are the event blocks: here all the initial particles of the events are listed. Each of the thirteen columns contains specific information about the event and the particles: in the first one there is the particle ID following the PDG MC standard, then the status of the particle, i.e. -1 for an incoming particle or 1 for outgoing final state particle. The third and fourth columns are the first mother ID and the second mother ID. The mother ID is not attributed according to the PDG ID codes but is the number of the line where the mother is: for instance, the second mother ID must be zero if the particle is a decay product. The next two columns are reserved for the colours code: in the LHEF the colour labels do not follow the QCD standard, i.e. the colour 101 or 103 might represent the same colour depending on the process, this is because the colour codes are used in PYTHIA only to make sure that the process is correctly reconstructed and it follows a physical colour flow (see figure 5.2).

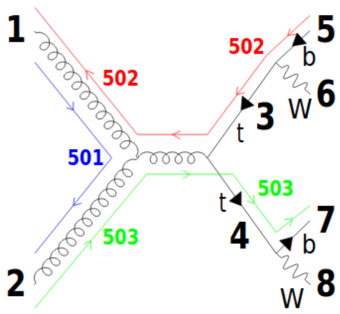

Figure 5.2: Example of a color flow in an hadron $t\bar{t}$ production.

The remaining columns contain the other relevant information about the particle.

```
<LesHouchesEvents version="3.0">
<!--
File generated with HELAC-ONIA
-->
<init>
2212    2212  6.500000E+03  6.500000E+03        0        0   10042   10042       3       1
5.3644270565E+09    8.3637019404E+06    1.0000000000E+00    81
</init>
<event>
 4    81  5.870011E+04  1.569509E+00  7.299270E-03  3.817764E-01
21    -1     0     0  103  101  0.000E+00  0.000E+00  2.511E-03  2.511E+03  0.000E+00  0.000E+00  9.00E+00
21    -1     0     0  101  102  0.000E+00  0.000E+00 -2.854E+03  2.854E+03  0.000E+00  0.000E+00  9.00E+00
 4     1     1     2  103    0 -4.606E-01 -3.345E-02 -2.709E+02  2.709E+02  1.500E+00  0.000E+00  9.00E+00
-4     1     1     2    0  102  4.606E-01  3.345E-02 -2.583E+03  2.583E+03  1.500E+00  0.000E+00  9.00E+00
</event>
```

Figure 5.3: LHEF example: the <init> and the <event> blocks are shown. To make the image more legible the numerical strings are, in this image and in the ones below, reported with a reduced precision.

In order to produce the necessary samples for studying the signal and the background events, a careful study of the LHEF structure was needed. Despite HELAC-Onia being able to generate DPS events via add-on codes, the ones needed for the case here under analysis cannot be produced directly, consequently, it was necessary to produce SPS events and then, using a Python script, merge the LHEF to reproduce the full DPS event at the parton level, namely before the showering [82]. This passage was necessary to reproduce the pocket formula as presented in the previous chapter: this way of proceeding is based on the strong assumption that a DPS process can be factorized into non-correlated SPS processes, which are indeed produced independently. Merging the events in an LHE file requires a little bit of practice and a preliminary study on the meaning and role of each label in order to modify them where needed. In fact, without the necessary changes, PYTHIA would not be able to reconstruct the colour flow and/or success in hadronization. The python script reads the first LHEF in input and saves all the events in the output file, but before closing each event, the particles of the events in the second file in input are added event per event. The first label to be changed is then the number of the total particles in each event which will become the sum of the total particles of the event of the first file and the total particle of the event of the second one. If this number is not changed, PYTHIA will not be able to process all the particle lines and will stop at the initial number of lines indicated by the original label. After the merging procedure, the numbering of the lines has changed, thereafter, for consistency, all the relationships between the particles must be carefully updated. Although at this point the parenting links between the particles should be clear enough to reconstruct the event history, PYTHIA fails in reconstructing the colour flow, thereby, also the colour labels must be customized. Each hard process should use different colour codes from the others, i.e. if the first hard process has the colour label from 101 to 103, the second one should use any other numbers despite the ones from 101 to 103. The colour labels have been changed according to the colour flow in the event before the merging procedure. A similar merging procedure has been used also for the other DPS process. To seek clarity the event blocks of the two SPS (figure 5.4) files and the event block of the merged DPS (figure 5.5) file are reported. An example of a TPS event will be reported in Appendix A in a short version since the number of particles produced is huge and the number of the lines would not fit within a page.

```
<event>
  7    81  7.738597E+01  3.611283E+00  7.299270E-03  2.684900E-01
 21    -1    0    0  102  101  0.00E+00  0.00E+00  7.83E-01  7.83E-01  0.00E+00  0.0  9.0
 21    -1    0    0  104  102  0.00E+00  0.00E+00 -5.80E+01  5.80E+01  0.00E+00  0.0  9.0
443     2    1    2    0    0  1.40E+00  1.44E+00 -4.34E+01  4.35E+01  3.00E+00  0.0  9.0
  4     1    1    2  104    0 -5.69E-01  7.26E-01 -1.15E+01  1.16E+01  1.50E+00  0.0  9.0
 -4     1    1    2    0  101 -8.31E-01 -2.16E+00 -2.33E+00  3.62E+00  1.50E+00  0.0  9.0
-13     1    3    0    0    0  4.85E-01  1.80E+00 -1.29E+01  1.30E+01  0.00E+00  0.0  9.0
 13     1    3    0    0    0  9.16E-01 -3.61E-01 -3.04E+01  3.05E+01  0.00E+00  0.0  9.0
</event>

<event>
  6    82  7.284052E+04  3.104937E+00  7.299270E-03  1.180000E-01
 21    -1    0    0  101  103  0.00E+00  0.00E+00  5.40E-03  5.40E-03  0.00E+00  0.0  9.0
 21    -1    0    0  103  102  0.00E+00  0.00E+00 -5.83E+02  5.83E+02  0.00E+00  0.0  9.0
443     2    1    2    0    0 -1.69E-01  1.63E-01 -4.55E+02  4.55E+02  3.09E+00  0.0  9.0
 21     1    1    2  101  102  1.69E-01 -1.63E-01 -1.28E+02  1.28E+02  0.00E+00  0.0  9.0
-13     1    3    0    0    0  2.02E-01  1.36E+00 -3.55E+02  3.55E+02  0.00E+00  0.0  9.0
 13     1    3    0    0    0 -3.71E-01 -1.20E+00 -9.98E+01  9.98E+01  0.00E+00  0.0  9.0
</event>
```

Figure 5.4: Event blocks of the SPS processes: in the first one the production of a $J/\psi(443)$ decaying into a muon(13) and an anti-muon(-13) plus a quark c(4) and anti-quark c(-4) and in the second one the production of a single J/ψ are shown. It should be noted that the total number of the particles is 7 in the first block and 6 in the second. The parenting relationships and color labels are also noteworthy.

```
<event>
 13    81  7.738597E+01  3.611283E+00  7.299270E-03  2.684900E-01
 21    -1    0    0  102  101  0.00E+00  0.00E+00  7.83E-01  7.83E-01  0.00E+00  0.0  9.0
 21    -1    0    0  104  102  0.00E+00  0.00E+00 -5.80E+01  5.80E+01  0.00E+00  0.0  9.0
443     2    1    2    0    0  1.40E+00  1.44E+00 -4.34E+01  4.35E+01  3.00E+00  0.0  9.0
  4     1    1    2  104    0 -5.69E-01  7.26E-01 -1.15E+01  1.16E+01  1.50E+00  0.0  9.0
 -4     1    1    2    0  101 -8.31E-01 -2.16E+00 -2.33E+00  3.62E+00  1.50E+00  0.0  9.0
 21    -1    0    0  105  107  0.00E+00  0.00E+00  5.40E-03  5.40E-03  0.00E+00  0.0  9.0
 21    -1    0    0  107  106  0.00E+00  0.00E+00 -5.83E+02  5.83E+02  0.00E+00  0.0  9.0
443     2    6    7    0    0 -1.69E-01  1.63E-01 -4.55E+02  4.55E+02  3.09E+00  0.0  9.0
 21     1    6    7  105  106  1.69E-01 -1.63E-01 -1.28E+02  1.28E+02  0.00E+00  0.0  9.0
-13     1    8    0    0    0 -5.71E-01  1.01E+00 -4.05E+02  4.05E+02  0.00E+00  0.0  9.0
 13     1    8    0    0    0  4.02E-01 -8.56E-01 -5.03E+01  5.03E+01  0.00E+00  0.0  9.0
 13     1    3    0    0    0  9.16E-01 -3.61E-01 -3.04E+01  3.05E+01  0.00E+00  0.0  9.0
-13     1    3    0    0    0  4.85E-01  1.80E+00 -1.29E+01  1.30E+01  0.00E+00  0.0  9.0
</event>
```

Figure 5.5: Event block of a DPS event. It should be noticed here how the parenting relationships have been changed to reproduce the correct event history and how the colour labels for the second hard process have been adapted to not interfere with the colour flow of the first hard process.

Another crucial change needed to get PYTHIA correctly read and hadronize the DPS sample concerning the order of the lines. PYTHIA is capable to produce an event starting from the beams collision to the final step where only the detectable particle remains. In order to produce the full process PYTHIA follows three logical steps: the `ProcessLevel`, the `PartonLevel` step and the `HadronLevel` step. The `ProcessLevel` class administrates the initial step of the event generation, wherein the basic process is selected. Currently, this is done either using some of the internal processes or with Les Houches Accord input. The `PartonLevel` class administrates the middle step of the event generation, i.e. the evolution from an input (hard) process from `ProcessLevel`, containing a few partons only, to a complete parton-level configuration to be handed on to `HadronLevel`. The `PartonLevel` involves the application of initial- and final-state radiation, multi-parton interactions and the structure of beam remnants. The `HadronLevel` class administrates the final step of the event generation, wherein the partonic configuration from `PartonLevel` is hadronized, including string fragmentation and secondary decays.

By merging the LHEF directly, without changing the order of the lines, PYTHIA fails in the hadronization step, more precisely cannot reconstruct the event history properly. This limit maybe can be attached to the internal subroutines of PYTHIA, which would expect the order of the lines of an event to follow the logical steps adopted by the machinery. As the logic suggests, the muon pairs will be present only after both the J/ψ have been produced in as much as they are produced by their decay. In fact, just moving the muon pair belonging to the first J/ψ decay at the latest lines of the event, as can be appreciated in figure 5.5, PYTHIA correctly reconstructs the event history and hadronize the sample.

For the TPS sample, a whole different procedure has been adopted. Here, the limits of processing $n > 2$ hard processes in PYTHIA have been circumvented by changing the order of the merging and the hadronization. The three SPS sample of two single J/ψ and a couple of c and $\bar{c}$ have been showered in PYTHIA and only in a second moment merged. The merging procedure for the TPS case is obtained via python script and using the *pylhe* library [83], which allows reading an LHEF similarly to an XML file, namely accessing the blocks via specific methods and classes. The use of this library was necessary to correctly merge the events block since in this case both the number and the types of particles in a single event were not fixed. The merged LHEF was then passed to PYTHIA: this passage was necessary to produce the output file in the root file format [84]. For this passage, all the flags concerning the generation have been switched off: `ProcessLevel:all=off`, `PartonLevel:all=off` and `HadronLevel:all=off`. This has been done since the showering procedure has concluded, and its product have been saved in the step prior to the merge step: thus, there was no need to call the three subroutines. In addition, if left switched on, PYTHIA would have failed the `HadronLevel` and would have aborted the code; which is among other things the reason why the TPS events requires these special treatments. Since after the merging procedure no more processes were required to PYTHIA, the color scheme correction done for the DPS, was not necessary in this case; on the other hand the information on mother-daughter relationship has been upgraded following the logic used for the DPS case. In fact, the information on the relationship between particle was necessary to reconstruct in a first moment the decay chains.

5.3.1 Insights on the single J/ψ production

A first look to the plots of the single J/ψ produced via addon code allowed the observation of the event distribution in the phase space. The addon codes are based on the VEGAS generator [85], which cannot produce disorder events in the phase space [78]. Hence, if one needs to use a sub-sample from the total sample or use it in a non trivial way, it is mandatory to keep in mind this generator feature.

To produce the TPS sample I selected two sub-samples from the total single J/ψ LHEF, picking the events at regular intervals: this selection mode ensure the sub-sample to spread to the whole phase space. Afterward, the sub-samples, which now covers the whole phase space but still present an order, need to be randomly re-arranged. This last step is crucial: if the samples are not randomly re-arranged, once they are merged into the TPS sample, in each event the two J/ψ belong to the same phase space region and that adds a non negligible correlation grade. The sub-samples have been re-arranged via python script.

Chapter 6

Kinematic study at Generation Level and possible analysis scenarios

In order to characterize the signal and the background distributions at the Generation Level, following the standard of the N parton interactions, the choice of the variables to study fell on the transverse momentum, the pseudorapidity and ϕ; in addition to the mere kinematic variables, their relative differences or product, $\Delta\eta$ and $\Delta\phi$, $\eta_i \times \eta_j$, between the charmed mesons have also been observed in order to enhance possible correlations.

To understand which variables are more indicative for the signal characterization, a first glance to the distribution was necessary: each sample has been re-weighted in terms of the specific cross section in order to have a clue of the relative weight of the processes. At this first step, the distributions are here obtained by using the Monte Carlo truth: each particle is correctly timely located into the decay chain by the so-called *mother-daughter* relationships, which are implied in the event history reconstruction by asking for the particle PDG ID [86].

Afterward, taking into account the acceptance of the detectors and leaving behind the Monte Carlo truth, the events have been reconstructed using the kinematic and PID information (in the muons' case, since in CMS they are identified by a dedicate trigger) and applying additional conditions for the decay characterization.

This procedure allows to understand the algorithmic selection efficiency for each process and to start drawing a selection strategy for this specific final state.

Each step will be described in detail in the next paragraphs.

6.1 Cross section and expected events

The cross sections for the single SPS processes have been calculated by HELAC-Onia; their values are reported in table 6.1.

Process	value in mb
$\sigma_{SPS}(J/\psi + X)$	$(0.1790 \pm 0.0002) \times 10^{-1}$
$\sigma_{SPS}(c\bar{c} + X)$	$(0.5364 \pm 0.0008) \times 10^{1}$
$\sigma_{SPS}(J/\psi + J/\psi + X)$	$(0.1920 \pm 0.0006) \times 10^{-4}$
$\sigma_{SPS}(J/\psi + c\bar{c} + X)$	$(0.2379 \pm 0.0044) \times 10^{-2}$
$\sigma_{SPS}(J/\psi + J/\psi + c\bar{c} + X)$	$(0.229 \pm 0.0195) \times 10^{-6}$
Sigma effective	value in mb
$\sigma_{\text{eff, DPS}}$	15 ± 10
$\sigma_{\text{eff,TPS}}$	12.5 ± 9.0

Table 6.1: The SPS cross sections, calculated by HELAC-Onia, and the sigma effective for DPS and TPS processes are here reported in mb.

The uncertainties for the SPS productions in HELAC-Onia are a Monte Carlo statistical error due to Monte Carlo numerical integration. In order to have a full vision on the uncertainties at this level, scale uncertainty and PDF uncertainty should also be taken into account in a second moment and are expected to be dominant. In a charm production at the LHC larger uncertainties are foreseen. For what concerns the sigmas effective: for the $\sigma_{\text{eff,DPS}}$ the choice fell on a value, usually used as benchmark since there is no a definitive value foreseen by theory, nor a clear indication from measurements as shown in 4.9. The uncertainty used has been chosen bearing in mind the trend showed in figure 4.9. Consequently for the $\sigma_{\text{eff,TPS}}$ the value here used is the one estimated in [71] and the error has been re-adapted keeping constant the relative error between the uncertainties here used and the ones estimated in [71]. The SPS cross sections are then used to compute the DPS and TPS cross sections, reported in 6.2, using the pocket formula formalism as explained in the previous chapter.

Process	value in mb	expected event at $138 fb^{-1}$ ($c\bar{c}$)	expected event at $138 fb^{-1}$
σ_{SPS}	0.229×10^{-6}	41.262×10^{3}	16
σ_{DPS}	0.349×10^{-4}	48.162×10^{5}	18×10^{3}
σ_{TPS}	0.549×10^{-3}	75.762×10^{6}	29×10^{3}

Table 6.2: The SPS, DPS and TPS cross sections calculated using the pocket formula and the expected events.

Between the SPS cross-section and the TPS one there are three orders of magnitudes, which make the SPS contribute negligible. Hence the DPS will represent the main background. In the third and fourth columns the expected events have been calculated using the integrated luminosity of RUN II: the former the expected events include all the possible charmed mesons, in the latter the events have been calculated taking into account the D^* fragmentation fraction $FF_{D^*} = 0.243$ [80], the branching ratio (BR) $D^{*+} \to D^0\pi^+_{\text{slow}} \approx 67.7\%$, BR $D^0 \to K^-\pi^+ \approx 3.93\%$ and BR $J/\psi \to \mu^+\mu^- \approx 5.93\%$ [87].

6.2 A first glance to the distributions at Monte Carlo truth level

In this section the principal distributions will be reported: as already anticipated, each contribute has been re-weighted in terms of the specific SPS cross section, effective cross section and combinatorial factor.

For seek of clarity we firstly report the diagrams of the four process in figure 6.1: SPS, DPS1, DPS2 and TPS. The label DPS1 refers to the $\sigma_{\text{SPS}}(J/\psi + J/\psi) \times \sigma_{\text{SPS}}(D^*)$ distributions, meanwhile the DPS2 refers to the $\sigma_{\text{SPS}}(J/\psi + D^*) \times \sigma_{\text{SPS}}(J/\psi)$ ones, as specified in the previous chapter.

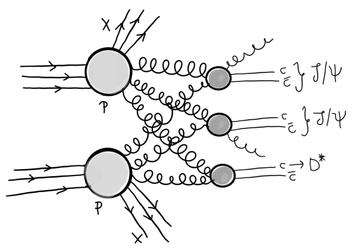

(a) TPS process.

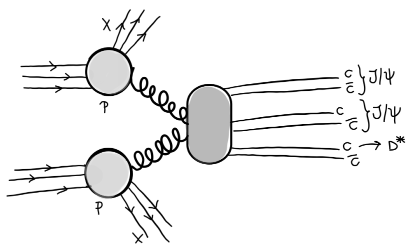

(b) SPS process.

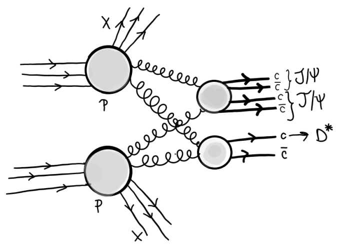

(c) DPS1 process.

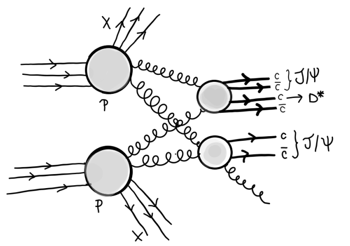

(d) DPS2 process.

Figure 6.1: Diagrammatic representation of the four produced processes.

The J/ψ are labeled with L and sL that stand for *Leading*, respectively, and *sub-Leading*: the transverse momentum has been used to discriminate the two charmonia. The same logic has been applied to the muons obtained from the J/ψ decays: the four final muons have been sorted from the most energetic (*Leading*) to the least energetic (*sub-sub-sub-Leading*). In some cases the SPS plots have been multiplied by a factor of 10 or 100 to emphasize the distributions and allow the reader to better appreciate their shape.

6.2.1 Kinematic variables distribution

From figure 6.2 to 6.7, as indicated in the legend, the three different contributions (SPS, DPS, TPS) for each kinematic variable chosen are shown. From 6.8 figure to 6.9, the scatter plots are shown: here in the x axis the transverse momentum is represented, meanwhile in the y axis there is the η distribution. The scatter plots are propaedeutic to the kinematic cuts, where the events are selected to be in the acceptance region for the pseudorapidity and to respect different criteria on the transverse momentum. From these graphs it is clear that the most populated region is the one at low p_T, that, together with a large spread in η foretell a low selection acceptance.

As one would expect, the distributions in terms of the angle ϕ are almost uniform: that is because there is no preferential angle, thus the events are expected to be isotropic. The visible oscillations in same sample have been attributed to statistical fluctuations and scaling effects.

For the same kinematic reasons the η distributions are expected to be symmetric with respect to zero point: although in some distributions a small asymmetry is present and, once again, this may be linked to a statistical fluctuation or, more likely, to some unknown generator feature that would be deeper investigated in the future.

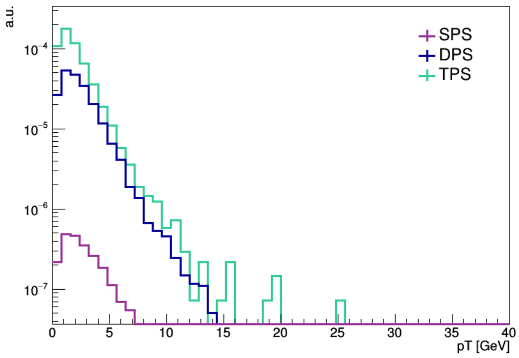

(a) D^*: transverse momentum distribution.

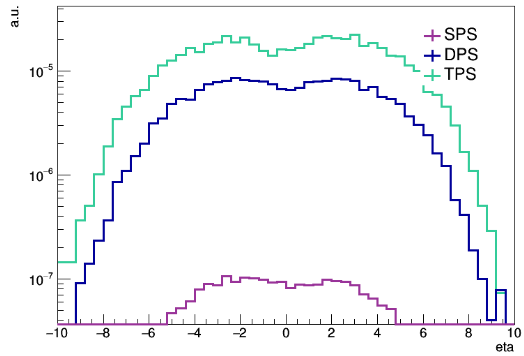

(b) D^*: η distribution.

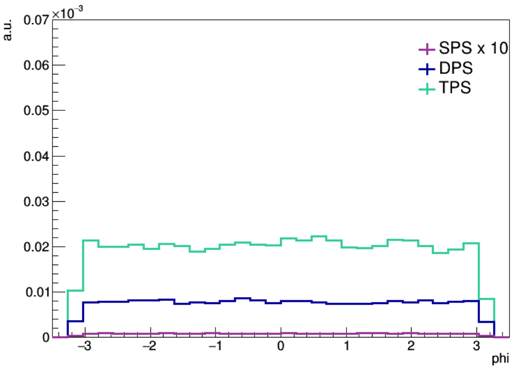

(c) D^*: ϕ distribution.

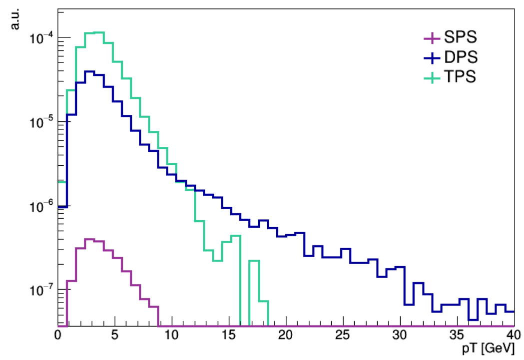

(d) J/ψ_L: transverse momentum distribution.

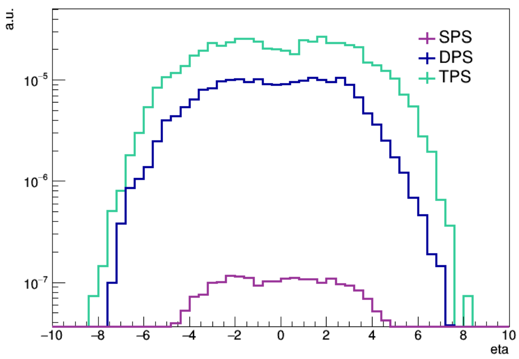

(e) J/ψ_L: η distribution.

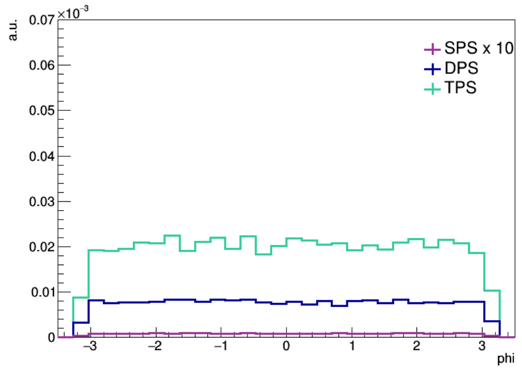

(f) J/ψ_L: ϕ distribution.

Figure 6.2: In figure 6.2a, 6.2b, 6.2c are shown, respectively, the p_T, η and ϕ distributions for the D^*, meanwhile in figure 6.2d, 6.2e and 6.2f are shown the p_T, η and ϕ distributions for the J/ψ leading.

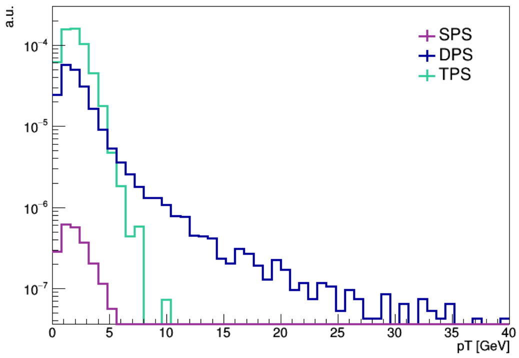

(a) J/ψ_{sL}: transverse momentum distribution.

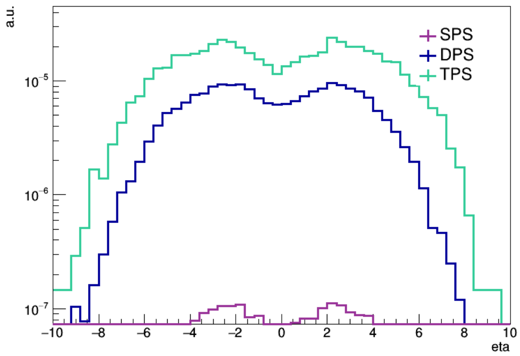

(b) J/ψ_{sL}: η distribution.

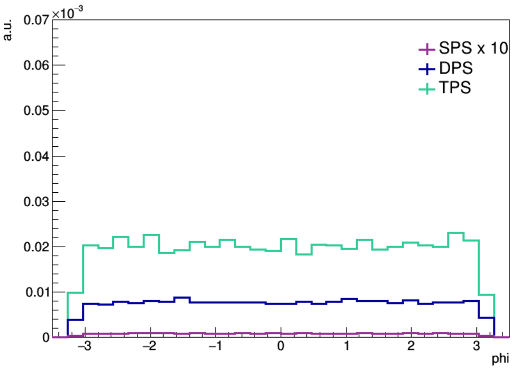

(c) J/ψ_{sL}: ϕ distribution.

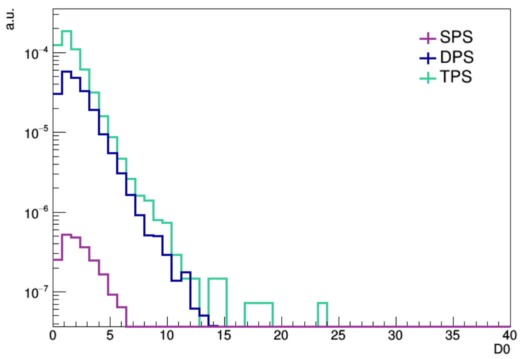

(d) D^0: transverse momentum distribution.

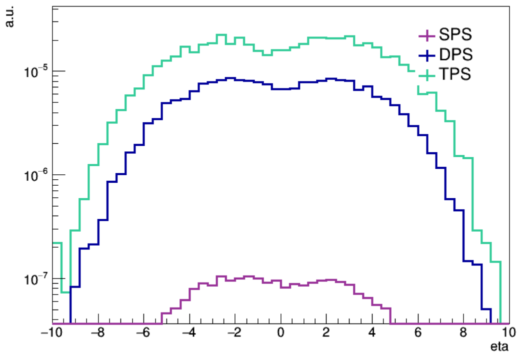

(e) D^0: η distribution.

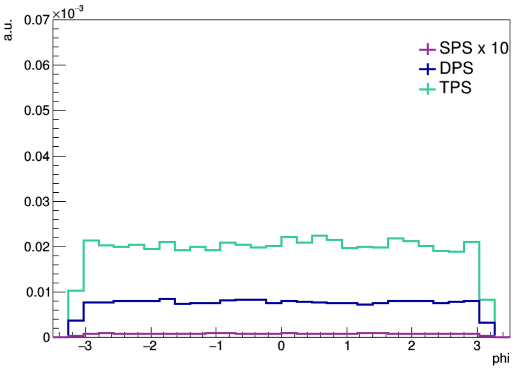

(f) D^0: ϕ distribution.

Figure 6.3: In figure 6.3a, 6.3b, 6.3c are shown, respectively, the p_T, η and ϕ respective distributions for the J/ψ sub-leading, meanwhile in figure 6.3d, 6.3e and 6.3f are shown the p_T, η and ϕ distributions for the D^0.

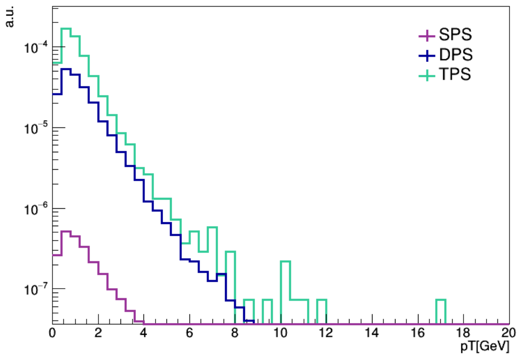

(a) π: transverse momentum distribution.

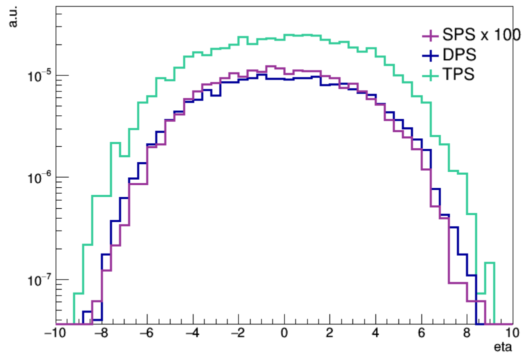

(b) π: η distribution.

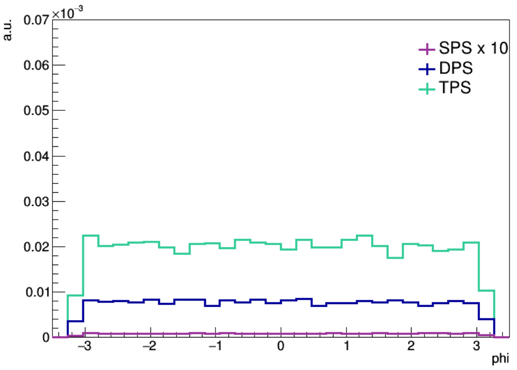

(c) π: ϕ distribution.

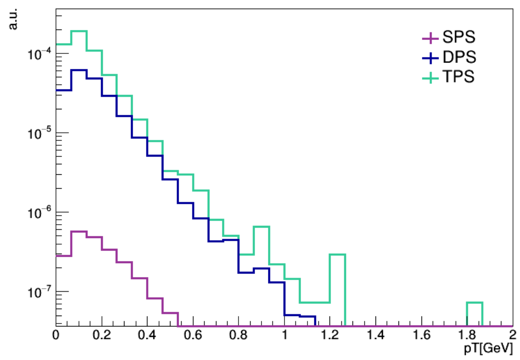

(d) π_{slow}: transverse momentum distribution.

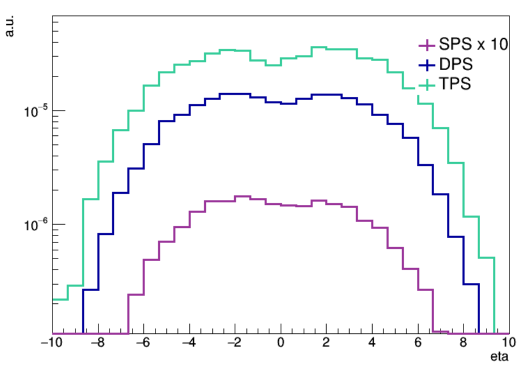

(e) π_{slow}: η distribution.

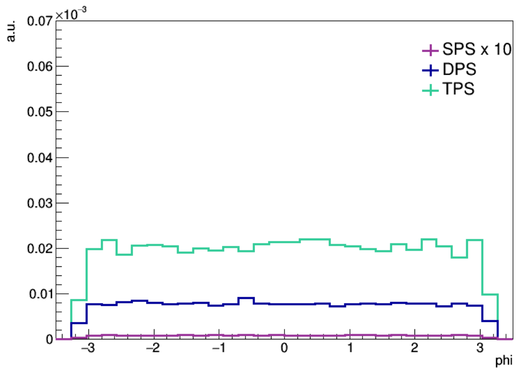

(f) π_{slow}: ϕ distribution.

Figure 6.4: In figure 6.4a, 6.4b, 6.4c are shown, respectively, the p_T, η and ϕ respective distributions for the π, meanwhile in figure 6.4d, 6.4e and 6.4f are shown the p_T, η and ϕ distributions for the π_{slow}.

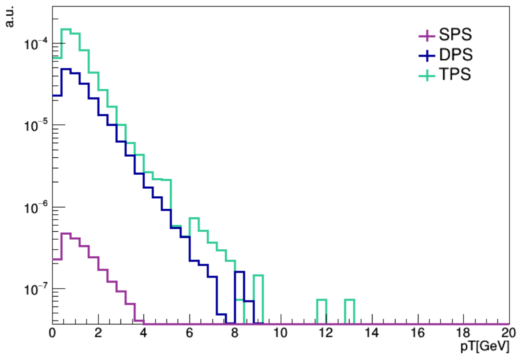

(a) K: transverse momentum distribution.

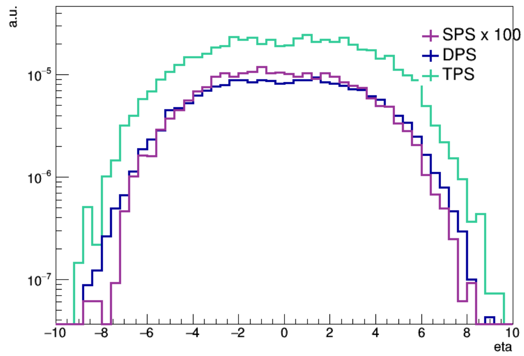

(b) K: η distribution.

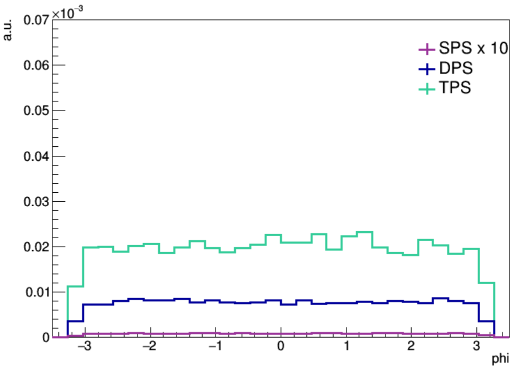

(c) K: ϕ distribution.

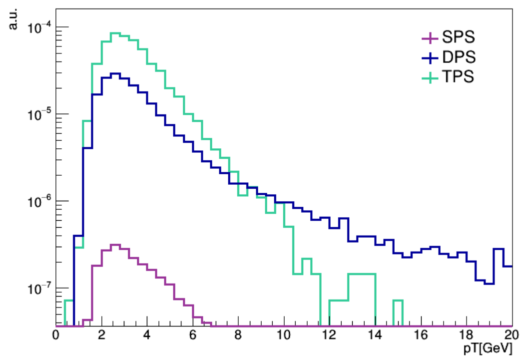

(d) μ_L: transverse momentum distribution.

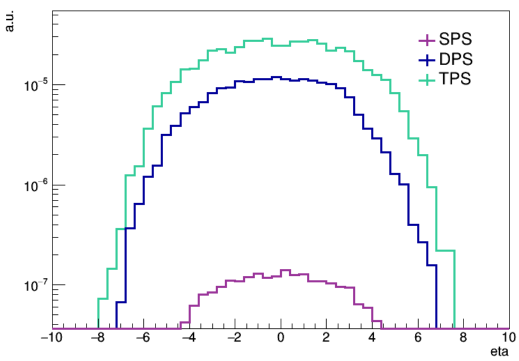

(e) μ_L: η distribution.

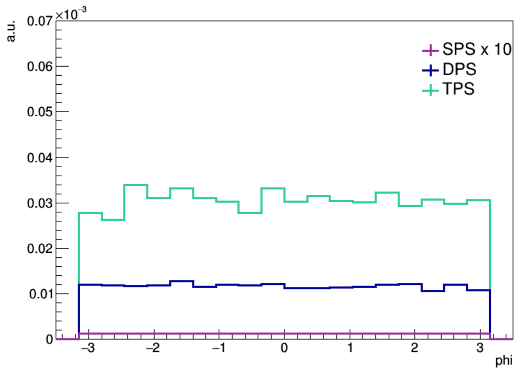

(f) μ_L: ϕ distribution.

Figure 6.5: In figure 6.5a, 6.5b, 6.5c are shown, respectively, the p_T, η and ϕ respective distributions for the K, meanwhile in figure 6.5d, 6.5e and 6.5f are shown the p_T, η and ϕ distributions for the μ leading.

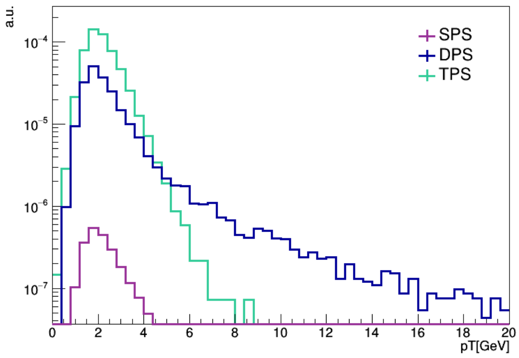

(a) μ_{sL}: transverse momentum distribution.

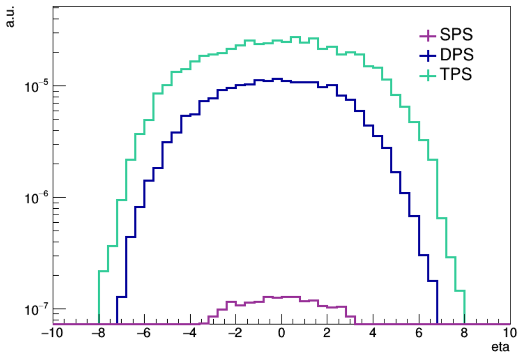

(b) μ_{sL}: η distribution.

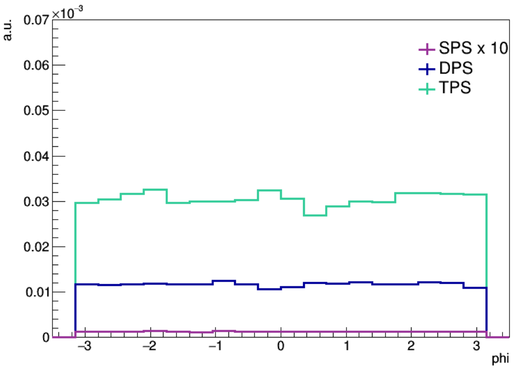

(c) μ_{sL}: ϕ distribution.

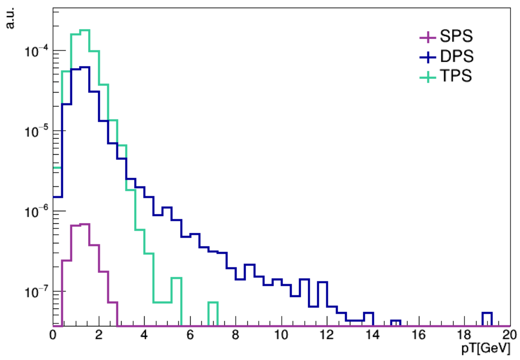

(d) μ_{ssL}: transverse momentum distribution.

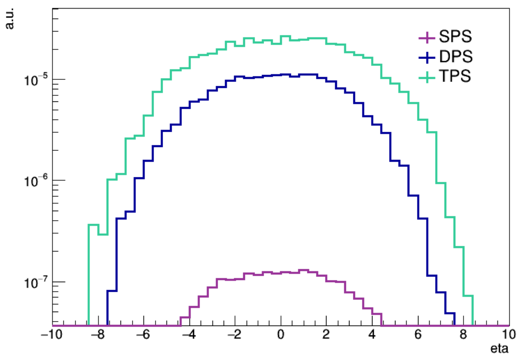

(e) μ_{ssL}: η distribution.

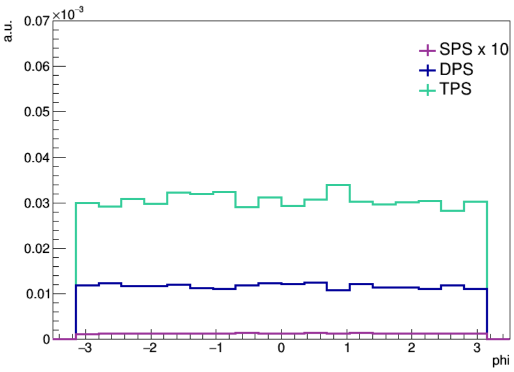

(f) μ_{ssL}: ϕ distribution.

Figure 6.6: In figure 6.6a, 6.6b, 6.6c are shown, respectively, the p_T, η and ϕ respective distributions for the μ sub-leading, meanwhile in figure 6.6d, 6.6e and 6.6f are shown the p_T, η and ϕ distributions for the μ sub-sub-leading.

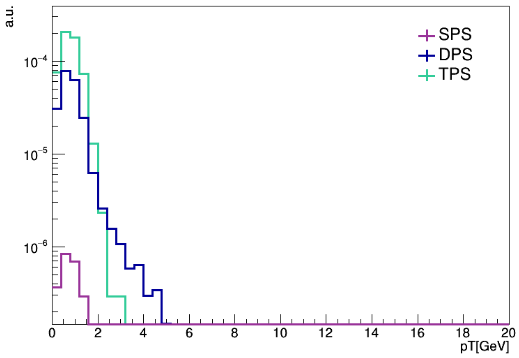

(a) μ_{sssL}: transverse momentum distribution.

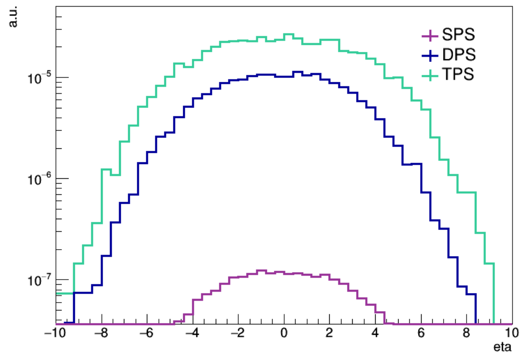

(b) μ_{sssL}: η distribution.

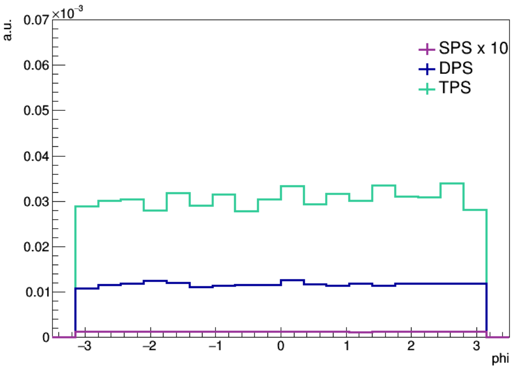

(c) μ_{sssL}: ϕ distribution.

Figure 6.7: In figure 6.7a, 6.7b, 6.7c are shown, respectively, the p_T, η and ϕ respective distributions for the μ sub-sub-sub-leading.

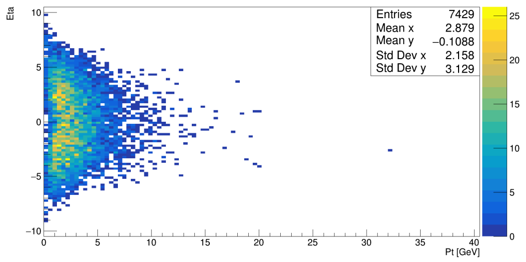

(a) Each entry in the x axis indicates the p_T and the y position indicates the η for the D^* in the SPS case.

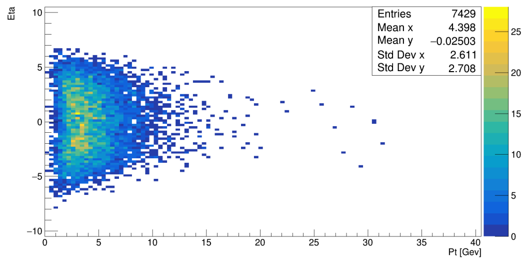

(b) Each entry in the x axis indicates the p_T and the y position indicates the η for the J/ψ_L in the SPS case.

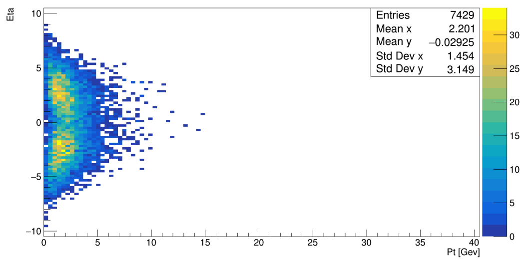

(c) Each entry in the x axis indicates the p_T and the y position indicates the η for the J/ψ_{sL} in the SPS case.

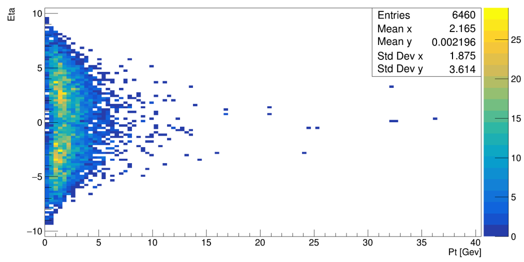

(d) Each entry in the x axis indicates the p_T and the y position indicates the η for the D^* in the DPS1 case.

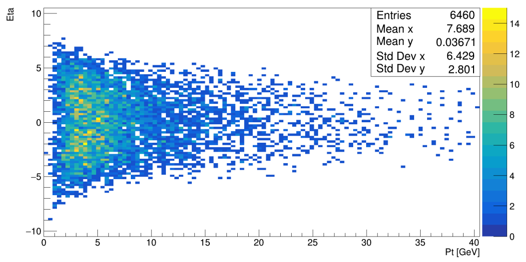

(e) Each entry in the x axis indicates the p_T and the y position indicates the η for the J/ψ_L in the DPS1 case.

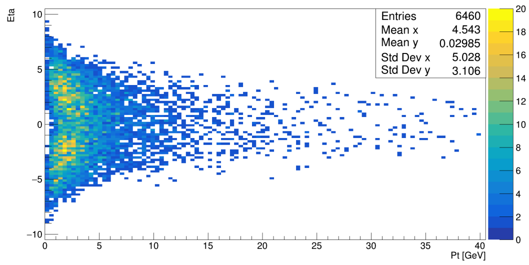

(f) Each entry in the x axis indicates the p_T and the y position indicates the η for the J/ψ_{sL} in the DPS1 case.

Figure 6.8: Scatter plots in the SPS and $\sigma_{\rm SPS}(J/\psi + J/\psi) \times \sigma_{\rm SPS}(D^*)$ (DPS1) cases.

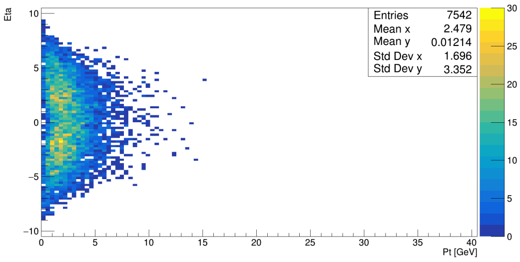

(a) Each entry in the x axis indicates the p_T and the y position indicates the η for the D^* in the DPS2 case.

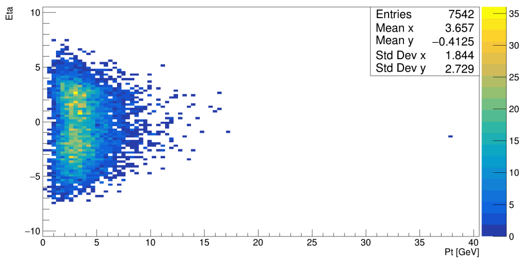

(b) Each entry in the x axis indicates the p_T and the y position indicates the η for the J/ψ_L in the DPS2 case.

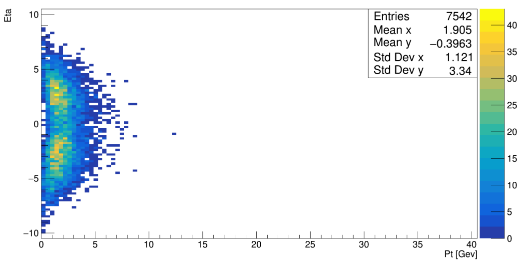

(c) Each entry in the x axis indicates the p_T and the y position indicates the η for the J/ψ_{sL} in the DPS2 case.

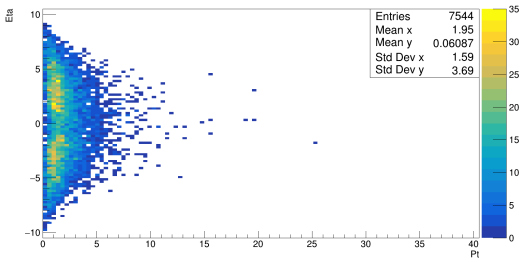

(d) Each entry in the x axis indicates the p_T and the y position indicates the η for the D^* in the TPS case.

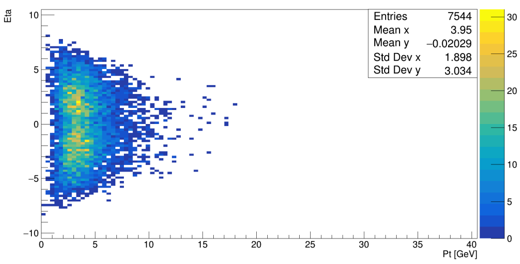

(e) Each entry in the x axis indicates the p_T and the y position indicates the η for the J/ψ_L in the TPS case.

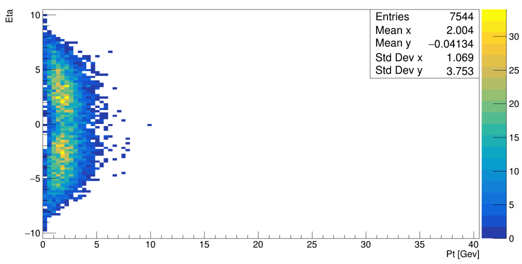

(f) Each entry in the x axis indicates the p_T and the y position indicates the η for the J/ψ_{sL} in the TPS case.

Figure 6.9: Scatter plots in the $\sigma_{\text{SPS}}(J/\psi + D^*) \times \sigma_{\text{SPS}}(J/\psi)$ (DPS2) and TPS cases.

The scatter plots are useful in order to visualize the correlation between two variables. In this case the plots suggest that the events are concentrated in a low p_T region, and that there is a large spread in η: this will lead to a small efficiency when the fiducial phase space for CMS will be taken into account.

Insight on the difference between the DPS contributes

In the following analysis two different DPS contributions are separated for a complete characterization of the background processes.

It is recalled the meaning of the labels DPS1 and DPS2 as shown in figure 6.1c and 6.1d, respectively. Only the distributions where there is a significance difference between the two DPS contributes will be reported.

It is important to underline how the DPS1 is, from a kinematic point of view, closer to the SPS case; on the other hand the DPS2 is closer, from the same kinematic point of view, to the signal. This is clear in the charmonia production: in the SPS and DPS1 cases the J/ψ are produced in the same hard scattering interaction, at the contrary, in the DPS2 and TPS cases they are from two different parton interactions. Hence, both the necessary energy to produced the peculiar processes, together with the modelization used are assumed to be the primary sources of the kinematic differences between the processes. This behavior is especially noticeable when it comes to the correlation variables: $\Delta\eta$, $\Delta\phi$ and $\eta_i \times \eta_j$ (see 6.2.2). This might suggest that these variables may play a key role in discriminating the signal from the background.

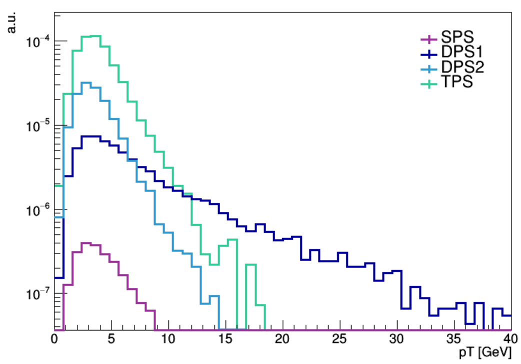

(a) $J/\psi_{\rm L}$: transverse momentum distribution.

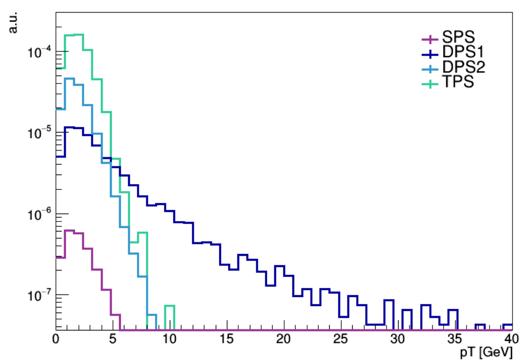

(b) $J/\psi_{\rm sL}$: transverse momentum distribution.

Figure 6.10: In figure 6.10a and 6.10b are shown, respectively, the p_T distributions for the charmonia leading and sub-leading.

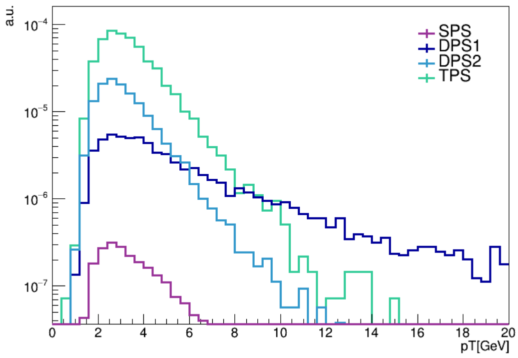

(a) μ_{L}: transverse momentum distribution.

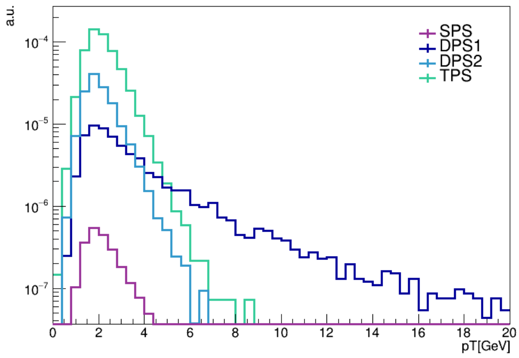

(b) μ_{sL}: transverse momentum distribution.

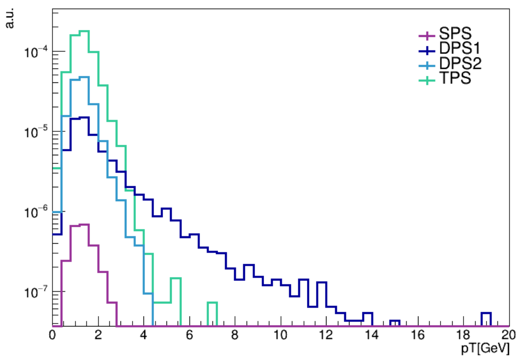

(c) μ_{ssL}: transverse momentum distribution.

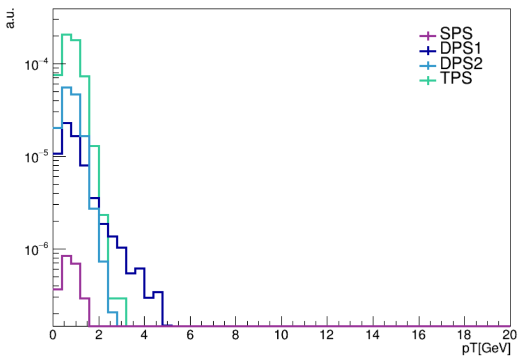

(d) μ_{sssL}: transverse momentum distribution.

Figure 6.11: In figure 6.11a, 6.11b, 6.11c and 6.11d are shown the p_T distributions for the muons.

6.2.2 Correlation variables

From figure 6.12 to 6.15, the correlation variables are shown. Each distribution is here presented in two versions: on the left the plots have been re-weighted with the specific cross section and the two DPS processes are displayed as one single contribution, while on the right they are normalized to one and the DPS1 and DPS2 are kept separated to enhance the different behaviour.

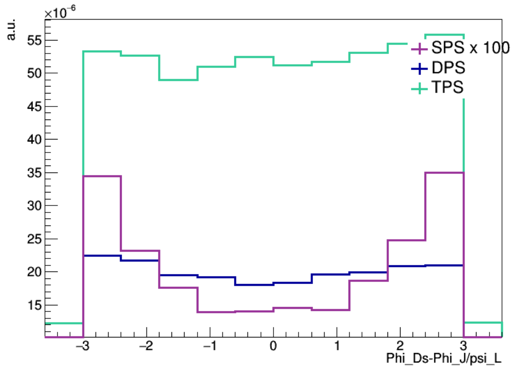

(a) $\Delta(\phi_{D^*} - \phi_{J/\psi_L})$ distribution.

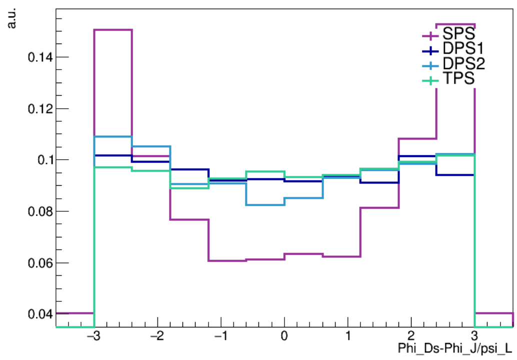

(b) $\Delta(\phi_{D^*} - \phi_{J/\psi_L})$ distribution.

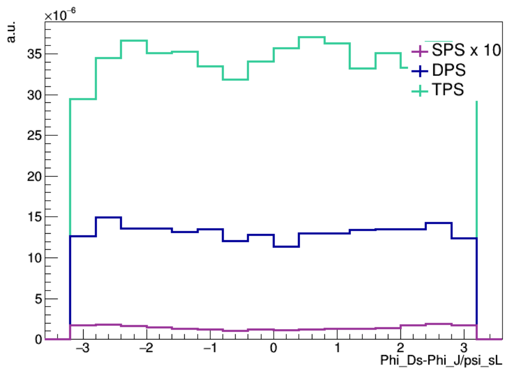

(c) $\Delta(\phi_{D^*} - \phi_{J/\psi_s L})$ distribution.

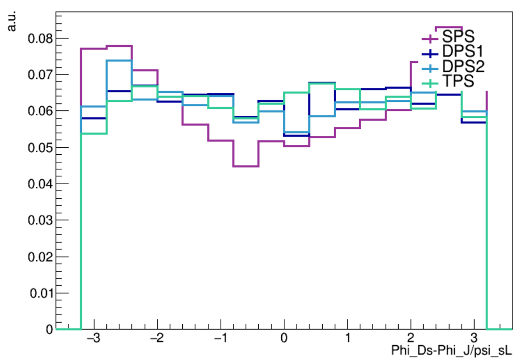

(d) $\Delta(\phi_{D^*} - \phi_{J/\psi_s L})$ distribution.

Figure 6.12: In figure 6.12a (6.12b) and 6.12c (6.12d) are shown the $\Delta(\phi_{D^*} - \phi_{J/\psi_L})$ and $\Delta(\phi_{D^*} - \phi_{J/\psi_s L})$ distributions.

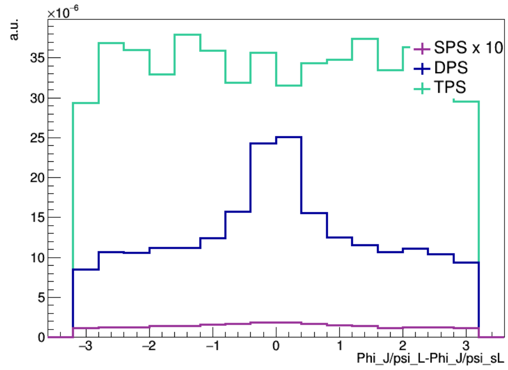

(a) $\Delta(\phi_{J/\psi_L} - \phi_{J/\psi_{sL}})$ distribution.

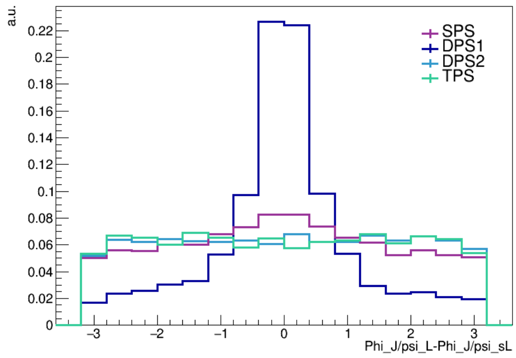

(b) $\Delta(\phi_{J/\psi_L} - \phi_{J/\psi_{sL}})$ distribution.

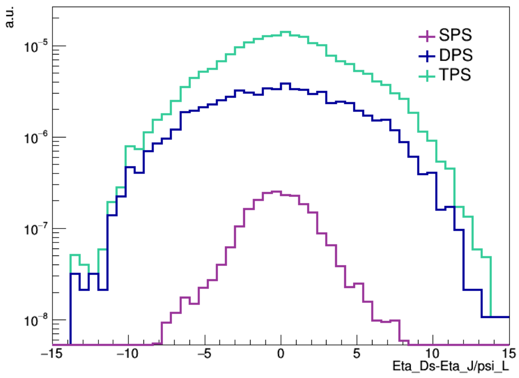

(c) $\Delta(\eta_{D^*} - \eta_{J/\psi_L})$ distribution.

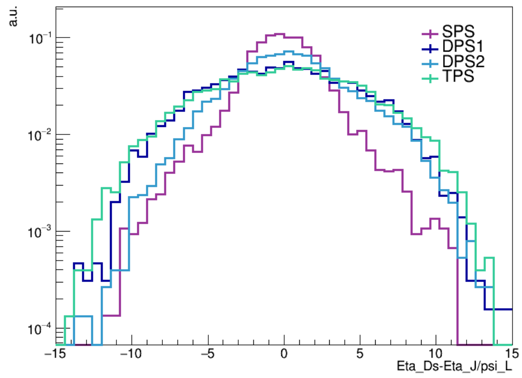

(d) $\Delta(\eta_{D^*} - \eta_{J/\psi_L})$ distribution.

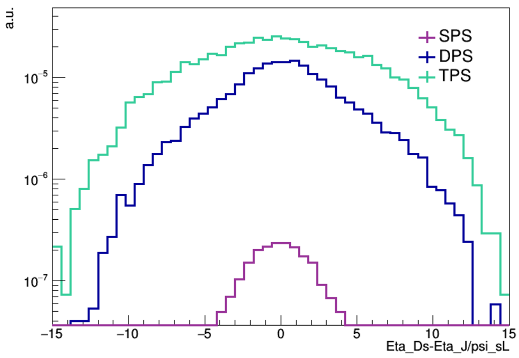

(e) $\Delta(\eta_{D^*} - \eta_{J/\psi_{sL}})$ distribution.

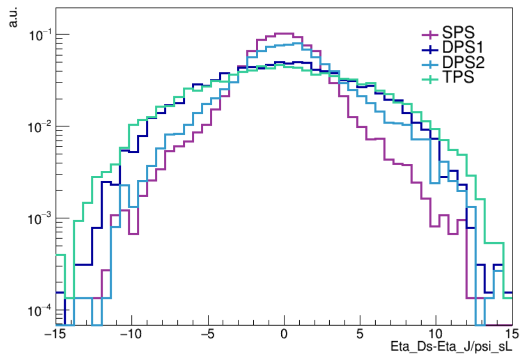

(f) $\Delta(\eta_{D^*} - \eta_{J/\psi_{sL}})$ distribution.

Figure 6.13: In figure 6.13a (6.13b) is shown$\Delta(\phi_{J/\psi_L} - \phi_{J/\psi_{sL}})$, meanwhile in figure 6.13c (6.13d), 6.13e (6.13f) are shown the $\Delta(\eta_{D^*} - \eta_{J/\psi_L})$ and $\Delta(\eta_{D^*} - \phi_{J/\eta_{sL}})$ distributions.

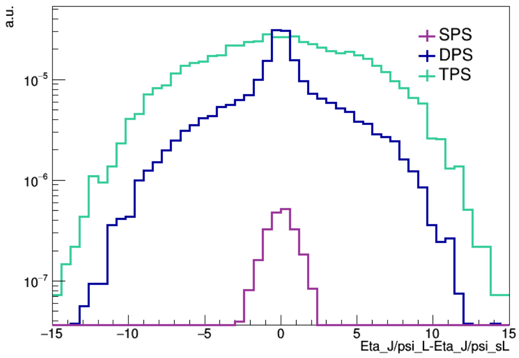

(a) $\Delta(\eta_{J/\psi_L} - \eta_{J/\psi_{sL}})$ distribution.

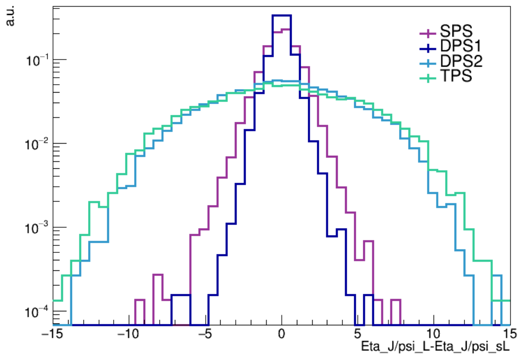

(b) $\Delta(\eta_{J/\psi_L} - \eta_{J/\psi_{sL}})$ distribution.

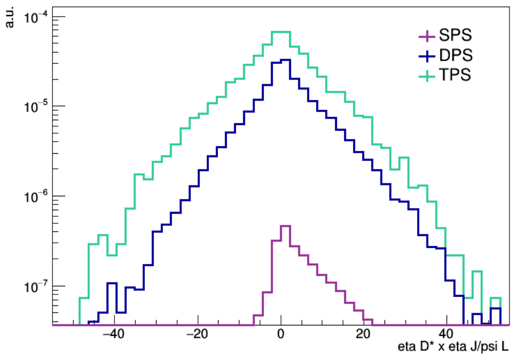

(c) $\eta_{D^*} \times \eta_{J/\psi_L}$ distribution.

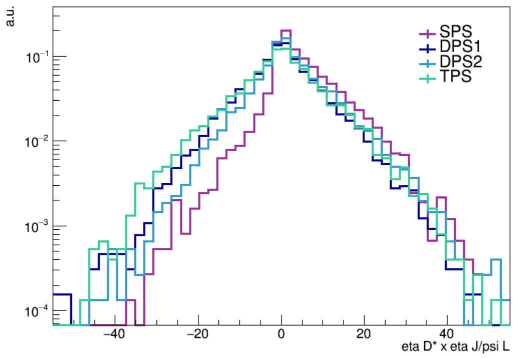

(d) $\eta_{D^*} \times \eta_{J/\psi_L}$ distribution.

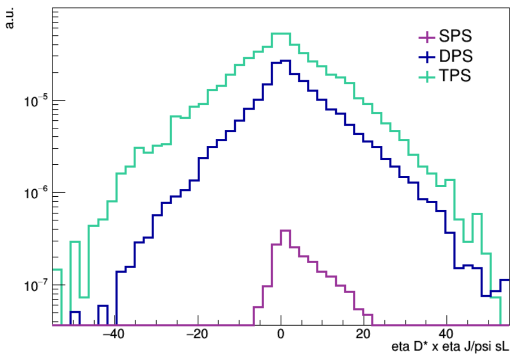

(e) $\eta_{D^*} \times \eta_{J/\psi_{SL}}$ distribution.

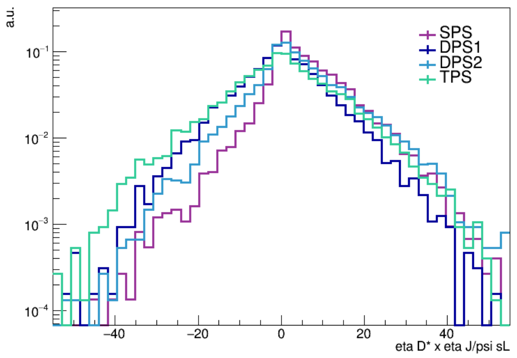

(f) $\eta_{D^*} \times \eta_{J/\psi_{SL}}$ distribution.

Figure 6.14: In figure 6.14a (6.14b), 6.14c (6.14d), 6.14e (6.14f) are shown, respectively, the $\Delta(\eta_{J/\psi_L} - \eta_{J/\psi_{sL}})$, $\eta_{D^*} \times \eta_{J/\psi_L}$ and $\eta_{D^*} \times \eta_{J/\psi_{sL}}$ distributions.

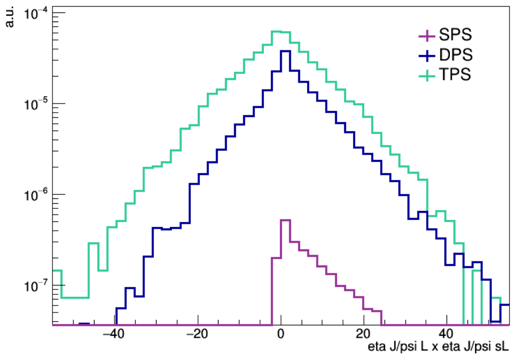

(a) $\eta_{J/\psi_L} \times \eta_{J/\psi_{sL}}$ distribution.

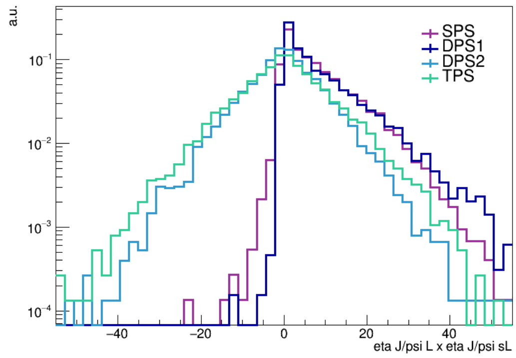

(b) $\eta_{J/\psi_L} \times \eta_{J/\psi_{sL}}$ distribution.

Figure 6.15: In figure 6.15a (6.15a) is shown the $\eta_{J/\psi_L} \times \eta_{J/\psi_{sL}}$ distribution.

These distributions are crucial from different points of view: on the one hand the different shapes of each contribute will play a key role when it will come to discriminate the signal and the background events, on the other hand these distributions are the direct results of the ansatzs that allow to write the pocket formula. The non correlation hypothesis are mirrored in these variables: the differences that may be present between the foreseen plots and the plots obtained from the data can suggest how large is the contribution from the neglected correlations.

As already anticipated from the previous graphs, the different kinematics between the events are emphasized by the correlation variables. Let's examine for example the graph 6.12b: here the difference between the two extreme case, namely the TPS and the SPS case, is well visible. For the former, since the SPS productions that converged in the pocket formula are considered independent, the distribution in space do not present any peculiar trend, on the contrary, the latter case presents a well defined trend, suggesting a correlation between the D^* and the J/ψ_L.

The same conclusions on the kinematic differences between the processes, can be drawn from the $\Delta\eta_{i,j}$ and $\eta_i \times \eta_j$: the distributions plotted in the graphs 6.14b and 6.15b suggest that the two J/ψ share the sign of the pseudorapidity in the SPS and DPS1 cases. Let's remind that the pseudorapidity is a commonly used spatial coordinate describing the angle of a particle relative to the beam axis; from here it follows that in these cases the charmonia are preferentially produce within the same polar angle since originating from the same parton parton interaction. This is also visible in figure 6.13b. This is not true for the DPS2 and TPS processes, and indeed the distribution is symmetric around zero.

6.3 Event reconstruction and cut selection

Since our detector covers only a limited fraction of the phase space, a pre-selection on the events that fall within the acceptance regions of CMS was necessary. This first selection also allowed a bare esteem on the detection efficiency for each sample. Bear in mind that the efficiency provided here is not the end result: the whole performance of each sub-detector should be taken into account. The detector performance is simulated in the so-called Simulation step (SIM), which follows the Generation Level step and was not implemented here, since is goes beyond the scope of this thesis.

The table 6.3 wants to illustrate the fiducial phase space; the cuts on the charmonia and the muons follow, as reference, the ones used in [61].

Particle	Variable acceptance
D^*	$p_T > 4$ (2) GeV for $\|\eta\| < 2.5$
J/ψ	$p_T > 6$ GeV for $\|\eta\| < 2.5$
D^0	$p_T > 3$ (1.5) GeV for $\|\eta\| < 2.5$
π_{slow}	$p_T > 0.3$ GeV for $\|\eta\| < 2.5$
π	$p_T > 0.7$ (0.5) GeV for $\|\eta\| < 2.5$
K	$p_T > 0.7$ (0.5) GeV for $\|\eta\| < 2.5$
μ	$p_T > 2.5$ GeV for $\|\eta\| < 2.5$

Table 6.3: Acceptance regions for mothers and daughters particles in terms of p_T and η.

The values before the brackets are the fiducial cuts that usually outline the acceptance region for the CMS detector, while the values in the brackets are refer to the cut here used for the analysis: these more inclusive cuts could be exploit in the future by optimizing the performance of the analysis reconstruction. The willingness to have a larger fiducial phase space region comes from the signal distributions, in fact, larger yields of TPS events seem to be concentrated in the low p_T region, which, unfortunately, is partially inaccessible and has a low efficiency.

At this point the events have been reconstructed without the use of the MC truth. Only for muons we used the PDG identity, that it is because when passing to a full analysis and working on the data, the muons are effectively recognized as such thanks to the muon chambers. In fact, the CMS experiment, by combining the tracker and the muon chambers information, can recognize the muon tracks with an high efficiency.

Charmonia reconstruction

The charmonia are reconstructed by the combination of the four most energetic muons: the final muons are initially identified as stable particles [82], then they are discriminated on the basis of their charge and finally sorted in energy descending order. The invariant masses of the four most energetic muons and anti-muons are then computed: the combinations which are closer to the PDG mass of the J/ψ pass the selection. In figure 6.16 the plot for the computed invariant mass is shown and a clear peak around 3.1 GeV is present, as expected for the J/ψ invariant mass; the background is combinatorial[1].

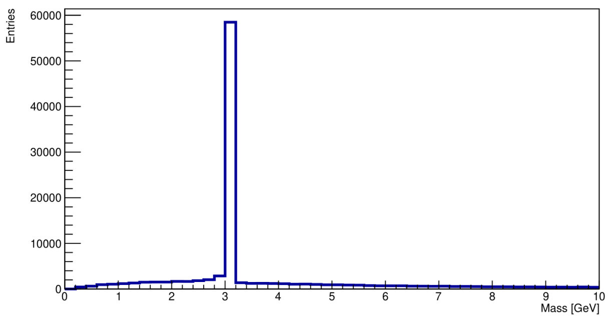

Figure 6.16: Invariant mass of all the possible couples between all the muons: the resonance is not centered in the true value of the J/ψ mass, that has been attributed to the fact that PYTHIA simulates the photon emission from the muons before reaching the final state muons, thus, to complete the picture the energy of the emitted photon must also be summed.

A diagram of the logic flux followed for the charmonia reconstruction is shown in figure 6.17.

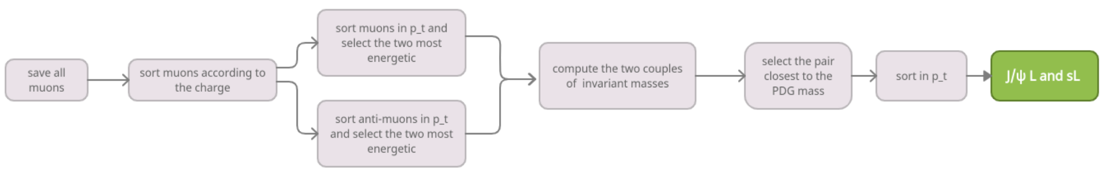

Figure 6.17: Logic flux followed for the charmonia reconstruction.

[1]Since there are no major differences between the four samples only one example of the invariant plot mass per combination is here reported.

D^* reconstruction

The reconstruction of the D^* meson required more steps: the first step is the D^0 meson reconstruction. While the D^* decays immediately, the D^0, which has a longer life time, decays in the tracker, opening to the possibility to reconstruct the Secondary Vertex. The kinematic information and the vertex of the charged particles present within the event are saved into a vector, then they are combined in pair, requiring that they both come from the same vertex and that their invariant mass is compatible with the D^0 mass. Another selection criterion is the cosine of the angle ($cos\alpha$) between the charm candidate momentum and the vector pointing from the Primary Vertex (production vertex) to the Secondary Vertex (decay vertex): if it is greater than 0.90, the charmed meson is likely to have been originated from the Primary Vertex. The value of the cosine has been choosen observing the cosine distribution from the Monte Carlo truth: here, since the detector simulation is missing, all the events are compatibly with $cos\alpha = 1$ because a complete superimposition between the two directions is satisfied. In order to compute the cosine, the information on the production vertex of the K or π candidate has been used as SV, meanwhile for the PV the information on the π_{slow} has been employed. The cosine formula reads:

$$cos\alpha = \frac{\vec{d} \cdot \vec{p}}{|d||p|}, \tag{6.1}$$

where $\vec{d}$ is the distance between the SV and PV and $\vec{p}$ is the three momentum of the D^0 candidate. The invariant mass using all the possible combination between the charged particles is shown in figure 6.18: for the combinatorial backgrounds three emerging picks are well visible, meanwhile the bumps in the combinatorial background are attributable to the presence of three resonances. The first and the second picks have been attributed to K^0, centred in ≈ 0.5 GeV and to Λ centred in ≈ 1.1 GeV. The pick centered in ≈ 1.9 is compatible with a D^0. Only the combinations that return an invariant mass of the D^0 nominal mass within 0.0001 GeV pass the selection. In this case a cut selection on the mass was mandatory because the D^*, in opposition to the J/ψ, is not present in each event, thus the closer invariant mass combination can be sensibly smaller or larger with respect to the D^* mass and this would falsify the selection.

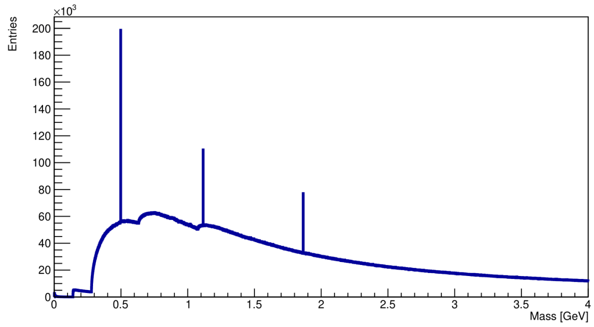

Figure 6.18: Invariant mass of all the possible couples between all the charged particle, muons excluded: the pick centered in the D^0 mass value is well visible (The higher). The other two resonances are attributed to K^0 (the lower) and to Λ (the central).

Once the D^0 candidates are reconstructed, the invariant mass of the D^0 plus the additional charge particle is computed: this is done by excluding the charged particles used for the D^0 reconstruction and all the muons. The invariant mass computed with the D^0 candidate and a third charged particle is shown in figure 6.19 and a clear peak around 2.1 GeV is shown, indicating the presence of the D^*. Afterward the candidates for the D^* are selected by requiring the compatibility between the computed invariant mass and the PDG mass within 0.001 GeV.

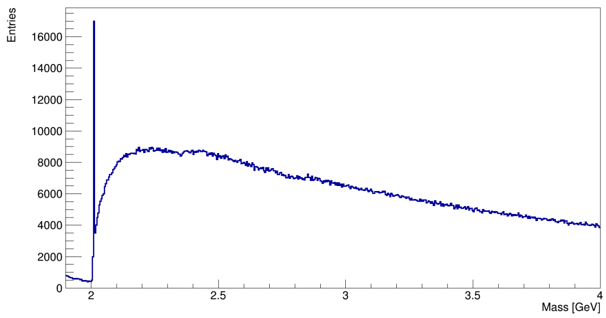

Figure 6.19: Invariant mass of all the possible combination between the D^0 candidate and the reaming charged particles, muons excluded: the pick centered in the D^* mass value is well visible.

A diagram of the logic flux followed for the D^* construction is shown in figure 6.20.

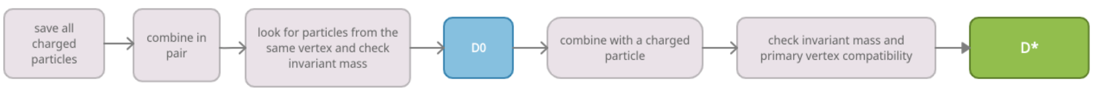

Figure 6.20: Logic flux followed for the D^* construction

6.4 First scenario: realistic situation

The first scenario that has been explored is the most realistic one where the cut selection is based on the fiducial region described in table 6.3.

In the TPS case, the sub-sub-sub-Leading and the sub-sub-Leading muons distributions are completely (or almost) under the p_T threshold (see figure 6.21 and 6.22). Hence, the small statistics does not allow to see the desired final state with the selected strategy, although an upper limit can be estimated.

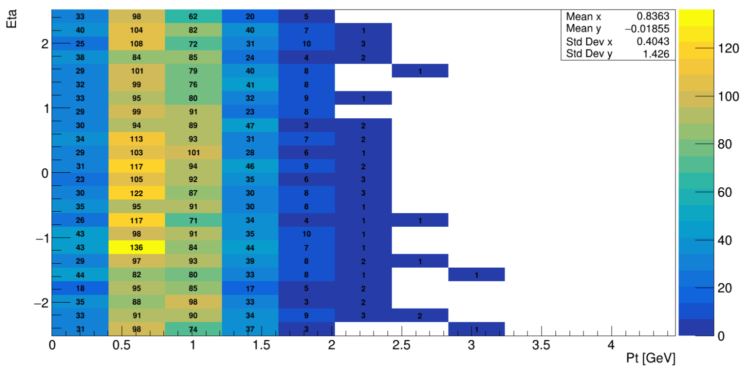

Figure 6.21: Scatter plot for the reconstructed μ_{sssL}: the range of the y axis (η) reflects the acceptance region, meanwhile the range of the x axis starts from zero to allow the reader to appreciate where the majority of the events are collocated. The numbers indicate the entries bin per bin.

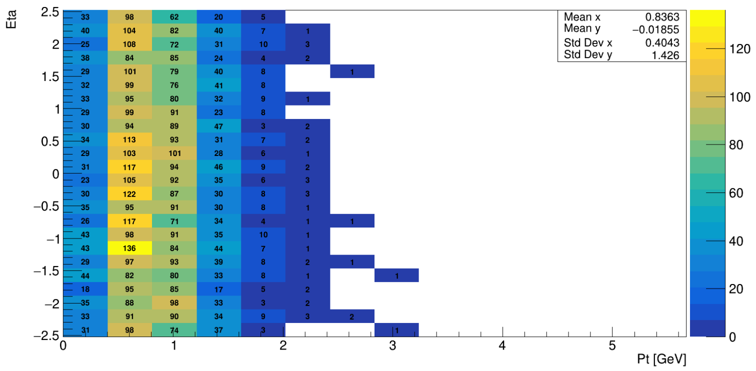

Figure 6.22: Scatter plot for the reconstructed μ_{ssL}: the range of the y axis (η) reflects the acceptance region, meanwhile the range of the x axis starts from zero to allow the reader to appreciate where the majority of the events are collocated. The numbers indicate the entries bin per bin.

The limits on the efficiency and the corresponding estimated number of events are reported in the table 6.4: the errors have been estimated assuming a Poisson distribution for the reconstructed events and propagating the error. The number of the events is computed using $N = \mathcal{L} \cdot \sigma \cdot \epsilon$, where $\mathcal{L}$ is the integrated luminosity, σ is the cross section and ϵ is the efficiency.

Process	Efficiency	Expected event at $138 fb^{-1}$
σ_{SPS}	$< (0.13 \pm 0.04)\%$	$< 0.012 \pm 0.004$
σ_{DPS}	$< (0.25 \pm 0.04)\%$	$< 45 \pm 7$
σ_{TPS}	$< (0.01 \pm 0.01)\%$	$< 3 \pm 3$

Table 6.4: Efficiency and expected events in a realistic scenario.

We expect that the region over the p_T threshold for the muons is poorly populated for a statistical effect, thereby, increasing the initial statistics can open the possibility to have soft muons over the selected threshold and improve the efficiency.

6.5 Second scenario: ideal situation

As observed during the analysis, the selected reconstruction strategy may not be optimized. The less energetic muons ($sssL$ and ssL) may not have the sufficient transverse momentum to be detected from, at least, the first muon chamber. In this case, depending on what will emerge from a deeper Monte Carlo study, the $sssL$ and ssL could be identified by the *Soft Muons ID* selection as *track muons*. In this case the muon is a tracker muon with a tracker track that satisfies a high purity flag and uses hits from at least six layers of the inner tracker including at least one pixel hit. The tracker muon reconstruction must have tight segment matching, having pulls less than 3 both in local x and in local y. A soft muon is loosely compatible with the primary vertex, having $|d_{xy}| < 0.3$ cm and $|dz| < 20$ cm [88], where d_{xy} and dz are the relative distances from the PV.

In this scenario the p_T threshold for the two softer muons is lowered to 1 GeV. The novel fiducial cuts are reported in table 6.5.

Particle	Variable acceptance
π_{slow}	$p_T > 0.3$ GeV for $\lvert\eta\rvert < 2.5$
π	$p_T > 0.7$ (0.5) GeV for $\lvert\eta\rvert < 2.5$
K	$p_T > 0.7$ (0.5) GeV for $\lvert\eta\rvert < 2.5$
μ_L and μ_{sL}	$p_T > 2.5$ GeV for $\lvert\eta\rvert < 2.5$
μ_{ssL} and μ_{sssL}	$p_T > 1$ GeV for $\lvert\eta\rvert < 2.5$

Table 6.5: Acceptance regions for daughters particles in terms of p_T and η.

For the present case the efficiency and estimated events are reported in table 6.6: the errors have been estimated assuming a Poisson distribution for the reconstructed events and propagating the error. The number of the events is computed using $N = \mathcal{L} \cdot \sigma \cdot \epsilon$, where $\mathcal{L}$ is the integrated luminosity, σ is the cross section and ϵ is the efficiency.

Process	Efficiency	Expected event at $138 fb^{-1}$
σ_{SPS}	$(1.89 \pm 0.16)\%$	0.30 ± 0.03
σ_{DPS}	$(1.06 \pm 0.09)\%$	191 ± 16
σ_{TPS}	$(0.27 \pm 0.01)\%$	81 ± 3

Table 6.6: Efficiency and expected events in an ideal scenario.

In both scenarios the DPS signal is estimated to be the main background, suggesting that this study is propedeutic not only for the TPS case, but also for the DPS productions.

Chapter 7

Conclusions

This thesis wanted to encourage the study of a novel final state in the charmed sector to probe the Triple Parton Scattering.

The first aim was to explore the possibility of employing the HELAC-Onia, a Matrix Element generator in the framework of NRQCD, to produce the initial SPS samples and elaborate an efficient strategy to reproduce the DPS and TPS samples. The production of the samples required a deep study of both generators (HELAC-Onia and PYTHIA), as well as the LHEF structure and its interpretation.

The second goal was to give a cross-section evaluation for the production of two J/ψ plus a D^* meson and characterize the kinematics and correlation variables for the three cases (SPS, DPS and TPS). What emerged from this second point is that the correlation variables might play a key role in discerning the different contributes. In a future perspective, the application of machine learning techniques will exploit such features for the enhancing of signal.

Another point that has emerged concerns the magnitude of the initial samples: in order to have a more reliable prediction on the expected signal and the SPS and DPS backgrounds events, a large statistics is needed. Nevertheless the obtained results seem to be in accordance with the results of the triple J/ψ observation [61]. The hierarchy between the SPS, DPS and TPS, with due distinctions, are in the two cases comparable: the SPS background is foreseen to be negligible, while the DPS represents the main background that can mimic the signal. A direct comparison of the cross sections here reported and the ones described in [61] is not possible, since in the latter case they have been estimated taking in to account the fiducial phase space always reported in [61].

Let us foresee the cross section for the DPS and TPS case for a final state with three J/ψ using the SPS cross section of a single charmonium reported in 6.2. The SPS case is neglected for the above mentioned reason.

Process	$J/\psi + J/\psi + D^*$ (mb)	$J/\psi + J/\psi + J/\psi$ (mb)
σ_{DPS}	0.35×10^{-4}	0.11×10^{-4}
σ_{TPS}	0.55×10^{-3}	0.06×10^{-5}

Table 7.1: The DPS and TPS cross sections calculated using the pocket formula and the expected events in a final state with $J/\psi + J/\psi + D^*$ compered to a final state with $J/\psi + J/\psi + J/\psi$.

The results reported in table 7.1 seem to validate the main motivation behind this thesis, even considering the fiducial efficiencies calculated in the previous chapter: a final state with an open charm mesons and two charmonia might be a good probe for the study of the Triple Parton Scattering.

7.1 What is next

In order to elevate this preliminary study to a full analysis, at least three steps are necessary:

- The first step aims to increase the precision of the MC predictions and to enlarging the statistics.
- The second step will be the validation for the reconstruction strategy.
- The third and last step will be the data analysis of Run II and Run III (once the first data will be available).

The samples used in this thesis are at the Leading-Order (LO), namely the leading term in a series expansion; adding the NLO terms means to retain the set of next largest terms in the expansion. Hence, to fulfill the first step's goals, all the processes should be studied at Next-to-Leading-Order, and this might mean to introduce a third generator (MadGraph5aMC@NLO), to improve the prediction. On the other hand to complement the sample generation, the colour octet contributions should be included; the colour octet contributions, neglected in this thesis, are believed to give a non marginal contribution at large p_T that may be crucial for this work, as shown in the previous chapter. Finally, also the so-called 4-flavour scheme should be taken into account, which will mean to include the following processes:

$$g\ c\bar{c} \rightarrow J/\psi + J/\psi + c\bar{c} \tag{7.1}$$

$$c\bar{c}\ g \rightarrow J/\psi + J/\psi + c\bar{c}; \tag{7.2}$$

these processes might have a non negligible contribution in the generation; here only the gluons-gluons interactions were considered, as the dominant one.

The consequential step is the analysis strategy validation, which will follow a new characterization of the MC distributions. Once the distributions have been characterized at the MC level, one has to take into account all the possible background processes; in fact, the QCD processes at LHC are foreseen to dominate with respect to the SPS and DPS contributes; the soft (non perturbative) contribution from MPI and the beam remnants can also play a key role. The Pile Up is another aspect to investigate: in a scenario like the Run II or Run III, where the luminosity is high, and several proton-proton collision can take place simultaneously, there will be a plethora of events that can mimic the signal. The main challenge will be to correctly reconstruct the interaction vertices: larger is the PU, greater is the probability to merge two independent vertices for being too close. Hence, to summarize, there are three main contributes that are foreseen to dominate the signal: the QCD background which comprehend all the final state identical to the signal one, but produced from different mechanisms, the soft hadronic background (beams remnants and soft MPI interactions) and at last the Pile Up. Advanced Machine Learning technique may provide a crucial help in keeping signal well identified over all these background sources, using the key correlation variables already presented in this thesis, and possibly more.

In addition, at this point taking the simulation of the entire detector into account is mandatory: this will allow to obtain a realistic perspective on the reconstruction efficiency and to elaborate the best strategy to follow in order to optimize the signal reconstruction.

Should there be the possibility, the last step will be the full analysis of Run II and of the ongoing Run III, which is expected to reach an integrated luminosity of at least 150 fb^{-1} by 2025.

Appendix A

TPS: event block example

In figure is show an example of a part of a TPS event block.


```
<event>
714 9999 1.000000 3.234066 0.007299 0.118000
21 -1 5 5 103 101 0.000000 0.000000 13.500496 13.500496 0.000000 0.000000 9.000000
21 -1 6 0 101 102 0.000000 0.000000 -0.469112 0.469112 0.000000 0.000000 9.000000
4 2 1 2 103 0 -1.217969 1.485648 8.254867 8.607173 1.500000 0.000000 9.000000
-4 2 1 2 0 102 1.217969 -1.485648 4.776517 5.362435 1.500000 0.000000 9.000000
21 2 16 0 103 101 -0.000000 -0.000000 13.500496 13.500496 0.000000 0.000000 9.000000
21 2 17 17 101 104 -0.000000 0.000000 -42.631416 42.631416 0.000000 0.000000 9.000000
4 2 3 3 103 0 -0.716539 2.022805 8.234060 8.640307 1.500000 0.000000 9.000000
-4 2 4 4 0 102 2.051894 -0.592307 4.702753 5.378381 1.500000 0.000000 9.000000
21 2 6 0 102 104 -1.335355 -1.430498 -42.067733 42.113224 0.000000 0.000000 9.000000
21 2 9 0 105 104 -0.510841 -1.461893 -40.116398 40.146276 0.000000 0.000000 9.000000
21 2 9 0 102 105 -0.794776 0.022951 -1.880183 2.041393 0.000000 0.000000 9.000000
-4 2 8 8 0 102 2.022156 -0.583862 4.631601 5.303937 1.500000 0.000000 9.000000
21 2 11 0 106 105 -0.429775 0.180580 -1.910891 1.966931 0.000000 0.000000 9.000000
21 2 11 0 102 106 -0.158774 -0.214912 0.503709 0.570193 0.000000 0.000000 9.000000
-4 2 12 12 0 102 1.815930 -0.526579 4.158600 4.808205 1.500000 0.000000 9.000000
21 2 24 24 108 101 0.000000 0.000000 99.793318 99.793318 0.000000 0.000000 9.000000
21 2 25 25 101 104 0.000000 -0.000000 -42.631416 42.631416 0.000000 0.000000 9.000000
4 2 7 7 103 0 -0.405976 1.967025 8.252088 8.624439 1.500000 0.000000 9.000000
-4 2 15 15 0 102 1.980959 -0.556220 4.122491 4.845463 1.500000 0.000000 9.000000
21 2 10 10 105 104 -0.510292 -1.461992 -40.106695 40.136576 0.000000 0.000000 9.000000
21 2 13 13 106 105 -0.428744 0.180395 -1.902143 1.958191 0.000000 0.000000 9.000000
21 2 14 14 102 106 -0.139010 -0.218462 0.505806 0.568233 0.000000 0.000000 9.000000
21 2 16 0 108 103 -0.496938 0.089255 86.290354 86.291831 0.000000 0.000000 9.000000
21 2 0 0 108 101 -0.326416 -0.267903 99.793429 99.794323 0.000000 0.000000 9.000000
21 2 0 0 101 104 -0.225652 -0.663001 -42.629561 42.635313 0.000000 0.000000 9.000000
4 2 18 18 103 0 -0.434530 1.941511 8.239861 8.608344 1.500000 0.000000 9.000000
-4 2 19 19 0 102 1.964386 -0.573863 4.124087 4.842130 1.500000 0.000000 9.000000
21 2 20 20 105 104 -0.722739 -2.086039 -40.095026 40.155760 0.000000 0.000000 9.000000
21 2 21 21 106 105 -0.439052 0.150300 -1.902786 1.958559 0.000000 0.000000 9.000000
21 2 22 22 102 106 -0.140937 -0.220396 0.507354 0.570829 0.000000 0.000000 9.000000
21 2 23 23 108 103 -0.779196 -0.142417 86.290379 86.294015 0.000000 0.000000 9.000000
2103 2 0 0 0 108 0.377902 0.375994 4611.015671 4611.015766 0.771330 0.000000 9.000000
2 2 0 0 101 0 -0.051486 -0.108091 1788.943215 1788.943250 0.330000 0.000000 9.000000
2 2 0 0 104 0 0.294510 0.321111 -0.061466 0.550024 0.330000 0.000000 9.000000
2101 2 0 0 0 101 -0.068858 0.341890 -6457.061288 6457.061324 0.579330 0.000000 9.000000
-4 2 27 30 0 106 1.823449 -0.794258 4.631441 5.412959 1.973338 0.000000 9.000000
2 2 34 34 104 0 0.294510 0.321111 -0.061466 0.550024 0.330000 0.000000 9.000000
21 2 28 28 105 104 -0.722739 -2.086039 -40.095026 40.155760 0.000000 0.000000 9.000000
21 2 29 29 106 105 -0.439052 0.150300 -1.902786 1.958559 0.000000 0.000000 9.000000
-4 2 36 36 0 106 1.823449 -0.794258 4.631441 5.412959 1.973338 0.000000 9.000000
321 1 37 40 0 0 -0.131799 0.048075 -1.189432 1.295435 0.493680 2302.461000 9.000000
-323 2 37 40 0 0 0.184567 0.293804 -1.572909 1.845344 0.900481 0.000000 9.000000
211 1 37 40 0 0 0.243965 -0.515874 -7.001176 7.025781 0.139570 4656.881000 9.000000
-211 1 37 40 0 0 -0.532951 -0.637377 -4.840311 4.913083 0.139570 11109.410000 9.000000
211 1 37 40 0 0 -0.061597 0.186731 -5.979400 5.984260 0.139570 5581.863000 9.000000
111 2 37 40 0 0 -0.514814 -0.044567 -0.834667 0.990913 0.134980 0.000016 9.000000
113 2 37 40 0 0 0.193910 -1.286641 -17.849467 17.916058 0.829815 0.000000 9.000000
111 2 37 40 0 0 0.008543 0.139591 -1.535738 1.547989 0.134980 0.000008 9.000000
311 2 37 40 0 0 -0.010859 0.206012 0.001161 0.538680 0.497610 0.000001 9.000000
-321 1 37 40 0 0 -0.317558 -0.198268 -0.780109 0.996214 0.493680 3562.610000 9.000000
-423 2 37 40 0 0 1.894761 -0.600373 4.154212 5.023545 2.006980 0.000000 9.000000
4 2 26 26 103 0 -0.434530 1.941511 8.239861 8.608344 1.500000 0.000000 9.000000
[...]
</event>
```


Figure A.1: Event block for a TPS event.

Bibliography

[1] CMS Collaboration et al. "Measurement of double-parton scattering in inclusive production of four jets with low transverse momentum in proton-proton collisions at $\sqrt{s} = 13$ TeV". In: *arXiv preprint arXiv:2109.13822* (2021).

[2] CMS collaboration et al. "Commissioning and performance of the CMS pixel tracker with cosmic ray muons". In: *Journal of Instrumentation* 5.03 (2010), T03007.

[3] Hua-Sheng Shao. "HELAC-Onia: an automatic matrix element generator for heavy quarkonium physics". In: *Computer Physics Communications* 184.11 (2013), pp. 2562–2570.

[4] Hua-Sheng Shao. "HELAC-Onia 2.0: an upgraded matrix-element and event generator for heavy quarkonium physics". In: *Computer Physics Communications* 198 (2016), pp. 238–259.

[5] Torbjörn Sjöstrand et al. "An introduction to PYTHIA 8.2". In: *Computer physics communications* 191 (2015), pp. 159–177.

[6] Thomas Sven Pettersson and P Lefèvre. *The Large Hadron Collider: conceptual design*. Tech. rep. Oct. 1995. URL: `https://cds.cern.ch/record/291782`.

[7] F. Halzen, A. D. Martin, and D. M. Scott. "Identification of W bosons in $\bar{p}p$ collisions: A detailed study". In: *Phys. Rev. D* 25 (3 Feb. 1982), pp. 754–760. DOI: `10.1103/PhysRevD.25.754`. URL: `https://link.aps.org/doi/10.1103/PhysRevD.25.754`.

[8] G. Arnison et al. "Experimental Observation of Isolated Large Transverse Energy Electrons with Associated Missing Energy at $\sqrt{s} = 540$ GeV". In: *Phys. Lett. B* 122 (1983), pp. 103–116. DOI: `10.1016/0370-2693(83)91177-2`.

[9] G. Arnison et al. "Experimental observation of lepton pairs of invariant mass around 95 GeV/c2 at the CERN SPS collider". In: *Physics Letters B* 126.5 (1983), pp. 398–410. ISSN: 0370-2693. DOI: `https://doi.org/10.1016/0370-2693(83)90188-0`. URL: `https://www.sciencedirect.com/science/article/pii/0370269383901880`.

[10] Giorgio Brianti. "The large hadron collider project: historical account". In: *Physics reports* 403 (2004), pp. 349–364.

[11] Luciano Maiani and Luisa Bonolis. "The LHC Timeline: A personal recollection (1980-2012). Oral History Interview". In: *arXiv preprint arXiv:1705.04951* (2017).

[12] Stephen Myers. "The large hadron collider 2008–2013". In: *International Journal of Modern Physics A* 28.25 (2013), p. 1330035.

[13] JT Boyd. "LHC Run-2 and future prospects". In: *arXiv preprint arXiv:2001.04370* (2020).

[14] O Brüning, H Burkhardt, and S Myers. "The large hadron collider". In: *Progress in Particle and Nuclear Physics* 67.3 (2012), pp. 705–734.

[15] Georges Aad et al. "The ATLAS experiment at the CERN large hadron collider". In: *Journal of instrumentation* 3.S08003 (2008).

[16] Serguei Chatrchyan et al. "The CMS experiment at the CERN LHC". In: *Journal of instrumentation* 3.8 (2008), S08004.

[17] Kenneth Aamodt et al. "The ALICE experiment at the CERN LHC". In: *Journal of Instrumentation* 3.08 (2008), S08002.

[18] LHCb Collaboration et al. "The LHCb detector at the LHC". In: *Journal of instrumentation* 3.08 (2008), S08005–S08005.

[19] Lyndon R Evans. *THE LARGE HADRON COLLIDER PROJECT*.

[20] Valentina Mariani. *Open charm cross section measurement with the CMS tracker at* $\sqrt{13}$ *TeV*. Doctoral thesis, 2019.

[21] Thomas Kramer. "LHC Beam Dump System: Analysis of beam commissioning, performance and the consequences of abnormal operation". PhD thesis. TU Graz, 2011.

[22] Oliver Brüning et al. "The scientific potential and technological challenges of the High-Luminosity Large Hadron Collider program". In: *Reports on Progress in Physics* 85.4 (Mar. 2022), p. 046201. DOI: 10.1088/1361-6633/ac5106. URL: https://doi.org/10.1088/1361-6633/ac5106.

[23] Jorg Wenninger. "LHC status and performance". In: *PoS* CHARGED2018 (2019), p. 001. DOI: 10.22323/1.339.0001.

[24] A Alici et al. "The LHC machine and experiments". In: (2021), 12 p. DOI: 10.23731/CYRM-2021-001.23. URL: https://cds.cern.ch/record/2773265.

[25] Steven D Bass, Albert De Roeck, and Marumi Kado. "The Higgs boson implications and prospects for future discoveries". In: *Nature Reviews Physics* 3.9 (2021), pp. 608–624.

[26] Jan Kretzschmar. *Standard Model physics at the LHC*. 2018. DOI: 10.48550/ARXIV.1803.10800. URL: https://arxiv.org/abs/1803.10800.

[27] CMS Collaboration. "Observation of a new boson at a mass of 125 GeV with the CMS experiment at the LHC". In: *Physics Letters B* 716.1 (2012), pp. 30–61. ISSN: 0370-2693. DOI: https://doi.org/10.1016/j.physletb.2012.08.021. URL: https://www.sciencedirect.com/science/article/pii/S0370269312008581.

[28] Vardan Khachatryan et al. "Observation of the rare B_s^ 0→ μ+ μ- decay from the combined analysis of CMS and LHCb data". In: *Nature* 522.7554 (2015), pp. 68–72.

[29] Michelangelo Mangano. "LHC at 10: the physics legacy". In: *arXiv preprint arXiv:2003.05976* (2020).

[30] Burkhard Schmidt. "The High-Luminosity upgrade of the LHC: Physics and Technology Challenges for the Accelerator and the Experiments". In: *Journal of Physics: Conference Series* 706 (Apr. 2016), p. 022002. DOI: 10.1088/1742-6596/706/2/022002. URL: https://doi.org/10.1088/1742-6596/706/2/022002.

[31] John Apostolakis et al. "Detector simulation challenges for future accelerator experiments". In: ().

[32] The CMS Collaboration. "The CMS experiment at the CERN LHC". In: *Journal of Instrumentation* 3.08 (Aug. 2008), S08004–S08004. DOI: 10.1088/1748-0221/3/08/s08004. URL: https://doi.org/10.1088/1748-0221/3/08/s08004.

[33] W. Adam et al. In: 16.02 (Feb. 2021), P02027–P02027. DOI: 10.1088/1748-0221/16/02/p02027. URL: https://doi.org/10.1088/1748-0221/16/02/p02027.

[34] Katja Klein. "The CMS Silicon Strip Tracker-Overview and Status". In: *arXiv preprint physics/0610259* (2006).

[35] Serguei Chatrchyan et al. "CMS Collaboration". In: *Nuclear Physics A* 932 (2014), pp. 595–620.

[36] Mark Raymond et al. "The APV25 0.25/spl mu/m CMOS readout chip for the CMS tracker". In: *2000 IEEE Nuclear Science Symposium. Conference Record (Cat. No. 00CH37149)*. Vol. 2. IEEE. 2000, pp. 9–113.

[37] Cristina Biino. "The CMS Electromagnetic Calorimeter: overview, lessons learned during Run 1 and future projections". In: *Journal of Physics: Conference Series*. Vol. 587. 1. IOP Publishing. 2015, p. 012001.

[38] Vyacheslav Klyukhin. "Design and Description of the CMS Magnetic System Model". In: *Symmetry* 13.6 (2021). ISSN: 2073-8994. DOI: 10.3390/sym13061052. URL: https://www.mdpi.com/2073-8994/13/6/1052.

[39] A.M. Sirunyan et al. "Performance of the CMS muon detector and muon reconstruction with proton-proton collisions at $\sqrt{s} = 13$ TeV". In: *Journal of Instrumentation* 13.06 (June 2018), P06015–P06015. DOI: 10.1088/1748-0221/13/06/p06015.

[40] CMS collaboration et al. "The performance of the CMS muon detector in proton-proton collisions at $\sqrt{s} = 7$ TeV at the LHC". In: *Journal of Instrumentation* 8.11 (2013), P11002.

[41] CMS collaboration et al. "The CMS trigger system". In: *arXiv preprint arXiv:1609.02366* (2016).

[42] G Bauer et al. "The data-acquisition system of the CMS experiment at the LHC". In: *Journal of Physics: Conference Series*. Vol. 331. 2. IOP Publishing. 2011, p. 022021.

[43] Lorenzo Viliani, CMS Collaboration, et al. "CMS tracker performance and readiness for LHC Run II". In: *Nuclear Instruments and Methods in Physics Research Section A: Accelerators, Spectrometers, Detectors and Associated Equipment* 824 (2016), pp. 67–69.

[44] Anne Dabrowski. "Upgrade of the CMS Instrumentation for luminosity and machine induced background measurements". In: *Nuclear and Particle Physics Proceedings* 273-275 (2016). 37th International Conference on High Energy Physics (ICHEP), pp. 1147–1154. ISSN: 2405-6014. DOI: https://doi.org/10.1016/j.nuclphysbps.2015.09.180. URL: https://www.sciencedirect.com/science/article/pii/S2405601415006690.

[45] Giovanni Abbiendi. "The CMS muon system in Run2: preparation, status and first results". In: *arXiv preprint arXiv:1510.05424* (2015).

[46] Josef Sestak et al. "Upgrade of the CMS Experimental Beam Vacuum During LS2". In: *9th Int. Particle Accelerator Conf.(IPAC'18), Vancouver, BC, Canada, April 29-May 4, 2018*. JACOW Publishing, Geneva, Switzerland. 2018, pp. 2596–2599.

[47] Gautier Hamel de Monchenault. "SISSA: Highlights and perspectives from the CMS experiment". In: *PoS* (2021), p. 333.

[48] A. M. Sirunyan and Tumasyan. "Observation of the $\chi_{b1}(3P)$ and $\chi_{b2}(3P)$ and Measurement of their Masses". In: *Phys. Rev. Lett.* 121 (9 Aug. 2018), p. 092002. DOI: 10.1103/PhysRevLett.121.092002. URL: https://link.aps.org/doi/10.1103/PhysRevLett.121.092002.

[49] Albert M Sirunyan et al. "Observation of the $Z \to J/\psi l^+ l^-$ Decay in pp Collisions at $\sqrt{s} = 13$TeV". In: *Physical Review Letters* 121.14 (2018), p. 141801.

[50] Michael Riordan. "The Discovery of Quarks". In: *Annalen der Physik* (1992).

[51] Alessandro Bettini. *Introduction to elementary particle Physics*. Cambridge University Press, 2008. ISBN: 9780511398759.

[52] Richard P. Feynman. "Very High-Energy Collisions of Hadrons". In: *Phys. Rev. Lett.* 23 (24 Dec. 1969), pp. 1415–1417. DOI: 10.1103/PhysRevLett.23.1415. URL: https://link.aps.org/doi/10.1103/PhysRevLett.23.1415.

[53] Richard D Ball et al. "Parton distributions from high-precision collider data". In: *The European Physical Journal C* 77.10 (2017), pp. 1–75.

[54] M Adamus and T Gadaj. "The ZEUS Experiment at DESY". In: (2000).

[55] I Abt et al. "The H1 detector at HERA". In: *Nuclear Instruments and Methods in Physics Research Section A: Accelerators, Spectrometers, Detectors and Associated Equipment* 386.2-3 (1997), pp. 310–347.

[56] Halina Abramowicz and Allen C Caldwell. "HERA collider physics". In: *Reviews of Modern Physics* 71.5 (1999), p. 1275.

[57] Paolo Bartalini and Jonathan Richard Gaunt. *Multiple parton interactions at the LHC*. Advanced series on directions in high energy physics. Singapore: World Scientific, 2019. DOI: 10.1142/10646. URL: https://cds.cern.ch/record/2621643.

[58] Oleh Fedkevych and Anna Kulesza. "Double parton scattering in four-jet production in proton-proton collisions at the LHC". In: *Phys. Rev. D* 104 (5 Sept. 2021), p. 054021. DOI: 10.1103/PhysRevD.104.054021. URL: https://link.aps.org/doi/10.1103/PhysRevD.104.054021.

[59] Ivan Belyaev and Daria Savrina. “Study of double parton scattering processes with heavy quarks”. In: *Multiple Parton Interactions At The Lhc*. World Scientific, 2019, pp. 141–157.

[60] P Bartalini et al. “Multi-parton interactions at the LHC”. In: *arXiv preprint arXiv:1111.0469* (2011).

[61] CMS Collaboration et al. “Observation of triple J/ψ meson production in proton-proton collisions at $\sqrt{s} = 13$ TeV”. In: *arXiv preprint arXiv:2111.05370* (2021).

[62] Marta Łuszczak, Rafał Maciuła, and Antoni Szczurek. “Production of two $c\bar{c}$ pairs in double-parton scattering”. In: *Physical Review D* 85.9 (May 2012). ISSN: 1550-2368. DOI: 10.1103/physrevd.85.094034. URL: http://dx.doi.org/10.1103/PhysRevD.85.094034.

[63] Andreas van Hameren, Rafał Maciuła, and Antoni Szczurek. “Single-parton scattering versus double-parton scattering in the production of two $c\bar{c}$ pairs and charmed meson correlations at the LHC”. In: *Phys. Rev. D* 89 (9 May 2014), p. 094019. DOI: 10.1103/PhysRevD.89.094019. URL: https://link.aps.org/doi/10.1103/PhysRevD.89.094019.

[64] R. Maciuła, A. van Hameren, and A. Szczurek. “Charm Meson Production and Double Parton Interactions at the LHC”. In: *Acta Physica Polonica B* 45.7 (2014), p. 1493. ISSN: 1509-5770. DOI: 10.5506/aphyspolb.45.1493. URL: http://dx.doi.org/10.5506/APhysPolB.45.1493.

[65] CMS Collaboration et al. “Measurements of Z bosons plus jets using variables sensitive to double parton scattering in pp collisions at 13 TeV”. In: *arXiv preprint arXiv:2105.14511* (2021).

[66] CMS Collaboration et al. “Observation of same-sign WW production from double parton scattering in proton-proton collisions at *sqrts*= 13 TeV”. In: *arXiv preprint arXiv:2206.02681* (2022).

[67] “Observation of WW from double-parton scattering in proton-proton collisions at $\sqrt{s} = 13$ TeV”. In: (2022).

[68] Jean-Philippe Lansberg, Hua-Sheng Shao, and Nodoka Yamanaka. “Indication for double parton scatterings in W+ prompt J/ψ production at the LHC”. In: *Physics Letters B* 781 (2018), pp. 485–491.

[69] Rafal Maciula and Antoni Szczurek. “Triple parton scattering effects in D-meson production at the LHC”. In: *arXiv preprint arXiv:1710.11521* (2017).

[70] Rafał Maciuła and Antoni Szczurek. “Can the triple-parton scattering be observed in open charm meson production at the LHC?” In: *Physics Letters B* 772 (2017), pp. 849–853. ISSN: 0370-2693. DOI: https://doi.org/10.1016/j.physletb.2017.07.061. URL: https://www.sciencedirect.com/science/article/pii/S0370269317306172.

[71] David d’Enterria and A. Snigirev. “Triple Parton Scatterings in High-Energy Proton-Proton Collisions”. In: *Physical Review Letters* 118 (Dec. 2016). DOI: 10.1103/PhysRevLett.118.122001.

[72] S. L. Glashow, J. Iliopoulos, and L. Maiani. “Weak Interactions with Lepton-Hadron Symmetry”. In: *Phys. Rev. D* 2 (7 Oct. 1970), pp. 1285–1292. DOI: 10.1103/PhysRevD.2.1285. URL: https://link.aps.org/doi/10.1103/PhysRevD.2.1285.

[73] J. -E. Augustin et al. “Discovery of a Narrow Resonance in e^+e^- Annihilation”. In: *Phys. Rev. Lett.* 33 (23 Dec. 1974), pp. 1406–1408. DOI: 10.1103/PhysRevLett.33.1406. URL: https://link.aps.org/doi/10.1103/PhysRevLett.33.1406.

[74] J. J. Aubert et al. “Experimental Observation of a Heavy Particle J”. In: *Phys. Rev. Lett.* 33 (23 Dec. 1974), pp. 1404–1406. DOI: 10.1103/PhysRevLett.33.1404. URL: https://link.aps.org/doi/10.1103/PhysRevLett.33.1404.

[75] Miguel Ángel Carretero Sahuquillo. “The charm quark as a naturalness success”. In: *Studies in History and Philosophy of Science Part B: Studies in History and Philosophy of Modern Physics* 68 (2019), pp. 51–61.

[76] Albert M Sirunyan et al. “Measurement of charged pion, kaon, and proton production in proton-proton collisions at s= 13 TeV”. In: *Physical Review D* 96.11 (2017), p. 112003.

[77] Johan Alwall et al. “A standard format for Les Houches event files”. In: *Computer Physics Communications* 176.4 (2007), pp. 300–304.

[78] Hua-Sheng Shao. personal communication. 2022.

[79] J. Pumplin et al. "New generation of parton distributions with uncertainties from global QCD analysis". In: *JHEP* 07 (2002), p. 012. DOI: 10.1088/1126-6708/2002/07/012. arXiv: hep-ph/0201195.

[80] Mykhailo Lisovyi, Andrii Verbytskyi, and Oleksandr Zenaiev. "Combined analysis of charm-quark fragmentation-fraction measurements". In: *The European Physical Journal C* 76.7 (2016), pp. 1–15.

[81] E Boos et al. "Generic user process interface for event generators". In: *arXiv preprint hep-ph/0109068* (2001).

[82] Christian Bierlich et al. "A comprehensive guide to the physics and usage of PYTHIA 8.3". In: *arXiv preprint arXiv:2203.11601* (2022).

[83] Lukas Heinrich, Matthew Feickert, and Eduardo Rodrigues. *pylhe: v0.3.0.* Version v0.3.0. DOI: 10.5281/zenodo.1217031. URL: https://github.com/scikit-hep/pylhe.

[84] Rene Brun and Fons Rademakers. "ROOT—An object oriented data analysis framework". In: *Nuclear instruments and methods in physics research section A: accelerators, spectrometers, detectors and associated equipment* 389.1-2 (1997), pp. 81–86.

[85] A. Pukhov. "Adaptation of Vegas for event generation". In: *Nuclear Instruments Methods in Physics Research Section A-accelerators Spectrometers Detectors and Associated Equipment - NUCL INSTRUM METH PHYS RES A* 502 (Apr. 2003), pp. 596–598. DOI: 10.1016/S0168-9002(03)00514-X.

[86] M Tanabashi et al. "Particle data group". In: *Phys. Rev. D* 98.3 (2018), p. 030001.

[87] Claudia Patrignani et al. "Review of particle physics". In: (2016).

[88] Albert M Sirunyan, CMS Collaboration, et al. "Performance of the CMS muon detector and muon reconstruction with proton-proton collisions at $\sqrt{s} = 13$ TeV". In: (2018).

Ringraziamenti

Sono stata indecisa fino all'ultimo se scrivere questa pagina o meno, ma visto che con le sole mie forze oggi non sarei alla fine di questo percorso, trovo necessario, o quanto meno doveroso, spendere qualche parola per chi mi è stato accanto e mi ha aiutato a realizzare tutto ciò.

Il primo grazie va al Professor Fanò che ha creduto in me dal primo momento e mi ha dato massima fiducia nell'affidarmi questo progetto; lo ringrazio infinitamente per l'opportunità e per i mille incoraggiamenti.

Grazie poi a Valentina che mi è stata sempre accanto: la persona di riferimento per qualsiasi problema pratico, teorico, burocratico. Grazie infinite per avermi accompagnato in questi mesi.

Grazie agli Avengers, quelli veri, quelli che quotidianamente mi hanno ascoltata, supportata e incoraggiata. Grazie per avermi aiutato a trovare la luce anche nelle giornate più buie.

Grazie Andrea per il supporto tecnico e l'infinita pazienza, sarai sempre il mio debbugger e consulente informatico di riferimento.

Grazie Cannella e Cardamomo, le amiche di sempre, per il silenzioso supporto e sostegno, siete un porto sicuro.

Grazie Elena, Camilla, Sara e Rachele per aver sopportato i miei mille sfoghi, per essermi venute prontamente in soccorso ogni qualvolta mi sentivo scoraggiata e perdevo fiducia nelle mie capacità. Grazie per aver riso e scherzato con me. Grazie per le mille mila chiacchiarate, che fossero frivole o serie non importa, le conserverò quanto più a lungo nei miei ricordi. Ringrazio il destino di avermi dato la possibilità di conoscervi.

Filippo: grazie, grazie, grazie. Anche se durante la magistrale non sei stato il mio compagno di banco, nei miei pensieri lo sarai sempre. Grazie per esserci stato dal primissimo giorno. Mi auguro che tra qualche tempo potremmo chiamarci colleghi e passare qualche pausa caffè a lamentarci del lavoro e degli studenti.

Alla mia famiglia, a chi c'è e a chi ci sarebbe tanto voluto essere, grazie per avermi supportato e amato sempre, infinitamente, incondizionamente. Spero di avervi reso fieri.

Grazie Matteo. Grazie. Sei la mia roccia. Senza il tuo continuo sostegno e appoggio questa tesi non sarebbe mai stata scritta. Questo traguardo non è solo mio, devi sentirlo anche tuo perché se non ci fossi stato te a spronarmi, ad insegnarmi a dare e richiedere sempre il meglio, accettando allo stesso tempo i miei limiti, forse mi sarei arresa cinque anni fa.

Infine grazie a chiunque in questi anni, e specialmente in questo periodo, mi ha aiutato anche solo con una parola di incoraggiamento: anche i gesti che possono sembrare piccoli e insignificanti, possono fare la differenza.

Arrivati a questo punto, non mi resta che dire...

Addio e grazie per tutto il pesce!